

Contents

The Experimental Verification of a Generalized Model of Equivalent Circuits ZOLTÁN LUKÁCS, DÁVID BACCILIERI, AND TAMÁS KRISTÓF	1–8
Photocatalytic Degradation of Rhodamine B in Heterogeneous and Homogeneous Systems ASFANDYAR KHAN, ZSOLT VALICSEK, AND OTTÓ HORVÁTH	9–16
A Framework for Demonstration Devices Used in Distance-Learning Environments PÉTER DECSI, ÁDÁM BORS, PÉTER KOCSOR, BÁLINT VÖRÖS, BARNABÁS HORVÁTH, SÁNDOR GUBA, ZOLTÁN GUGOLYA, SÁNDOR MESTER, AND ISTVÁN SZALAI	17–21
Optimisation of the Physical Properties of Rice Husk Ash in Ceramic Materials Using the Response Surface Methodology ASOTAH WISDOM, UDOCHUKWU MARK, ELAKHAME ZEBERU, AND ABRAHAM ADELEKE	23–30
Comparative Study on Anaerobic Degradation Processes of Pressed Liquid Fraction of Organic Solid Waste TAMÁS RÓZSENBERSZKI, LÁSZLÓ KOÓK, PÉTER BAKONYI, NÁNDOR NEMESTÓTHY, AND KATALIN BÉLAFI-BAKÓ	31–35
Electric Vehicle Modelling and Simulation of a Light Commercial Vehicle Using PMSM Propulsion AMINU BABANGIDA AND PÉTER TAMÁS SZEMES	37–46
Development of Compartment Models for Diagnostic Purposes BÁLINT LEVENTE TARCSAY, ÁGNES BÁRKÁNYI, TIBOR CHOVÁN, AND SÁNDOR NÉMETH	47–58
Polyvinylpyrrolidone as a Corrosion Inhibitor for Carbon Steel in a Perchloric Acid Solution: Effect of Structural Size ABBES BENCHADLI, TARIK ATTAR, BOULANOUAR MESSAOUDI, AND ESMA CHOUKCHOU-BRAHAM	59–69
Modelling of the Pyrolysis Zone of a Downdraft Gasification Reactor MÁRTA KÁKONYI, ÁGNES BÁRKÁNYI, TIBOR CHOVÁN, AND SÁNDOR NÉMETH	71–76
<i>Daphnia Magna</i> Acute Immobilization Test: an Opportunity to Test the Ecotoxicity of Alternative Fuels KATALIN ESZTER HUBAI	77–82
Influence of Mineral Composition in Natural Granite Rocks on Microhardness ESZTER KELEMEN-CSERTA AND ISTVÁN GÁBOR GYURIKA	83–88

THE EXPERIMENTAL VERIFICATION OF A GENERALIZED MODEL OF EQUIVALENT CIRCUITS

ZOLTÁN LUKÁCS*¹, DÁVID BACCILIERI¹, AND TAMÁS KRISTÓF¹

¹Center for Natural Sciences, University of Pannonia, Egyetem u. 10, 8200 Veszprém, HUNGARY

The determination of typical parameters of electrochemical systems, e.g. the polarization or charge transfer resistances, can be critical with regard to the application of Electrochemical Impedance Spectroscopy (EIS) if the lower frequency range is biased as a result of transport and/or adsorption/desorption processes. In such cases, the charge transfer resistance should be assessed from the higher frequency range which is typically inadequate in itself as an input for nonlinear parameter fitting. In earlier publications, an alternative mathematical treatment of both the Equivalent Circuit (EC) and of the parameter dispersion was provided using a generalized model of ECs and also a dispersion-invariant model of the electrochemical interface. In the present work, the previously presented experimental EIS results were crosschecked to verify the performance of the generalized model against a series of redox and corrosion systems. The results proved that the applied method is consistent and provides a fairly good correlation between the principal resistance data assessed by different methods.

Keywords: *Electrochemical Impedance Spectroscopy, parameter dispersion, linearized model, equivalent circuit, polarization resistance*

1. Introduction

Electrochemical Impedance Spectroscopy (EIS) is used to study systems in many electrochemical fields, e.g., electrode kinetics, the testing of bilayer systems, batteries, galvanic cells, corrosion, solid-state electrochemical processes, bioelectrochemistry, photovoltaic systems etc. In EIS, the studied system is perturbed from its equilibrium (or stationary) state by a small-amplitude sinusoidal potential signal. For this AC potential signal, it is assumed that the transfer function of the electrochemical kinetic system can be represented by a so-called equivalent circuit (EC). The simplest circuit of this kind is the Voigt circuit, a parallel RC circuit, complete with a resistor representing the pure ohmic[†] solution resistance, which approximates the transfer function of the electrochemical system well in many cases[‡] (see Fig. 1A).

The transfer function of Model A in Figure 1 is given by

$$Z(\omega) = R_S + \frac{R_{CT}}{1 + i\omega\tau}, \quad (1)$$

where i denotes the imaginary unit, ω stands for the angular frequency and $\tau = R_{CT}C_{DL}$ represents the time constant of the RC circuit. Eq. 1 describes an ideal theoretical

model and the EIS curves plotted from it yield a perfect semicircle on the so-called Nyquist diagram. The value of the ohmic solution resistance (R_S) is determined from the high-frequency data (~ 10 kHz – 1 kHz). If diffusion, adsorption or other processes do not influence the curve, then the sum of the solution and charge transfer resistances can be determined from the low-frequency data. In contrast with the theoretical expectations, in practice, the impedance spectroscopy diagrams measured have always been slightly flattened (‘depressed semicircles’). This depression can be modelled phenomenologically by using a power of less than 1 in the frequency-dependent term of Eq. 1:

$$Z(\omega) = R_S + \frac{R_{CT}}{1 + (i\omega\tau)^{1-\beta}}, \quad (2)$$

where $0 < \beta \ll 1$ denotes the constant phase coefficient and the resulting element with the fractional power in Eq. 2 is referred to in the literature as a constant phase element. As the fractional power expression results in a constant phase impedance at high frequencies, this phenomenon is commonly referred to as the Constant Phase Element (CPE).

Research into the CPE and related phenomena dates back many decades. Cole and Cole [1, 2] investigated the capacitance of solid and liquid dielectrics as well as interpreted the appearance of the CPE as dependent on the frequency of the dielectric constant. The application of AC methods and EIS in particular to a wide range of electro-

*Correspondence: lukacs.zoltan@mk.uni-pannon.hu

[†]Pure ohmic in the electrochemically relevant frequency range.

[‡]In this section, the effects of the transport and adsorption/desorption steps are not considered. They are mentioned in sufficient detail in the section where the experimental results are discussed.

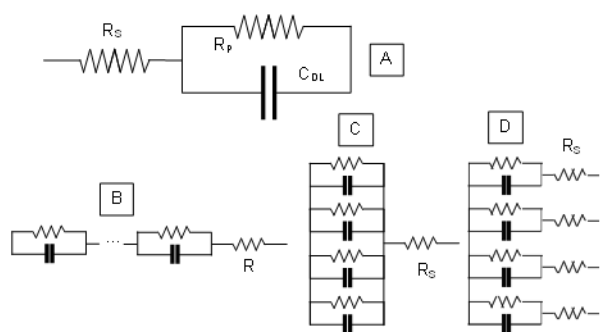


Figure 1: Equivalent circuits corresponding to Models A–D and frequently applied in the relevant literature (see further comments in the text).

chemical systems has become quite common in electrochemical kinetics [3–8], electrode surface structure investigations [9–14], corrosion studies [15–21], battery and fuel cell development [22–26], membrane studies [27,28] and many other fields in electrochemistry.

The CPE appears in all the cited works and can be regarded with a high degree of certainty as an inherent characteristic of electrochemical systems. However, the origin and evaluation of the CPE has remained a controversial issue. Most works on the topics agree that the CPE can be interpreted as a consequence of the distribution of the time constant of RC circuits representing the characteristics with regard to the capacitance and conductivity of the electrochemical interface. Cole [1] assumes a lognormal distribution of the relaxation time constants. A similar distribution function is proposed by Brug [3]. In subsequent works, the appearance of the CPE is frequently interpreted by means of equivalent circuits that include many RC elements in parallel or series. (Implicitly, the distribution functions can also be recurred to such equivalent circuits.)

The applicable equivalent circuits can be roughly divided into two categories. Some fall into the category of the so-called ‘3D’ (three-dimensional) dispersion models which correspond to the structures perpendicular to the surface, contributing to the conventional equivalent circuit with a series of additional parallel RC circuits [14, 15], as shown in Model B in Fig. 1. The 3D model (or its derivatives, see below) has been successfully applied in the description of passive films and coatings [29–31]. The so-called 2D dispersion models [3, 14] are intended to describe the distribution of the EIS parameters in two dimensions on the electrode surface. This dispersion can be attributed to the heterogeneity of the surface and the resulting deviations of the (intensive) kinetic parameters, i.e., the time constants.

Discussions concerning the 2D dispersion can lead, however, to an unexpected conclusion if this is consequently carried out. The 2D dispersion model, i.e., the dispersion of the time constants of the RC circuits, representing the kinetic parameters of the individual active re-

action sites connected in parallel to each other, as shown in Model C in Fig. 1, will degenerate to Model A. In order to avoid this, the effect of the solution resistance is taken into account to re-establish the ability of conventional EC patterns to interpret CPE behaviour (‘While an Ohmic resistance in physical systems cannot be avoided, the example illustrated in Fig. 1B illustrates the crucial role played by the Ohmic resistance in CPE behavior associated with surface distributions.’ [14]). However, there are at least three very important reasons to have serious reservations with regard to this concept. Firstly, Pajkossy has shown [10] that ‘capacitance dispersion due to irregular geometry appears at much higher frequencies than is usual in electrochemical methodologies’ which means that the irregular geometry, which acts on the EIS impedance function through the variation in the (local) solution resistance, cannot be the reason for the dispersion in the generally applied and electrochemically relevant frequency range. Secondly, in highly conductive solutions and/or with high-resistance (i.e., slow) electrochemical reactions, the contribution of the solution resistance to the overall impedance can be negligible compared to that of the charge transfer resistance, especially at lower frequencies. Thirdly, strictly speaking, the solution resistance is not an inherent part of the impedance of the electrochemical impedance system. By moving the tip of the Luggin capillary closer or farther away, the value of the measured solution resistance can be varied significantly, therefore, any calculations using it in the modelling or evaluation of the kinetic process are debatable.

In conclusion, Models C and D in Fig. 1 are not applicable in the interpretation of the CPE phenomenon. Consequently, by proceeding forwards on this path, it follows that Model A in Fig. 1 is not and cannot be the ultimate model (transfer function) of the electrochemical interface. The ultimate model is something more complex, which can, in certain cases, be simplified to Model A as far as the accuracy of measured data is concerned. In an earlier paper [32], this issue was already discussed in brief (see Fig. 3 and the relevant text in the cited paper).

This contradiction was realized in the relevant literature decades ago. In a noteworthy work, Agarwal et al. [33] approximated a number of ECs to Model B which obviously does not match the physical content of the approximated ECs, however, the fitted curves match the experimental ones very well. These results are also confirmed from another point of view. It has been proven [34, 35] that some ECs, exhibiting quite different elements and connection patterns, have the same transfer function. These findings also show that the concept of the ‘equivalent circuit’ is by no means as solid nor unambiguous as it would seem to be at first sight. After all, the question what is the minimum statement that can be both relevant and unambiguous concerning the EIS equivalent circuit and parameter determination in general is raised.

A possible answer to this question was presented in two recent publications [36, 37]. It was assumed that Model A in Fig. 1 is approximately correct and devia-

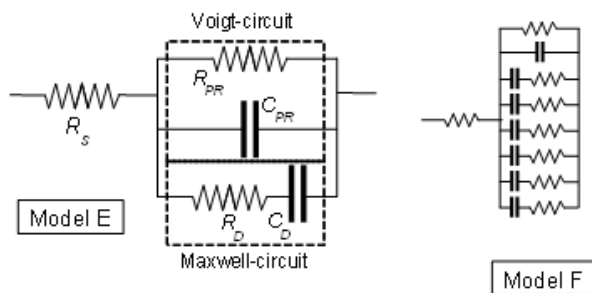


Figure 2: Model E by applying the general scheme and Model F with the series of Maxwell circuits connected in parallel.

tions from it are due to the parameter dispersions and/or mechanistic effects, moreover, all these effects can be fitted using a properly chosen series of EC elements. After due consideration, the model of a Voigt circuit (equivalent to Model A) and a series of Maxwell circuits connected in parallel was chosen (see Fig. 2, Model F). Model F has some important features which have practical advantages; the part of the EC corresponding to Model A, representing the ‘ideal’ behaviour of the interface, is separated parallel from the rest of the EC. This arrangement results in a linear separation in the compensated admittance:

$$Y_C = Y_{PR} + i\omega C_{PR} + \sum_{k=1}^K \frac{i\omega C_{D,k}}{1 + i\omega\tau_{D,k}} \quad (3)$$

where $Y_{PR} = 1/R_{PR}$ and C_{PR} denote the principal admittance and capacitance, respectively, $C_{D,k}$ represents the capacitance and $\tau_{D,k}$ stands for the time constant of the k th Maxwell circuit connected in parallel. The physical interpretation, performance and limitations of the principal parameters as well as the linearization in general are discussed in detail in previous papers [36, 37]. In Ref. [36], an equation to determine the principal admittance was published by our group ($x = \omega^2$):

$$\frac{\partial \ln x}{\partial \ln Y'_C} = Y_{PR} \frac{\partial \ln x}{\partial Y'_C} + 1 \quad (4)$$

The principal admittance which is, under certain conditions, equivalent to the reciprocal of the charge transfer or polarisation resistance, can be determined from a relatively narrow frequency range approximate to or higher than the critical frequency[§]. This is a serious advantage to any nonlinear model fitting which requires impedance data from a wider and, in particular, a lower frequency range (i.e., lower than the critical frequency) where the adsorption/desorption or transport (diffusion) processes may have a stronger impact on the measured impedance data. In a previous paper [36], Eq. 4 was tested in an

[§]Critical frequency is understood as the frequency value where the imaginary part of the impedance has a (local) extremum at the ‘top’ of the ‘depressed semicircle.’ The accurate value of the critical frequency can be calculated via a quadratic fitting of the nearest points. In some EIS spectra, such an extremum cannot be established.

experimental system (quinhydrone redox system in 10% HCl) and, in a more recent paper [37], other methods developed to determine the principal admittance were tested in the quinhydrone as well as three other systems, namely Fe, Cu and COR (see their descriptions in the Experimental section below). In this paper, the testing of Eq. 4 against the latter three systems is presented and discussed.

2. Experimental

In order to gain a comprehensive overview concerning the performance of the proposed new parameter evaluation method based on Eq. 4, three test systems were created (the short names, used for identification in the paper, are in brackets):

$\text{Fe}^{3+}/\text{Fe}^{2+}$ redox system (Fe): metallic iron was dissolved in 10% m/v HCl at a concentration of $8 \cdot 10^{-4}$ mol/dm³ and $\text{FeCl}_3 \cdot 6\text{H}_2\text{O}$ was added to set the same concentration of 8×10^{-4} mol/dm³ for FeCl_3 . Solutions were diluted using 10% HCl to the concentrations indicated in Table 1.

The working, reference and counter electrodes were all composed of platinum for this system. The working electrode was a platinum plate with a surface area of 2 cm², the reference electrode was a larger platinum sheet with a surface area of 5 cm² and the counter electrode was a platinum net with an approximate surface area of 20 cm². The potential of the platinum reference electrode was measured before and after the EIS measurements against a saturated Ag/AgCl electrode to check if the redox potential of the system was reasonably close to the expected, calculated values.

Cu^{2+}/Cu non-corrosive copper/copper ion system (Cu): the CuSO_4 concentrations and the supporting electrolyte are included in Table 1. The working electrode was a cylindrical copper electrode 30 mm in length and with a diameter of 6 mm in a teflon holder, while the geometric surface area of the electrode was 5.94 cm². The reference electrode was composed of copper with the same dimensions and the counter electrode was a copper sheet with a surface area of approximately 20 cm².

In the corrosive systems (COR), the working electrode was a DIN St 52-type cylindrical steel electrode 30 mm in length and with a diameter of 6 mm in a teflon holder, while the geometric surface area of the electrode was 5.94 cm². The saturated Ag/AgCl electrode was used as the reference electrode and a platinum net with an approximate surface area of 20 cm² as a counter electrode. The electrolyte compositions are shown in Table 1.

All the working electrodes were degreased in acetone. The platinum electrodes were kept in a 10% HCl solution for at least 3 hours before the experiment. The copper and steel electrodes were polished with #400, #600 and finally #1000 emery paper, while the copper electrodes were etched in a solution of 20% HNO_3 for 5 minutes. The steel electrodes used for the corrosion experiments

Table 1: Summary of the parameters and identifiers of the systems and series.

System		Series		Electrode	Electrolyte
Abbreviation	Short description	ID	Definition		
Fe	Fe(II)/Fe(III) redox	1E-4	Fe(II), Fe(III) concentration, M	Platinum	10% HCl
		2E-4			
		4E-4			
		8E-4			
Cu	Cu/Cu(II) reversible metal	1E-4	Cu(II) concentration, M	Cu	1M H ₂ SO ₄
		2E-4			
		4E-4			
		8E-4			
COR	Corrosion system	COR1	N/A	St-52 steel	5% NaCl + 0.5% HAc*
		COR2			5% NaCl + 0.1% HCl
		COR3			1% HCl
		COR4			10% HCl

*Acetic acid

(system COR) were pre-treated in a 10% HCl solution for 5 minutes before being placed in the cell.

All the experiments were carried out in a conventional three-electrode electrochemical cell with a volume of approximately 700 cm³. The experiments were conducted at room temperature and the solutions were not deaerated. All EIS spectra were measured twice and both runs were evaluated. In all three systems (Fe, Cu and COR), the electrodes were prepared before the first run and only the electrolytes were replaced for the purpose of measuring the subsequent runs. The parameters and identifiers (used to denote the measurement systems and runs in the discussion of the results) are shown in Table 1. Consecutive runs using the same solution composition are denoted with a -1 or -2 suffix at the end of the IDs, e.g., 1E-4-1 and 1E-4-2 for the Fe³⁺ and Fe²⁺ concentrations in the Fe system, respectively, namely 10⁻⁴ mol/dm³ (M).

The EIS spectra were measured with a Metrohm Autolab PGSTAT 302N-type potentiostat using NOVA 1.11 software. The amplitude of the applied potential signal was 10 mV (i.e., 20 mV p-p). All spectra were taken within the 10 kHz – 100 mHz range and 20 frequency points were measured per decade over a logarithmically equidistant distribution. In all the experiments, two spectra were measured in order to assess the rate of impedance drifts over time.

The linear fittings were generally very good which involved a high count of 9s in the correlation coefficient. In order to avoid the cumbersome counting of the digits, the Precision Factor P_R was introduced according to

$$P_R = -\lg(1 - R^2), \quad (5)$$

where R^2 denotes the square of the correlation coefficient (e.g., if $R^2 = 0.999$, then $P_R = 3$).

3. Results and Discussion

The Nyquist diagrams of the Fe, Cu and COR systems are shown in Figs. 3-5, respectively. The corresponding Bode plots are available in Ref. [37]. The three systems exhibit quite different characteristics with regard to how well they fit to the conventional EC parameters and non-linear least squares methods. The Fe system could be fitted with a Randles circuit including a CPE instead of a double layer capacitance if the diffusion-controlled low-frequency range was longer and consequently better separated.

This fitting procedure was tried but yielded uncertain results with high parameter errors and strong correlations in the Hessian matrix. In general, the analytic methods do not yield good results if the measurement data do not have ranges where they are mainly sensitive to one parameter only. The measurements below 100 mHz last for quite a lengthy period of time and during this time range, the nonstationarity ('time drift') can produce a significant degree of bias with regard to the measurement data which should be avoided. The Cu system is a bit worse because the low-frequency range data cannot be interpreted in terms of the conventional EC parameters at all.

The COR system is, however, quite different since it can be fitted with a conventional CPE and charge transfer resistance. The common feature in all three systems is a relatively regular and similar arc in the frequency range higher than the critical frequency (i.e., the frequency where the imaginary part of the impedance has a maximum – this is somewhat unclear in the case of the Cu system but the regular behaviour exhibited in the high-frequency range is clearly visible). The similarities in and regularities of the higher-frequency range impedance data would suggest that only this range should be used to determine both the double layer capacitance, which is inher-

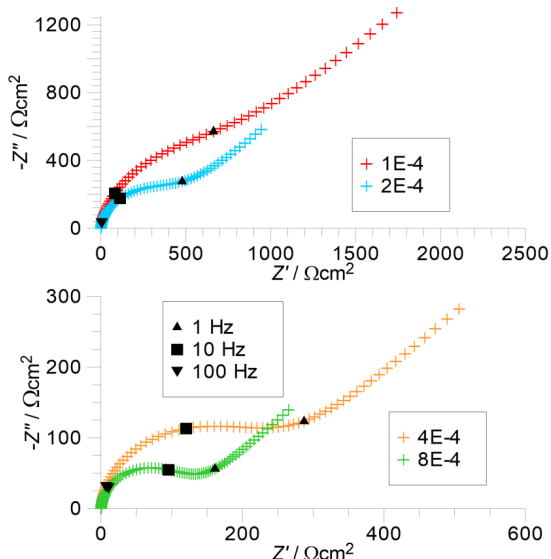


Figure 3: Nyquist plots of the Fe system.

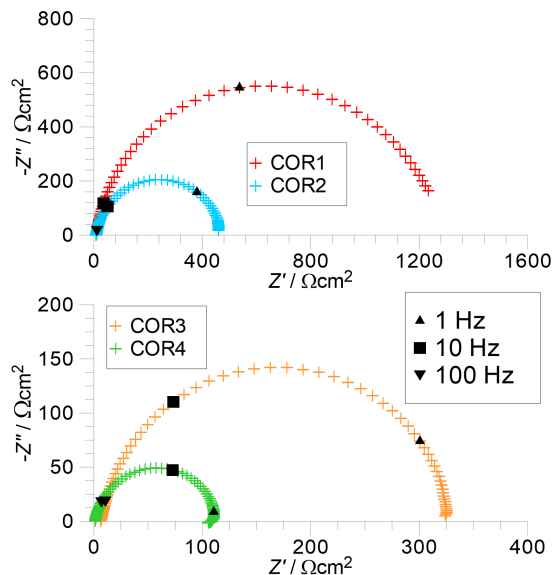


Figure 5: Nyquist plots of the COR system.

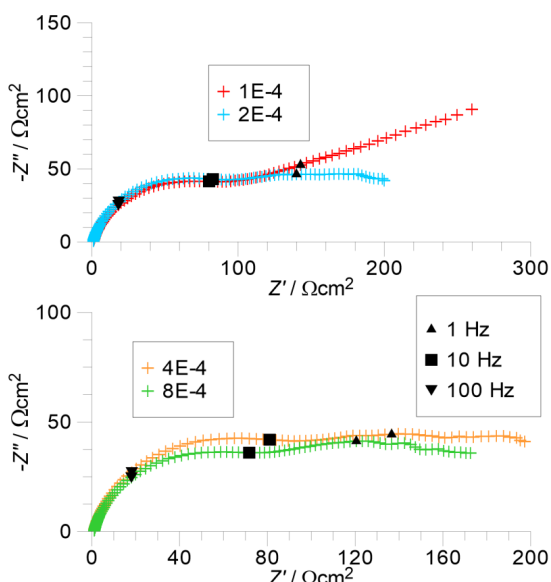


Figure 4: Nyquist plots of the Cu system.

ently related to the high frequency range, and the charge transfer resistance, which is, in contrast, related to the lower frequency data range. This circumstance requires a more sophisticated approach, which has been outlined in Ref. [36] and is applied in this paper, for the three systems discussed.

Based upon the aforementioned considerations, the importance of developing methods that can determine the charge transfer resistance from the higher frequency data alone is indisputable. The testing of Eq. 4 with the discussed experimental systems is shown in Figs. 6 to 8. The data points are obtained by calculating the gradient Y_{PR} according to Eq. 4 using the two adjacent points (Method (i)) and by fitting the gradients of the lines to 5 points of both greater and smaller frequencies at each frequency (Method (ii) in Ref. [36]). Therefore, the lines are formed

by effectively averaging out the points. The curves are strongly dependent on the frequency and, in this case, selecting the most appropriate value to characterize the charge transfer resistance of the system is always an issue. The optimal value of the principal admittance was selected on the basis of the linear-fitting correlation data, moreover, the data set providing the highest correlation coefficient was accepted as the ‘real’ value. The P_R maxima at very high frequencies were not taken into account (see Fig. 6).

By comparing Figs. 3-5 with Figs. 6-8, it can be concluded that the more regular (depressed) semicircles are formed in the Nyquist diagram, the more established principal admittance data can be obtained from Eq. 4. However, if regular semicircles are formed by a system, then the practical usefulness of the proposed evaluation is strongly limited because in such cases, conventional evaluation methods can generally be applied. This is the case with the COR system. The application of the method is necessitated in systems like that of Fe and Cu where conventional nonlinear fitting methods or any other simple methods (e.g. the graphical determination of R_{CT} [36,37]) cannot be used at all or with only a very limited degree of precision. In order to also test the versatility of the method in such systems, the principal admittance values determined via Method (ii) were compared to those calculated by Eq. 13 in Ref. [37][¶] for the three systems investigated in this paper and also for the quinhydrone (QH) system published in the previous paper [36] on the subject, the results of which are presented in Fig. 9. According to the results, a fairly good correlation coefficient is obtained which indicates that both methods, namely Method (ii) and Eq. 13, calculate the same phys-

[¶]The derivation leading to Eq. 13 (in Ref. [37]) is also based on Eq. 3 (in this paper) but includes specific mathematical transformations based on the elimination of the dispersion parameters from the respective equations.

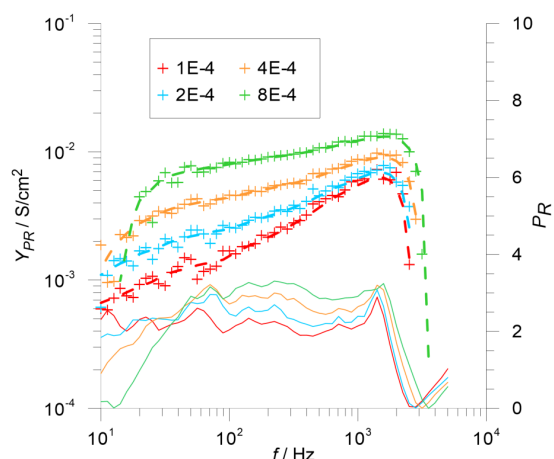


Figure 6: Principal admittance of the Fe system calculated by Eq. 4 using Method (i) (points) and Method (ii) (dotted lines). Solid lines indicate the P_R values obtained using Method (ii).

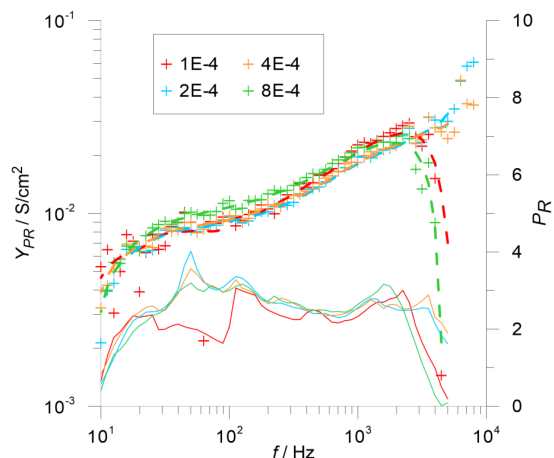


Figure 7: Principal admittance of the Cu system calculated by Eq. 4 using Method (i) (points) and Method (ii) (dotted lines). Solid lines indicate the P_R values obtained using Method(ii).

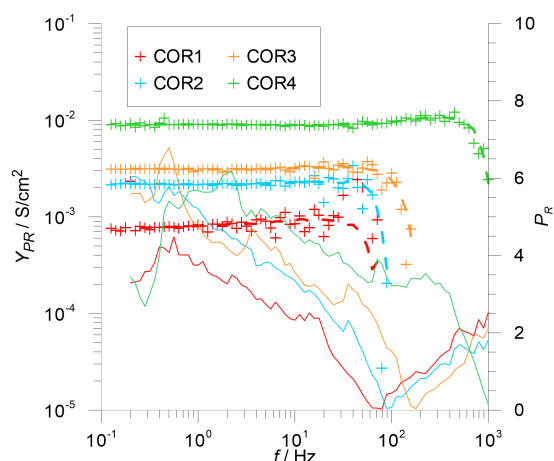


Figure 8: Principal admittance of the COR system calculated by Eq. 4 using Method (i) (points) and Method (ii) (dotted lines). Solid lines indicate the P_R values obtained using Method(ii).

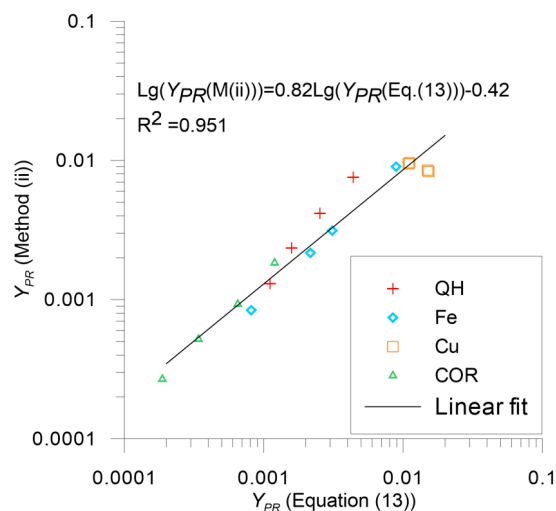


Figure 9: Correlation between the logarithms of the principal admittance obtained by Method(ii) using Eqs. 4 and 13 in Ref. [37]. The linear fit was calculated from the logarithms of the principal admittance data. The QH (quinhydrone) data were taken from Ref. [36].

ical quantity.

The data in Fig. 9 prove that both methods are applicable for the determination of the principal admittance. The question that is typically raised in similar situations is which method is better. In our opinion, it is still too early to make such a judgement given that in Ref. [37] several additional equations were also published to calculate the principal admittance. Some of these equations differ in terms of their initial physical considerations (compare Eq. 4 in this paper and Eq. 13 in Ref. [37]), while others differ only as far as the weighting of data points is concerned (compare Eq. 8 with 8a or Eq. 13 with Eq. 14 in Ref. [37]).

It is recommended that these methods should be applied especially in those cases when the impedance data in the low-frequency range (typically below the critical frequency) are not interpretable or cannot be fitted for some reason (e.g., the applicable EC cannot be assessed unambiguously). In such cases, by applying two or more of the proposed equations, the uncertainty in this determination can be decreased by only utilizing parameters, which are sufficiently close to one another.

4. Conclusions

A recent method developed to determine the principal admittance was tested on electrochemical redox and corrosion systems in order to check and compare the performances of the methods. The characteristics of the impedance with regard to such electrochemical systems exhibited features which often make conventional non-linear fitting methods unusable or at least inaccurate. The new method was applied to determine the principal admittance from the impedance data obtained in the higher frequency range which exhibit a more regular shape but

are not applicable to conventional fitting methods alone. By comparing this new method with another also newly developed method (Eq. 13 in Ref. [37]), a strong correlation between the parameters measured using the two methods was observed, which proves that both of them are suitable for determining the principal admittance of systems which exhibit similarly regular behaviour within the higher frequency range.

Acknowledgement

Present article was published in the frame of the project GINOP-2.3.2-15-2016-0053 ('Development of engine fuels with high hydrogen content in their molecular structures (contribution to sustainable mobility)').

REFERENCES

- [1] Cole K.S.; Cole, R.H.: Dispersion and absorption in dielectrics 1. Alternating current characteristics, *J. Chem. Phys.*, 1941, **9**(4), 341–351 DOI: [10.1063/1.1750906](https://doi.org/10.1063/1.1750906)
- [2] Cole K.S.; Cole, R.H.: Dispersion and absorption in dielectrics 2. Direct current characteristics, *J. Chem. Phys.*, 1942, **10**(2), 98–105 DOI: [10.1063/1.1723677](https://doi.org/10.1063/1.1723677)
- [3] Brug, G.J.; van den Eeden, A.L.G.; Sluyters-Rehbach, M.; Sluyters, J.H.: The analysis of electrode impedances complicated by the presence of a constant phase element, *J. Electroanal. Chem.*, 1984, **176**(1–2), 275–295 DOI: [10.1016/S0022-0728\(84\)80324-1](https://doi.org/10.1016/S0022-0728(84)80324-1)
- [4] Macdonald, D.D.: Review of mechanistic analysis by electrochemical impedance spectroscopy, *Electrochim. Acta*, 1990, **35**(10), 1509–1525 DOI: [10.1016/0013-4686\(90\)80005-9](https://doi.org/10.1016/0013-4686(90)80005-9)
- [5] Lasia, A.; Rami, A.: Kinetics of hydrogen evolution on nickel electrodes, *J. Electroanal. Chem. Interfacial Electrochem.*, 1990, **294**(1–2), 123–141 DOI: [10.1016/0022-0728\(90\)87140-F](https://doi.org/10.1016/0022-0728(90)87140-F)
- [6] Antaño-Lopez, R.; Keddami, M.; Takenouti, H.: A new experimental approach to the time-constants of electrochemical impedance: frequency response of the double layer capacitance, *Electrochim. Acta*, 2001, **46**(24–25), 3611–3617 DOI: [10.1016/S0013-4686\(01\)00640-5](https://doi.org/10.1016/S0013-4686(01)00640-5)
- [7] Hu, J.-M.; Zhang, J.-Q.; Cao, Ch.-N.: Oxygen evolution reaction on IrO₂-based DSA[®] type electrodes: kinetics analysis of Tafel lines and EIS, *Int. J. Hydrog. Energy*, 2004, **29**, 791–797 DOI: [10.1016/j.ijhydene.2003.09.007](https://doi.org/10.1016/j.ijhydene.2003.09.007)
- [8] Lockett, V.; Sedev, R.; Ralston, J.; Horne, M.; Rodopoulos, T.: Differential capacitance of the electrical double layer in imidazolium-based ionic liquids: influence of potential, cation size, and temperature, *J. Phys. Chem. C*, 2008, **112**, 7486–7495 DOI: [10.1021/jp7100732](https://doi.org/10.1021/jp7100732)
- [9] Nyikos, L.; Pajkossy, T.: Electrochemistry at fractal interfaces: the coupling of *ac* and *dc* behavior at irregular electrodes, *Electrochim. Acta*, 1990, **35**(10), 1567–1572 DOI: [10.1016/0013-4686\(90\)80011-C](https://doi.org/10.1016/0013-4686(90)80011-C)
- [10] Pajkossy, T.: Impedance of rough capacitive electrodes, *J. Electroanal. Chem.*, 1994, **364**(1–2), 111–125 DOI: [10.1016/0022-0728\(93\)02949-1](https://doi.org/10.1016/0022-0728(93)02949-1)
- [11] Lasia, A.: Impedance of porous electrodes, *J. Electroanal. Chem.*, 1995, **397**(1–2), 27–33 DOI: [10.1016/0022-0728\(95\)04177-5](https://doi.org/10.1016/0022-0728(95)04177-5)
- [12] Kerner, Zs.; Pajkossy, T.: On the origin of capacitance dispersion of rough electrodes, *Electrochim. Acta*, 2000, **46**(2–3), 207–211 DOI: [10.1016/S0013-4686\(00\)00574-0](https://doi.org/10.1016/S0013-4686(00)00574-0)
- [13] Jović, V.D.; Jović, B.M.: EIS and differential capacitance measurements onto single crystal faces in different solutions Part I: Ag(111) in 0.01 M NaCl, *J. Electroanal. Chem.*, 2003, **541**, 1–11 DOI: [10.1016/S0022-0728\(02\)01309-8](https://doi.org/10.1016/S0022-0728(02)01309-8)
- [14] Hirschorn, B.; Orazem, M.E.; Tribollet, B.; Vivier, V.; Frateur, I.; Musiani, M.: Determination of effective capacitance and film thickness from constant-phase-element parameters, *Electrochim. Acta*, 2010, **55**(21), 6218–6227 DOI: [10.1016/j.electacta.2009.10.065](https://doi.org/10.1016/j.electacta.2009.10.065)
- [15] Jüttner, K.; Lorenz, W.J.; Kendig, M.W.; Mansfeld, F.: Electrochemical impedance spectroscopy on 3-D inhomogeneous surfaces, *J. Electrochem. Soc.*, 1988, **135**, 332–339 DOI: [10.1149/1.2095610](https://doi.org/10.1149/1.2095610)
- [16] Hack, H.P.; Scully, J.R.: Defect area determination of organic coated steels in seawater using the breakpoint frequency method, *J. Electrochem. Soc.*, 1991, **138**(1), 33–40 DOI: [10.1149/1.2085574](https://doi.org/10.1149/1.2085574)
- [17] Rammelt, U.; Reinhard, G.: Application of electrochemical impedance spectroscopy (EIS) for characterizing the corrosion-protective performance of organic coatings on metals, *Prog. Org. Coat.*, 1992, **21**(2–3), 205–226 DOI: [10.1016/0033-0655\(92\)87005-U](https://doi.org/10.1016/0033-0655(92)87005-U)
- [18] Tan, Y.J.; Bailey, S.; Kinsella, B.: An investigation of the formation and destruction of corrosion inhibitor films using electrochemical impedance spectroscopy (EIS), *Corros. Sci.*, 1996, **38**(9), 1545–1561 DOI: [10.1016/0010-938X\(96\)00047-9](https://doi.org/10.1016/0010-938X(96)00047-9)
- [19] Macdonald, D.D.; Sikora, E.; Engelhardt, G.: Characterizing electrochemical systems in the frequency domain, *Electrochim. Acta*, 1998, **43**(1–2), 87–107 DOI: [10.1016/S0013-4686\(97\)00238-7](https://doi.org/10.1016/S0013-4686(97)00238-7)
- [20] Bommersbach, P.; Alemany-Dumont, C.; Millet, J.P.; Normand, B.: Formation and behaviour study of an environment-friendly corrosion inhibitor by electrochemical methods, *Electrochim. Acta*, 2005, **51**(6), 1076–1084 DOI: [10.1016/j.electacta.2005.06.001](https://doi.org/10.1016/j.electacta.2005.06.001)
- [21] Baril, G.; Galicia, G.; Deslouis, C.; Pébère, N.; Tribollet, B.; Vivier, V.: An impedance investigation of the mechanism of pure magnesium corrosion in sodium sulfate solutions, *J. Electrochem. Soc.*, 2007, **154**(2), C108 DOI: [10.1149/1.2401056](https://doi.org/10.1149/1.2401056)
- [22] Levi, M.D.; Salitra, G.; Markovsky, B.; Teller, H.; Aurbach, D.; Heider, U.; Heider, L.: Solid-

- state electrochemical kinetics of Li-ion intercalation into $\text{Li}_{1-x}\text{CoO}_2$: Simultaneous application of electroanalytical techniques SSCV, PITT, and EIS, *J. Electrochem. Soc.*, 1999, **146**(4), 1279–1289 DOI: [10.1149/1.1391759](https://doi.org/10.1149/1.1391759)
- [23] Wang, C.; Appleby, A.J.; Little, F.E.: Electrochemical study on nano-Sn, $\text{Li}_4.4\text{Sn}$ and $\text{AlSi}_{0.1}$ powders used as secondary lithium battery anodes, *J. Power Sources*, 2001, **93**(1–2), 174–185 DOI: [10.1016/S0378-7753\(00\)00576-0](https://doi.org/10.1016/S0378-7753(00)00576-0)
- [24] Li, Z.E.; Du, F.; Bie, X.; Zhang, D.; Cai, Y.; Cui, X.; Wang, C.; Chen, G.; Wei, Y.: Electrochemical kinetics of the $\text{Li}[\text{Li}_{0.23}\text{Co}_{0.3}\text{Mn}_{0.47}]\text{O}_2$ cathode material studied by GITT and EIS, *J. Phys. Chem. C*, 2010, **114**, 22751–22757 DOI: [10.1021/jp1088788](https://doi.org/10.1021/jp1088788)
- [25] Tang, K.; Yu, X.; Sun, J.; Li, H.; Huang, X.: Kinetic analysis on LiFePO_4 thin films by CV, GITT, and EIS, *Electrochim. Acta*, 2011, **56**(13), 4869–4875 DOI: [10.1016/j.electacta.2011.02.119](https://doi.org/10.1016/j.electacta.2011.02.119)
- [26] Niya, S.M.R.; Hoorfar, M.: Study of proton exchange membrane fuel cells using electrochemical impedance spectroscopy technique – A review, *J. Power Sources*, 2013, **240**, 281–293 DOI: [10.1016/j.jpowsour.2013.04.011](https://doi.org/10.1016/j.jpowsour.2013.04.011)
- [27] Morin, A.; Peng, Z.; Jestin, J.; Detrez, M.; Gebel, G.: Water management in proton exchange membrane fuel cell at sub-zero temperatures: An in operando SANS-EIS coupled study, *Solid State Ion.*, 2013, **252**, 56–61 DOI: [10.1016/j.ssi.2013.07.010](https://doi.org/10.1016/j.ssi.2013.07.010)
- [28] Zhiani, M.; Majidia, S.; Silva, W.B.; Gharibi, H.: Comparison of the performance and EIS (electrochemical impedance spectroscopy) response of an activated PEMFC (proton exchange membrane fuel cell) under low and high thermal and pressure stresses, *Energy*, 2016, **97**, 560–567 DOI: [10.1016/j.energy.2015.12.058](https://doi.org/10.1016/j.energy.2015.12.058)
- [29] Oliveira, J.L.; Skilbred, A.W.B.; Loken, A.; Henriques, R.R.; Soares, B.G.: Effect of accelerated ageing procedures and flash rust inhibitors on the anti-corrosive performance of epoxy coatings: EIS and dynamic-mechanical analysis, *Prog. Org. Coat.*, 2021, **159**, 106387 DOI: [10.1016/j.porgcoat.2021.106387](https://doi.org/10.1016/j.porgcoat.2021.106387)
- [30] Martinez, S.; Šoić, I.; Špada, V.: Unified equivalent circuit of dielectric permittivity and porous coating formalisms for EIS probing of thick industrial grade coatings, *Prog. Org. Coat.*, 2021, **153**, 106155 DOI: [10.1016/j.porgcoat.2021.106155](https://doi.org/10.1016/j.porgcoat.2021.106155)
- [31] Hinderliter, B.R.; Croll, S.G.; Tallman, D.E.; Su, Q.; Bierwagen, G.P.: Interpretation of EIS data from accelerated exposure of coated metals based on modeling of coating physical properties, *Electrochim. Acta*, 2006, **51**(21), 4505–4515 DOI: [10.1016/j.electacta.2005.12.047](https://doi.org/10.1016/j.electacta.2005.12.047)
- [32] Lukács, Z.: Evaluation of model and dispersion parameters and their effects on the formation of constant-phase elements in equivalent circuits, *J. Electroanal. Chem.*, 1999, **464**(1), 68–75 DOI: [10.1016/S0022-0728\(98\)00471-9](https://doi.org/10.1016/S0022-0728(98)00471-9)
- [33] Agarwal, P.; Orazem, M.E.; Garcia-Rubio, L.H.: Measurement models for electrochemical impedance spectroscopy: I . Demonstration of applicability, *J. Electrochem. Soc.*, 1992, **139**(7), 1917–1927 DOI: [10.1149/1.2069522](https://doi.org/10.1149/1.2069522)
- [34] Fletcher, S.: Tables of degenerate electrical networks for use in the equivalent-circuit analysis of electrochemical systems, *J. Electrochem. Soc.*, 1994, **141**(7), 1823–1826 DOI: [10.1149/1.2055011](https://doi.org/10.1149/1.2055011)
- [35] Harrington, D.A.; van den Driessche, P.: Mechanism and equivalent circuits in electrochemical impedance spectroscopy, *Electrochim. Acta*, 2011, **56**(23), 8005–8013 DOI: [10.1016/j.electacta.2011.01.067](https://doi.org/10.1016/j.electacta.2011.01.067)
- [36] Lukács, Z.; Kristóf, T.: A generalized model of the equivalent circuits in the electrochemical impedance spectroscopy, *Electrochim. Acta*, 2020, **363**, 137199 DOI: [10.1016/j.electacta.2020.137199](https://doi.org/10.1016/j.electacta.2020.137199)
- [37] Lukács, Z.; Baccilieri, D.; Hancsók, J.; Kristóf, T.: A dispersion-invariant model of the electrochemical impedance, *Electrochim. Acta*, 2021, **390**, 138828 DOI: [10.1016/j.electacta.2021.138828](https://doi.org/10.1016/j.electacta.2021.138828)

PHOTOCATALYTIC DEGRADATION OF RHODAMINE B IN HETEROGENEOUS AND HOMOGENEOUS SYSTEMS

ASFANDYAR KHAN^{1,2}, ZSOLT VALICSEK¹, AND OTTÓ HORVÁTH*¹

¹Department of General and Inorganic Chemistry, Center for Natural Sciences, Faculty of Engineering, University of Pannonia, Veszprém, HUNGARY

²Department of Textile Engineering, National Textile University Faisalabad, PAKISTAN

This study focuses on the photocatalytic degradation of Rhodamine B (RhB) in heterogeneous and homogeneous photo-Fenton reactions. In the heterogeneous system, iron(II) doped copper ferrite $\text{Cu}_{(x)}^{\text{II}}\text{Fe}_{(1-x)}^{\text{II}}\text{Fe}_2^{\text{III}}\text{O}_4$ nanoparticles (NPs) prepared in our previous work were employed as potential catalysts. The photodegradation of RhB was carried out in a quartz cuvette located in a diode array spectrometer. The experimental conditions such as pH, NPs dosage and H_2O_2 dosage with regard to the photocatalytic degradation of RhB were optimized to be 7.5, 500 mg/L and 8.9×10^{-2} mol/L, respectively. In addition, visible light-induced photodegradation of RhB was also carried out by using H_2O_2 over a wide pH range in the absence of heterogeneous photocatalysts. It was observed that the reaction rate significantly increased above pH 10, resulting in a faster rate of degradation of RhB, which may be attributed to the deprotonation of hydrogen peroxide. Furthermore, the potential antibacterial property of such catalysts against the Gram-negative bacterium *Vibrio fischeri* in a bioluminescence assay yielded inhibition activities of more than 60% in all cases.

Keywords: heterogeneous photo-Fenton system, iron(II) doped copper ferrites, deprotonation effect, photodegradation

1. Introduction

Synthetic dyes have numerous applications in several industries, e.g., paper, textile, leather and paint. Besides these applications, some dyes are toxic organic compounds and their discharge into the environment causes eutrophication, aesthetic pollution and distress for marine organisms [1, 2]. Some synthetic dyes are recalcitrant, that is, resistant to biological degradation and direct photolysis. In addition, many dyes contain nitrogen which produces carcinogenic as well as mutagenic aromatic amines as a result of natural anaerobic reductive degradation [3, 4].

These toxic organic dyes can be mineralized into water and carbon dioxide via photocatalytic reactions using catalysts under ultraviolet or visible light irradiation [5, 6]. Only a handful of research groups have developed and applied ferrite nanoparticles (NPs) as catalysts which can utilize larger bandwidths of the visible light spectrum. Manganese ferrite [7], zinc ferrite [8–10], aluminium doped zinc ferrite [11], manganese doped cobalt ferrite [12], barium ferrite [13], copper ferrite [14], and nickel ferrites [15, 16] have been investigated with regard to the degradation of certain dyes and other toxic compounds.

Our research group prepared and applied iron(II) doped copper ferrites $\text{Cu}_{(x)}^{\text{II}}\text{Fe}_{(1-x)}^{\text{II}}\text{Fe}_2^{\text{III}}\text{O}_4$ (where $x = 0, 0.2, 0.4, 0.6, 0.8, 1$) for the photo-induced degradation of Methylene Blue (MB) [17]. Here, a detailed photocatalytic study on the degradation of Rhodamine B is presented by using heterogeneous photo-Fenton systems and compared to homogeneous photocatalytic procedures. In addition, the antibacterial property of iron(II) doped copper ferrites in the *Vibrio fischeri* bioluminescence inhibition assay was investigated.

2. Experimental

2.1 Materials

Rhodamine B (molecular formula: $\text{C}_{28}\text{H}_{31}\text{ClN}_2\text{O}_3$) was used as a model dye for visible light-induced photocatalytic degradation. Anhydrous copper(II) sulfate, ferric chloride hexahydrate, ammonium iron(II) sulfate hexahydrate and sodium hydroxide were used to prepare the catalysts. Sodium hydroxide or hydrochloric acid was added to adjust the pH during photocatalysis. Hydrogen peroxide (30%w/w) was employed as Fenton's reagent and double distilled water used as a solvent throughout the study. All the laboratory-grade chemicals were obtained from Sigma-Aldrich (Budapest, Hungary) and used without further purification.

*Correspondence: horvath.otto@mk.uni-pannon.hu

2.2 Applied catalysts

The catalysts applied in this study were iron(II) doped copper ferrite $\text{Cu}_{(x)}\text{Fe}_{(1-x)}^{\text{II}}\text{Fe}_2^{\text{III}}\text{O}_4$ NPs (where $x = 0$ (NP-1), 0.2 (NP-2), 0.4 (NP-3), 0.6 (NP-4), 0.8 (NP-5), 1.0 (NP-6)), which were prepared by a simple coprecipitation-calcination technique. The detailed methods for the synthesis of these catalysts and their structural elucidation have been reported in our earlier studies [17, 18].

2.3 RhB photocatalytic reactions

For photocatalysis, a stock solution of 0.5 g/L RhB was prepared. In order to perform the photocatalysis, a small cuvette used as a reactor was adjusted to a S600 UV/Vis diode array spectrophotometer. The concentration of RhB (approximately 1.8×10^{-5} mol/L) in the cuvette was calculated by using the Beer-Lambert law [17].

Control experiments for the self-degradation of RhB were carried out without ferrite nanoparticles in the absence and presence of both light and hydrogen peroxide (for the oxidant effect). Then the NP catalyst of a given concentration was added to the RhB solution and stirred for 30 mins to ensure a good degree of dispersion and reach an adsorption equilibrium before photodegradation. The temperature of the photoreactor (25 ± 2 °C), concentration of RhB (1.8×10^{-5} mol/L) and duration (140 mins.) of photocatalytic experiments were kept constant. The process variables investigated were the catalyst dosage (80 to 800 mg/L), hydrogen peroxide concentration (2.2×10^{-2} to 3.0×10^{-1} mol/L) and pH (2 to 12). Meanwhile, the original pH of the total aqueous solution was approximately 7.5. The pH was adjusted by adding HCl or NaOH before starting the photocatalytic experiment.

2.4 Determination of reaction rate

The Beer-Lambert law was used to determine the reaction rate of each experiment. The spectral changes observed in the visible range of the absorption spectrum (Fig. 1) indicate that the intermediates and end products formed during the photocatalytic degradation of RhB did not produce any remarkable peaks. Therefore, the reaction rate of RhB photodegradation can be determined from the reduction in absorbance at the maximum wavelength ($\lambda_{\text{max}} = 554$ nm). The addition of heterogeneous photocatalysts caused the baseline in the recorded spectra to change as a consequence of scattering. This problem was resolved during the evaluation of the reaction rate by applying baseline corrections.

2.5 Assessment of antibacterial property

A Luminoskan Ascent microplate luminometer (Thermo Scientific) was used to measure the antibacterial property of the ferrite NPs in a *Vibrio scheri* bioluminescence

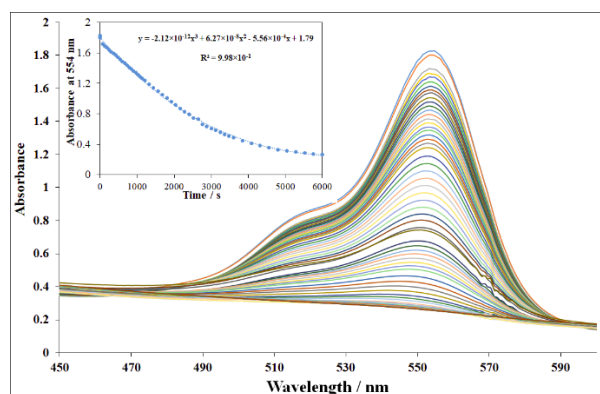


Figure 1: Spectral changes during Rhodamine B photodegradation in the presence of NP-3. The inset shows the absorbance vs. time plot at 554 nm. Experimental conditions: concentration of RhB is 1.8×10^{-5} mol/L, concentration of H_2O_2 is 1.8×10^{-1} mol/L, concentration of NP-3 is 400 mg/L, initial pH is = 7.5, and irradiation time is 140 mins.

inhibition assay. According to the manufacturer's (Hach Lange GmbH, Germany) recommendations, a test specimen of a Gram-negative *Vibrio fischeri* (NRRL-B-11177) suspension was prepared with a lifespan of 4 hours after being reconstituted. The same test protocol was followed as reported in the literature [19].

During the evaluation, the results obtained from 2 parallel measurements were averaged before the relative inhibition (%) was calculated using

$$\text{Relative inhibition } (t) = \frac{I_c(t) - I_s(t)}{I_c(t)} \times 100 \% \quad (1)$$

where $I_c(t)$ denotes the emission intensity of the control sample at time t and $I_s(t)$ represents the emission intensity of the test specimen at the same time.

3. Results and discussion

A detailed explanation regarding the control experiments concerning the photodegradation of RhB was reported in one of our previous studies [18]. The experiment used as a basis for comparisons (RhB + H_2O_2 + Light) is shown in Fig. 2.

After the control experiments, the photocatalytic efficiency of six doped ferrite nanoparticles was investigated. Fig. 1 shows the spectral changes obtained during the photocatalytic experiment using NP-3 and the decrease in the absorbance of RhB at $\lambda_{\text{max}} = 554$ nm (inset of Fig. 1). The degradation reaction of RhB follows apparent first-order kinetics (Fig. 3), which is also consistent with earlier observations regarding other catalysts [20, 21]. The slight deviation from the straight line is due to the complex nature of this heterogeneous system.

Fig. 4 reveals that all doped ferrite NPs in the series of $\text{Cu}_{(x)}\text{Fe}_{(1-x)}^{\text{II}}\text{Fe}_2^{\text{III}}\text{O}_4$ ($x = 0 - 1$) delivered higher apparent rate constants for the degradation of RhB compared to the control experiment. Doped copper ferrites

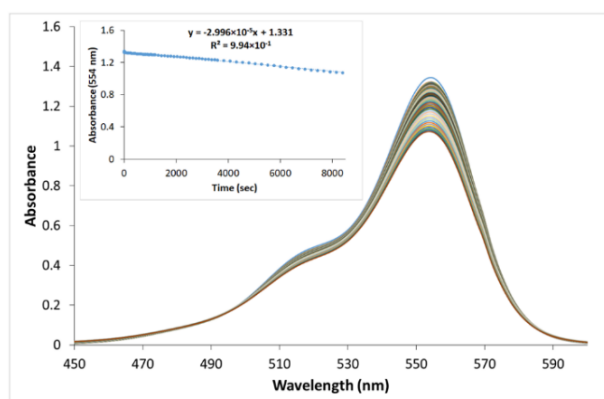


Figure 2: Spectral changes during the photodegradation of Rhodamine B in the absence of NPs. The inset shows the absorbance vs. time plot at $\lambda_{\max} = 554$ nm. Experimental conditions: concentration of H_2O_2 is 1.8×10^{-1} mol/L, concentration of RhB is 1.8×10^{-5} mol/L, and irradiation time is 140 mins.

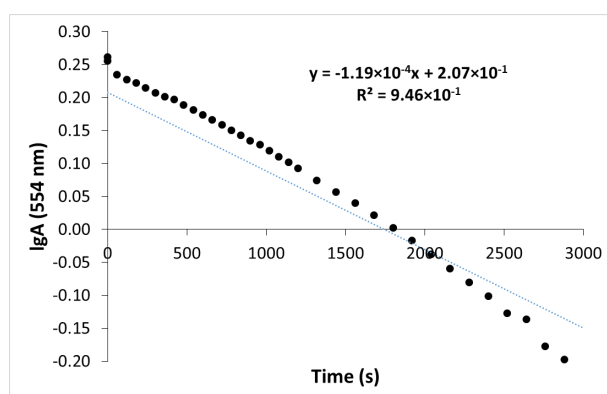


Figure 3: A plot of the logarithm of the absorbance at 554 nm vs. time for the photodegradation of RhB (see the inset of Fig. 1)

NP-2 and NP-3 exhibited outstanding photocatalytic performances in the series studied. Nickel doped cobalt ferrite NPs revealed a very similar trend with regard to the photo-oxidative degradation of RhB [22]. The higher apparent rate constants for the degradation of RhB using NP-2 and NP-3 may be attributed to their special needle-like crystalline structure [17]. On the basis of the first experimental series, NP-3 was chosen to further investigate three important determinants, namely the catalyst dosage, hydrogen peroxide concentration and pH of the heterogeneous photo-Fenton system.

3.1 The effect of catalyst dosage

Fig. 5 shows the effect of the NP-3 dosage (0–800 mg/L) on the apparent rate constant. The increase in dosage from 0–500 mg/L yielded a significant increase in the apparent rate constant. This phenomenon can be attributed to the higher number of available active sites in heterogeneous photo-Fenton processes [23]. However, increasing the dosage of NPs above 500 mg/L caused a moderate

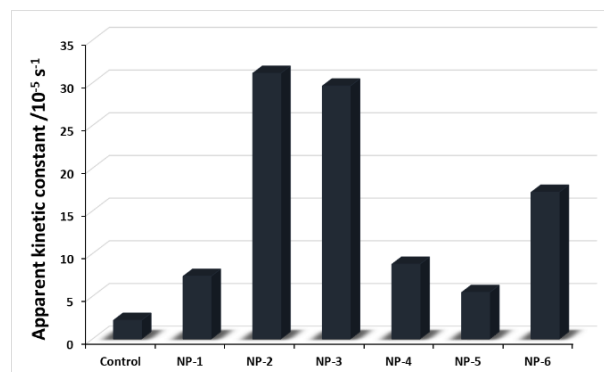


Figure 4: Photocatalytic efficiency in terms of apparent rate constants (compared to the control experiment) for NP-1 to 6. Experimental conditions: concentration of NPs is 400 mg/L, concentration of RhB is 1.8×10^{-5} mol/L, concentration of H_2O_2 is 1.8×10^{-1} mol/L, initial pH is 7.5, and irradiation time is 140 mins.

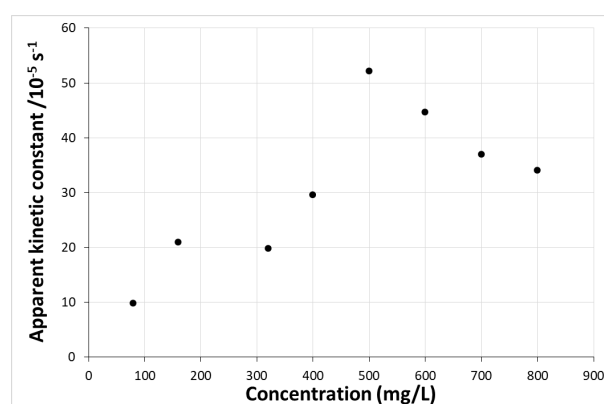


Figure 5: Effect of the concentration of NP-3 on the apparent rate constant of RhB photodegradation. Experimental conditions: concentration of RhB is 1.8×10^{-5} mol/L, concentration of H_2O_2 is 1.8×10^{-1} mol/L, initial pH is 7.5, and irradiation time is 140 mins.

decrease in the apparent rate constant, which may be attributed to the fact that higher concentrations of NPs can increase the turbidity of the reaction system, thereby hindering the absorption of light [4]. Therefore, for the photocatalytic experiments that followed, an optimum NP-3 dosage of 500 mg/L was used.

3.2 The effect of the hydrogen peroxide concentration

At first, the effect of H_2O_2 on the photodegradation of RhB in the absence of NPs was investigated (Fig. 6). The concentration of H_2O_2 was increased from 4.5×10^{-2} to 6.7×10^{-1} mol/L. The reaction rate was enhanced by increasing the concentration of H_2O_2 up to 3.5×10^{-1} mol/L. However, beyond this value, a slight decrease in the apparent rate constant was observed.

The second experimental series focused on checking the effect of increasing the concentration of H_2O_2 from 2.2×10^{-2} to 3×10^{-1} mol/L in the presence of NPs

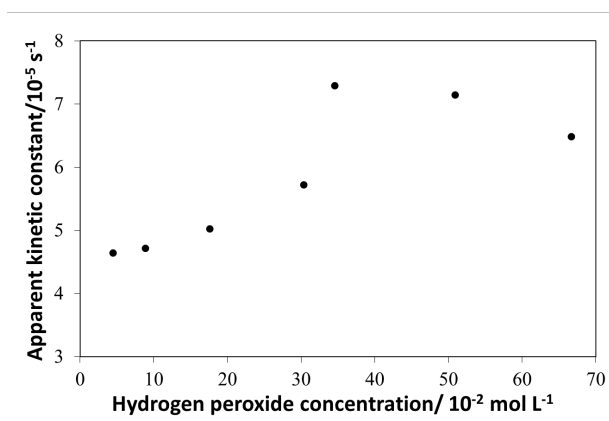


Figure 6: Effect of the concentration of H_2O_2 on the apparent rate constant of RhB photodegradation in the absence of NPs. Experimental conditions: concentration of RhB is $1.8 \times 10^{-5} \text{ mol/L}$, initial pH is 7.5, and irradiation time is 140 mins.

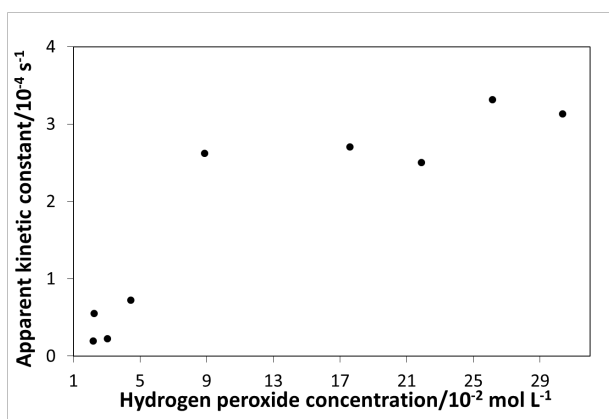


Figure 7: Effect of the concentration of H_2O_2 on the apparent rate constant of RhB photodegradation in the presence of NP-3 in a heterogeneous photo-Fenton system. Experimental conditions: concentration of RhB is $1.8 \times 10^{-5} \text{ mol/L}$, concentration of NP-3 is 500 mg/L, initial pH is 7.5, and irradiation time is 140 mins.

in a heterogeneous photo-Fenton system (Fig. 7). The reaction rate was remarkably improved by increasing the concentration of H_2O_2 up to $8.9 \times 10^{-2} \text{ mol/L}$. A further increase in the concentration of H_2O_2 did not enhance the reaction rate significantly, moreover, similar results have been published in the literature [24, 25]. The excess H_2O_2 could act as a $\bullet\text{OH}$ scavenger, producing the less reactive $\text{HO}_2\bullet$ species instead of the highly potent $\bullet\text{OH}$ [4, 23, 25]. Hence $8.9 \times 10^{-2} \text{ mol/L}$ as an optimum concentration of H_2O_2 was used in experiments on the photocatalytic degradation of RhB that followed.

3.3 The effect of pH

The surface charge properties of the photocatalyst and the ionic species present in the photocatalytic reactor are greatly influenced by the pH. Furthermore, the photodegradation efficiency of the dye is affected by the ionic

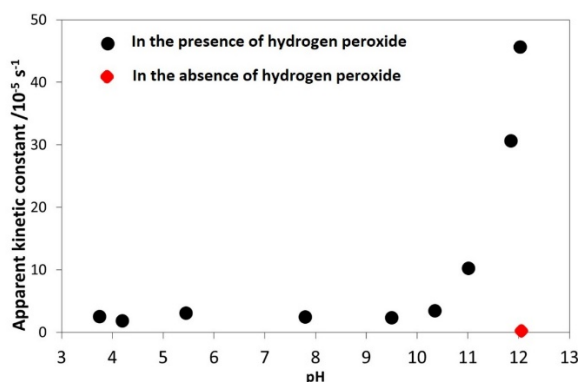


Figure 8: Effect of the initial pH on the apparent rate constant of RhB photodegradation in the absence of NPs. Experimental conditions: concentration of RhB is $1.8 \times 10^{-5} \text{ mol/L}$, concentration of H_2O_2 is $8.9 \times 10^{-2} \text{ mol/L}$, and irradiation time is 140 mins.

species and surface charge of the photocatalyst in the reaction mixture. Two experimental series were designed to study the effect of pH on the visible light-induced degradation of RhB. In the first series, the pH was varied from 3.8 to 12.1 while the concentrations of RhB and H_2O_2 were kept constant in the absence of NPs. Remarkably, neutral and alkaline pHs were found to be more effective in this system concerning RhB photodegradation (Fig. 8). In addition, the presence and absence of H_2O_2 were also investigated at higher pH values (approximately pH 12), which can be seen from the last two data points in Fig. 8. It was observed that significantly enhancing the fraction of the more reactive deprotonated form of hydrogen peroxide (HO_2^-) at higher pH values ($\text{pK}_a = 11.75$ [26]) noticeably accelerated the rate of RhB degradation. On the basis of Fig. 8, it was possible to determine the individual (apparent) rate constants (under these conditions) for the differently protonated forms of peroxide, namely $1.9 \times 10^{-5} \text{ s}^{-1}$ for H_2O_2 and $6.2 \times 10^{-4} \text{ s}^{-1}$ for HO_2^- . Deprotonation resulted in increasing the degradation effect by 32 times.

Moreover, the effect of the pH in the presence of NPs (Fig. 9) revealed that a neutral or near alkaline pH could be optimal during this type of reaction. Although the best apparent rate constant was observed at $\text{pH} \approx 8$, further increasing the pH resulted in a slight decrease in the reaction rate. By comparing Figs. 8 and 9, it can be observed that the partly hydroxylated forms of the metal ions ($[\text{Fe}^{\text{III}}(\text{OH})_2]^+$, $[\text{Cu}^{\text{II}}(\text{OH})]^+$) could also be identified at the local maximum of approximately $\text{pH} = 8$ presented in Fig. 9. Therefore, the partly hydroxylated metal ions can react with H_2O_2 , resulting in a ≈ 14 -times increase in the individual (apparent) rate constant ($2.7 \times 10^{-4} \text{ s}^{-1}$ compared to $1.9 \times 10^{-5} \text{ s}^{-1}$ for H_2O_2 in the absence of NPs).

The pH can also alter the charge state of RhB in the reaction mixture. Furthermore, at high pH values, RhB aggregates are produced as a result of the excessive concen-

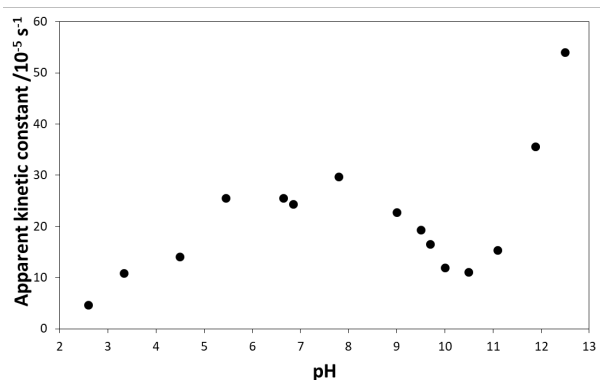


Figure 9: Effect of the pH on the apparent rate constant of RhB photodegradation in the presence of NP-3 in a heterogeneous system. Experimental conditions: concentration of NP-3 is 500 mg/L, concentration of RhB is 1.8×10^{-5} mol/L, concentration of H_2O_2 is 8.9×10^{-2} mol/L, and irradiation time is 140 mins.

tration of OH^- ions, which compete with COO^- to bind with $-\text{N}^+$. In addition, since the surface of the solid catalyst is negatively charged, it repels the RhB due to the presence of ionic COO^- groups under basic conditions. Therefore, the degradation efficiency on the surface of the photocatalyst is decreased. The same phenomenon in the case of bismuth ferrite nanoparticles has been reported in the literature [4, 27]. However, an increase in the pH above 11 significantly enhanced the reaction rate (Fig. 9) in a very similar manner to the reaction in the absence of NPs. As a result, the presence of NPs does not further increase the reactivity of HO_2^- .

In addition, the effect of light, hydrogen peroxide and NPs at an approximately constant pH is illustrated in Table 1. The light-induced degradation of RhB at pH 12 in the absence of both hydrogen peroxide and NP-3 yielded a very low reaction rate (Step 1). In Step 2, the addition of hydrogen peroxide in the absence of both light and NP-3 at pH 11.9 yielded a faster reaction rate. Step 3, which represents a heterogeneous Fenton system, yielded a much faster reaction rate. The heterogeneous photo-Fenton system shown in Step 4 yielded the best reaction rate as far as the degradation of RhB is concerned.

The catalyst NP-3 ($\text{Cu}_{(0.4)}^{\text{II}}\text{Fe}_{(0.6)}^{\text{II}}\text{Fe}_{2}^{\text{III}}\text{O}_4$) was able to overcome the disadvantage of the narrow pH range of conventional photo-Fenton processes. Based on this experimental series, the catalyst $\text{Cu}_{(0.4)}^{\text{II}}\text{Fe}_{(0.6)}^{\text{II}}\text{Fe}_{2}^{\text{III}}\text{O}_4$ is a promising candidate for the degradation of various recalcitrant dyes.

3.4 Generalized RhB degradation mechanism

A very simple schematic mechanism is proposed for the purpose of RhB degradation since the reactive species produced during irradiation, namely $\bullet\text{OH}$, H^+ and $\bullet\text{O}_2^-$, oxidize RhB molecules to intermediates of lower molecular weights. Generally speaking, the active species react

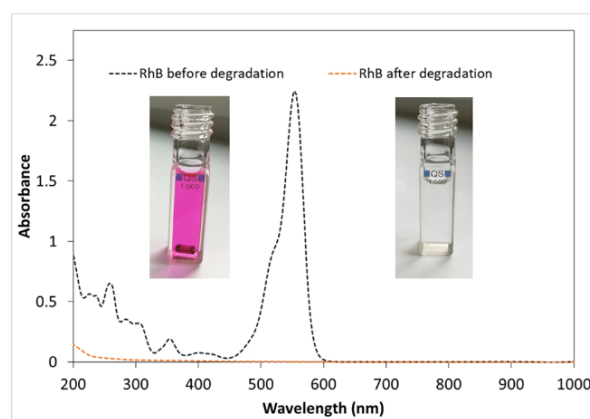


Figure 10: Visual and spectrometric comparison of RhB before and after its degradation; experimental conditions: concentration of NPs is 500 mg/L, concentration of RhB is 1.8×10^{-5} mol/L, concentration of H_2O_2 is 8.9×10^{-2} mol/L, and irradiation time is 140 mins.

with the central carbon atom in the chemical structure of RhB. Then the oxidizing agents attack the intermediates produced in the previous step, yielding smaller open-ring compounds. Subsequently, the latter compounds are mineralized to water and carbon dioxide [28]. As is displayed in Fig. 10, the UV/visible absorption spectrum of RhB degradation yields prominent peaks at 262, 358 and 554 nm. However, no significant peaks were observed following photodegradation (Fig. 10) in neither the visible nor UV region, which confirmed the complete mineralization of RhB.

The images obtained from the photoreactor (cuvette) before and after photocatalysis also confirmed the complete degradation of RhB, namely a clear, colorless solution was obtained after the removal of solid catalysts (Fig. 10) by centrifugal filtration.

3.5 Photocatalytic efficiencies under optimized conditions

Finally, the photocatalytic efficiencies of all six NPs (NP-1 to 6) were determined under optimized conditions for the degradation of RhB (Fig. 11). It was observed that all of the NPs were active photocatalysts, the application of NP-3 yielded the highest reaction rate. These results are quite comparable to those presented in Fig. 4 obtained from the first series of experiments. However, the concentration of hydrogen peroxide under the optimized conditions (8.9×10^{-2} mol/L) is considerably lower than in the first series (1.8×10^{-1} mol/L) and is, therefore, much more economical. Although the concentration of the photocatalyst is higher under the optimized conditions (500 vs. 400 mg/L), the NPs can be reused over several cycles. According to our results, all NPs in the series can potentially be applied for the purpose of environmental remediation.

Table 1: Comparison of the reaction rate and apparent rate constant at pH \approx 12 in homogeneous (Steps 1 & 2) and heterogeneous (Steps 3 & 4) systems.

Step No.	Light	Hydrogen peroxide (mol/L)	NP-3 (mg/L)	Initial pH by adding 15 μ L 1M NaOH)	Final pH	Apparent rate constant (1/s)	Comparison with basic reaction (%)
1	visible	0	0	12.1	11.7	2.6×10^{-6}	12
2	no	8.9×10^{-2}	0	11.9	11	1.6×10^{-4}	749
3	no	8.9×10^{-2}	500	11.9	11.3	2.7×10^{-4}	1256
4	visible	8.9×10^{-2}	500	11.9	11.2	3.6×10^{-4}	1642

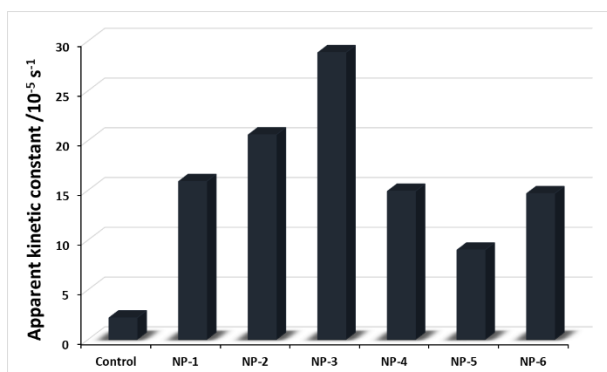


Figure 11: Photocatalytic efficiency in terms of apparent rate constants (compared to the control experiment) for NP-1 to 6. Experimental conditions: concentration of NPs is 500 mg/L, concentration of RhB is 1.8×10^{-5} mol/L, concentration of H_2O_2 is 8.9×10^{-2} mol/L, initial pH is 7.5, and irradiation time is 140 mins.

3.6 Assessment of the antibacterial activity of doped copper ferrites

The inhibition effect (%) of doped copper ferrites against Gram-negative *Vibrio scheri* in bioluminescence assays is illustrated in Fig. 12. The inhibition (%) of bacteria in the presence of doped nanoparticles containing varying ratios of copper (Cu^{II}) and iron (Fe^{II}) revealed that all doped copper ferrites yielded sufficient antibacterial activities. In our research, higher ratios of Cu^{II} proved to be useful in improving antibacterial activity. The same trend in terms of bacterial inhibition against Gram-negative *Escherichia coli* was observed using cobalt ferrite nanoparticles synthesized by co-precipitation [29].

Generally speaking, Cu^{II} can disrupt the functions of cells in several ways, hence the ability of microorganisms to develop resistance to Cu^{II} is remarkably reduced. The attachment of Cu^{II} ions to the surface of microorganisms plays a key role in their antibacterial activity [30]. The ions from the surface of doped copper ferrites, especially Cu^{II} , are adsorbed onto bacterial cell walls, damaging the cell membrane in two possible ways, namely by altering the functions of enzymes or solidifying the structures of proteins. Therefore, the presence of copper ferrites in the bacterial growth medium immobilizes and inactivates bacteria, inhibiting their ability to replicate and ultimately leading to cell death [31].

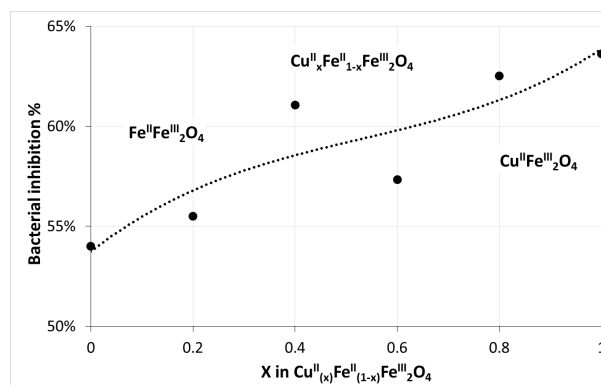


Figure 12: Comparison of the degree of bacterial inhibition using doped copper ferrites against Gram-negative *Vibrio scheri*.

In our study, a mechanism is proposed (Fig. 13) in which doped copper ferrites are attached to the cell wall of the bacterium *Vibrio fischeri*, reducing its ability to replicate. The degree of bacterial inhibition in all cases is approximately 60%, which confirms the potential application of doped copper ferrites in terms of antibacterial developments.

4. Conclusion

Iron(II) doped copper ferrites $\text{Cu}_x^{\text{II}}\text{Fe}_{(1-x)}^{\text{II}}\text{Fe}_2^{\text{III}}\text{O}_4$ have been proven to be efficient catalysts for the degradation of organic pollutants under visible-light irradiation in the presence of hydrogen peroxide. The performances of NPs with copper(II) ratios of $x = 0.2$ and 0.4 were especially promising under optimized conditions. Contrary to conventional homogeneous photo-Fenton systems, our catalysts exhibit higher efficiencies under neutral and near alkaline conditions. Besides their advantageous photocatalytic ability, these NPs also show a sufficient degree of antibacterial activity, due to their copper(II) constituents. By taking both properties into consideration, $\text{Cu}_{(0.4)}^{\text{II}}\text{Fe}_{(0.6)}^{\text{II}}\text{Fe}_2^{\text{III}}\text{O}_4$ yields the optimum combination of these features. Therefore, from the series of NPs studied in this work, NP-3 is the most promising candidate for the combined photocatalytic purification and disinfection of water.

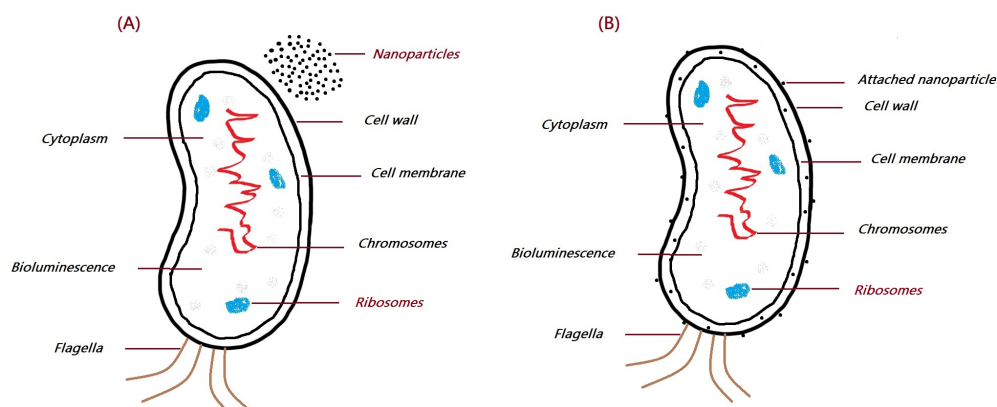


Figure 13: Proposed mechanism for the attachment of nanoparticles to *Vibrio fischeri*: bacterium and nanoparticles before (A) and after (B) attachment.

Acknowledgments

The proficient support of Prof. Dr. Éva Kristóf-Makó, Prof. Dr. Kristóf Kovács and Dr. Balázs Zsirka in terms of the structural elucidation of nanoparticle catalysts is gratefully acknowledged. This work was supported by the National Research, Development and Innovation Office of Hungary in the framework of the bilateral Hungarian-French science and technology (S&T) cooperation project 2019-2.1.11-TÉT-2019-00033).

Declaration of interest

The authors declare that they have no known competing financial interests or personal relationships that may have appeared to influence the work reported in this paper.

REFERENCES

- [1] Bao, N.; Feng, X.; Yang, Z.; Shen, L.; Lu, X.: Highly efficient liquid-phase photooxidation of an azo dye methyl orange over novel nanostructured porous titanate-based fiber of self-supported radially aligned $\text{H}_2\text{Ti}_8\text{O}_{17} \cdot 1.5 \text{H}_2\text{O}$ Nanorods. *Environ. Sci. Technol.*, 2004, **38**(9), 2729–2736 DOI: [10.1021/es034388k](https://doi.org/10.1021/es034388k)
- [2] Abdi, J.; Yahyanezhad, M.; Sakhaie, S.; Vossoughi, M.; Alemzadeh, I.: Synthesis of porous $\text{TiO}_2/\text{ZrO}_2$ photocatalyst derived from zirconium metal organic framework for degradation of organic pollutants under visible light irradiation. *J. Environ. Chem. Eng.*, 2019, **7**(3), 103096 DOI: [10.1016/j.jece.2019.103096](https://doi.org/10.1016/j.jece.2019.103096)
- [3] Horikoshi, S.; Hojo, F.; Hidaka, H.; Serpone, N.: Environmental remediation by an integrated microwave/UV illumination technique. 8. Fate of carboxylic acids, aldehydes, alkoxy carbonyl and phenolic substrates in a microwave radiation field in the presence of TiO_2 particles under UV irradiation. *Environ. Sci. Technol.*, 2004, **38**(7), 2198–2208 DOI: [10.1021/es034823a](https://doi.org/10.1021/es034823a)
- [4] Guo, S.; Zhang, G.; Jimmy, C. Y.: Enhanced photo-Fenton degradation of rhodamine B using graphene oxide–amorphous FePO_4 as effective and stable heterogeneous catalyst. *J. Colloid Interface Sci.*, 2015, **448**, 460–466 DOI: [10.1016/j.jcis.2015.02.005](https://doi.org/10.1016/j.jcis.2015.02.005)
- [5] Huang, Y.; Li, J.; Ma, W.; Cheng, M.; Zhao, J.; Yu, J. C.: Efficient H_2O_2 oxidation of organic pollutants catalyzed by supported iron sulfophenylporphyrin under visible light irradiation. *J. Phys. Chem. B.*, 2004, **108**(22), 7263–7270 DOI: [10.1021/jp036054n](https://doi.org/10.1021/jp036054n)
- [6] Dhiwaha, A. T.; Maruthamuthu, S.; Marnadu, R.; Sundararajan, M.; Manthrammel, M. A.; Shkir, M.; Sakthivel, P.; Reddy, V. R. M.: Improved photocatalytic degradation of rhodamine B under visible light and magnetic properties using microwave combustion grown Ni doped copper ferrite spinel nanoparticles. *Solid State Sci.*, 2021, **113**, 106542 DOI: [10.1016/j.solidstatesciences.2021.106542](https://doi.org/10.1016/j.solidstatesciences.2021.106542)
- [7] Luciano, A. J. R.; de Sousa Soletti, L.; Ferreira, M. E. C.; Cusioli, L. F.; de Andrade, M. B.; Bergamasco, R.; Yamaguchi, N. U.: Manganese ferrite dispersed over graphene sand composite for methylene blue photocatalytic degradation. *J. Environ. Chem. Eng.*, 2020, **8**(5), 104191 DOI: [10.1016/j.jece.2020.104191](https://doi.org/10.1016/j.jece.2020.104191)
- [8] Mandal, S.; Natarajan, S.; Tamilselvi, A.; Mayadevi, S.: Photocatalytic and antimicrobial activities of zinc ferrite nanoparticles synthesized through soft chemical route: A magnetically recyclable catalyst for water/wastewater treatment. *J. Environ. Chem. Eng.*, 2016, **4**(3), 2706–2712 DOI: [10.1016/j.jece.2016.05.020](https://doi.org/10.1016/j.jece.2016.05.020)
- [9] Mahmoodi, N. M.: Zinc ferrite nanoparticle as a magnetic catalyst: synthesis and dye degradation. *Mater. Res. Bull.*, 2013, **48**(10), 4255–4260 DOI: [10.1016/j.materresbull.2013.06.070](https://doi.org/10.1016/j.materresbull.2013.06.070)
- [10] Han, L.; Zhou, X.; Wan, L.; Deng, Y.; Zhan, S.: Synthesis of ZnFe_2O_4 nanoplates by succinic acid-assisted hydrothermal route and their photocatalytic degradation of rhodamine B under visible light.

- J. Environ. Chem. Eng.*, 2014, **2**(1), 123–130 DOI: 10.1016/j.jmrt.2020.10.080
- [11] Borhan, A. I.; Samoila, P.; Hulea, V.; Jordan, A. R.; Palamaru, M. N.: Effect of Al³⁺ substituted zinc ferrite on photocatalytic degradation of Orange I azo dye. *J. Photochem. Photobiol. A Chem.*, 2014, **279**, 17–23 DOI: 10.1016/j.jphotochem.2014.01.010
- [12] Dou, R.; Cheng, H.; Ma, J.; Komarneni, S.: Manganese doped magnetic cobalt ferrite nanoparticles for dye degradation via a novel heterogeneous chemical catalysis. *Mater. Chem. Phys.*, 2020, **240**, 122181 DOI: 10.1016/j.matchemphys.2019.122181
- [13] Roonasi, P.; Mazinani, M.: Synthesis and application of barium ferrite/activated carbon composite as an effective solar photocatalyst for discoloration of organic dye contaminants in wastewater. *J. Environ. Chem. Eng.*, 2017, **5**(4), 3822–3827 DOI: 10.1016/j.jece.2017.07.035
- [14] Tehrani-Bagha, A.; Gharagozlou, M.; Emami, F.: Catalytic wet peroxide oxidation of a reactive dye by magnetic copper ferrite nanoparticles. *J. Environ. Chem. Eng.*, 2016, **4**(2), 1530–1536 DOI: 10.1016/j.jece.2016.02.014
- [15] Goyal, A.; Bansal, S.; Singhal, S.: Facile reduction of nitrophenols: Comparative catalytic efficiency of MFe₂O₄ (M = Ni, Cu, Zn) nano ferrites. *Int. J. Hydrog. Energy*, 2014, **39**(10), 4895–4908 DOI: 10.1016/j.ijhydene.2014.01.050
- [16] Liu, S. Q.; Feng, L. R.; Xu, N.; Chen, Z. G.; Wang, X. M.: Magnetic nickel ferrite as a heterogeneous photo-Fenton catalyst for the degradation of rhodamine B in the presence of oxalic acid. *Chem. Eng. Technol.*, 2012, **203**, 432–439 DOI: 10.1016/j.cej.2012.07.071
- [17] Khan, A.; Valicsek, Z.; Horváth, O.: Synthesis, characterization and application of iron (II) doped copper ferrites (Cu_(x)Fe_(1-x)Fe₂O₄) as novel heterogeneous photo-Fenton catalysts. *Nanomaterials*, 2020, **10**(5), 921 DOI: 10.3390/nano10050921
- [18] Khan, A.; Valicsek, Z.; Horváth, O.: Comparing the degradation potential of copper (II), iron (II), iron (III) oxides, and their composite nanoparticles in a heterogeneous photo-Fenton system. *Nanomaterials*, 2021, **11**(1), 225 DOI: 10.3390/nano11010225
- [19] Szabó-Bárdos, E.; Kulcsár, P.; Kováts, N.; Békéssy, Z.; Eck-Varanka, B.; Horváth, O.: Assessment of the potential bactericide effect of self-cleaning floors: a proposed protocol. *Luminescence*, 2020, **35**(3), 434–436 DOI: 10.1002/bio.3745
- [20] Li, Y. F.; Xu, D.; Oh, J. I.; Shen, W.; Li, X.; Yu, Y.: Mechanistic study of codoped titania with nonmetal and metal ions: a case of C+ Mo codoped TiO₂. *ACS Catal.*, 2012, **2**(3), 391–398 DOI: 10.1021/cs2006668
- [21] Rahman, Q. I.; Ahmad, M.; Misra, S. K.; Lohani, M.: Effective photocatalytic degradation of rhodamine B dye by ZnO nanoparticles. *Mater. Lett.*, 2013, **91**, 170–174 DOI: 10.1016/j.matlet.2012.09.044
- [22] Singh, C.; Goyal, A.; Singhal, S.: Nickel-doped cobalt ferrite nanoparticles: efficient catalysts for the reduction of nitroaromatic compounds and photo-oxidative degradation of toxic dyes. *Nanoscale*, 2014, **6**(14), 7959–7970 DOI: 10.1039/C4NR01730G
- [23] Wang, X.; Pan, Y.; Zhu, Z.; Wu, J.: Efficient degradation of rhodamine B using Fe-based metallic glass catalyst by Fenton-like process. *Chemosphere*, 2014, **117**, 638–643 DOI: 10.1016/j.chemosphere.2014.09.055
- [24] Zhang, L.; Nie, Y.; Hu, C.; Qu, J.: Enhanced Fenton degradation of Rhodamine B over nanoscaled Cu-doped LaTiO₃ perovskite. *Appl. Catal. B Environ.*, 2012, **125**, 418–424 DOI: 10.1016/j.apcatb.2012.06.015
- [25] Salem, M. A.; Abdel-Halim, S. T.; El-Sawy, A. E.-H. M.; Zaki, A. B.: Kinetics of degradation of allura red, ponceau 4R and carmosine dyes with potassium ferrioxalate complex in the presence of H₂O₂. *Chemosphere*, 2009, **76**(8), 1088–1093 DOI: 10.1016/j.chemosphere.2009.04.033
- [26] Skounas, S.; Methenitis, C.; Pneumatikakis, G.; Morcellet, M.: Kinetic studies and mechanism of hydrogen peroxide catalytic decomposition by Cu (II) complexes with polyelectrolytes derived from l-alanine and glycylglycine. *Bioinorg. Chem. Appl.*, 2010, **2010**, 1–9 DOI: 10.1155/2010/643120
- [27] Sun, Z.; Xiao, C.; Hussain, F.; Zhang, G.: Synthesis of stable and easily recycled ferric oxides assisted by Rhodamine B for efficient degradation of organic pollutants in heterogeneous photo-Fenton system. *J. Clean. Prod.*, 2018, **196**, 1501–1507 DOI: 10.1016/j.jclepro.2018.06.122
- [28] Isari, A. A.; Payan, A.; Fattahi, M.; Jorfi, S.; Kakavandi, B.: Photocatalytic degradation of rhodamine B and real textile wastewater using Fe-doped TiO₂ anchored on reduced graphene oxide (Fe-TiO₂/rGO): characterization and feasibility, mechanism and pathway studies. *Appl. Surf. Sci.*, 2018, **462**, 549–564 DOI: 10.1016/j.apsusc.2018.08.133
- [29] Samavati, A.; Ismail, A.: Antibacterial properties of copper-substituted cobalt ferrite nanoparticles synthesized by co-precipitation method. *Particuology*, 2017, **30**, 158–163 DOI: 10.1016/j.partic.2016.06.003
- [30] Hoshino, N.; Kimura, T.; Hayakawa, F.; Yamaji, A.; Ando, T.: Bactericidal activity of catechin-copper (II) complexes against *Staphylococcus aureus* compared with *Escherichia coli*. *Lett. Appl. Microbiol.*, 2000, **31**(3), 213–217 DOI: 10.1046/j.1365-2672.2000.00800.x
- [31] Hu, C. H.; Xia, M. S.: Adsorption and antibacterial effect of copper-exchanged montmorillonite on *Escherichia coli* K₈₈. *Appl. Clay Sci.*, 2006, **31**(3–4), 180–184 DOI: 10.1016/j.clay.2005.10.010

A FRAMEWORK FOR DEMONSTRATION DEVICES USED IN DISTANCE-LEARNING ENVIRONMENTS

PÉTER DECSI^{*1}, ÁDÁM BORS¹, PÉTER KOCSOR², BÁLINT VÖRÖS², BARNABÁS HORVÁTH², SÁNDOR GUBA², ZOLTÁN GUGOLYA², SÁNDOR MESTER¹, AND ISTVÁN SZALAI^{1,2}

¹Institute of Mechatronics Engineering and Research, University of Pannonia, Gasparich Márk u. 18/A, Zalaegerszeg, 8900, HUNGARY

²Research Centre for Engineering Sciences, University of Pannonia, Egyetem u. 10, Veszprém, 8200, HUNGARY

Distance-learning has become widespread around the world. Many training areas such as engineering require the acquisition of practical rather than theoretical knowledge. In this paper, a framework is presented in the form of four pilot projects which is used for practical laboratory measurements in a distance-learning environment. Four demonstration devices consisting of an induction motor drivetrain, a magnetorheological clutch as well as a rolling resistance and an ultrasonic sensor were built and several examples of measurements presented. The system, based on accessible and user-friendly hardware, is cost-effective, simple to program and can be adapted to suit any application.

Keywords: distance learning, practice-based learning, demonstration device

1. Introduction

Remote learning provides an effective method for educators and students to remain connected and engage with learning content while working from home. Several tools are available to teach theoretical knowledge, e.g., learning management systems and video conferencing solutions. Since learning can be synchronous or asynchronous, both approaches require different tools.

The efficiency of their usage depends on how prepared the parties involved are. During the COVID-19 pandemic, educational institutions had to start using virtual environments as well as stop on-site education and were unable to provide appropriate practical training for their students. Even though remote learning can be effective, a transition from traditional methods must be made [1].

Although numerous demonstration devices have already been presented [2], few of them are capable of distance learning and many of them are only simulations [3]. Since practical training is based on self-experience, available distance learning tools are insufficient. In this paper, a universal tool is presented for distance practical training in the form of four example projects.

The demonstration devices are suitable for distance learning. The user is connected to a microcomputer through the internet, after an operator grants access to it. It provides attended and unattended access to multiple

users simultaneously, offline and cloud connectivity, file transfer as well as instant messaging (chat). The educator is able to monitor the learning path and provide instant feedback to students, which is necessary for its effective use [4].

2. Framework

Access to the front end of the framework is provided by a remote desktop client based on Virtual Network Computing (VNC) technology. The software can be run on multiple platforms; it has versions for Windows, macOS, Linux, iOS, Android, Solaris, HP-UX, and IBM AIX operating systems. The back end of the system runs on a Raspberry Pi microcomputer called the VNC Server.

The graphical user interface (GUI) of the operating system is modified on the server that enables it to be controlled using a touchscreen and remotely simultaneously. The control software of the demonstration device is written in Python which is the most common programming language nowadays. The base of the program is a GUI that uses the Tkinter Python module, moreover, the widgets are designed to be simple and readable [5]. The program is tabbed, the first tabs contain lessons and tutorials about its content. It is possible to embed videos from video sharing sites.

The teaching materials are image files, which can be created from a premade PowerPoint template. The appropriate image size, appearance, font size, etc. is set to look identical and be easily readable on multiple platforms.

*Correspondence: decsi.peter@mk.uni-pannon.hu



Figure 1: Graphical user interface of the presented framework.

The measurements, control algorithms and displays are unique to the type of demonstration device used. Only the GUI elements, e.g. buttons, sliders or labels, are provided for the programmers using the framework. In Fig. 1, the GUI of the induction motor drivetrain is presented.

The control algorithms are written in the Python language and the Integrated Development Environment (IDE) used can be chosen arbitrarily by the programmer, only the necessary Python modules need to be installed. Students can access live videos from the device to see the effects of their actions.

3. Induction motor drivetrain

Induction motors are widely used in industry due to their simple and rugged construction, cost-effectiveness as well as maintenance-free and efficient operation. Their simple and robust construction, reliability and power efficiency also fulfil the challenging requirements of the automotive industry. The key to the application of these motors is the control system. An inverter or variable frequency drive (VFD) controls the frequency and AC voltage to set the rotational speed of the motor. It provides a high starting torque as well as high level of efficiency and offers several options to work as a whole system.

Engineering students in the industry are expected to have an understanding of the working principles of an induction motor. In this demonstration device, two induction motors are mounted on a plate (Fig. 2). One of them is a three-phase two-pole squirrel cage induction motor rated at 200 W, the other is a three-phase four-pole squirrel cage induction motor rated at 120 W. The motors are driven by suitable Omron VS mini J7 VFDs. They are compact general-purpose inverters, which are simple to use as well as have several digital and analogue channels.

The larger motor has a double-sided shaft to which a DC motor is mounted and functions as a tachogenerator that measures the shaft speed, which enables the demonstration of the slip of the motor.

The digital inputs of the inverter are used in this project to enable the rotational direction selectors. The analogue input is a speed reference and the output is a current monitor related to the connected motor. The VFD is set to the V/f (voltage, frequency control) mode, so the

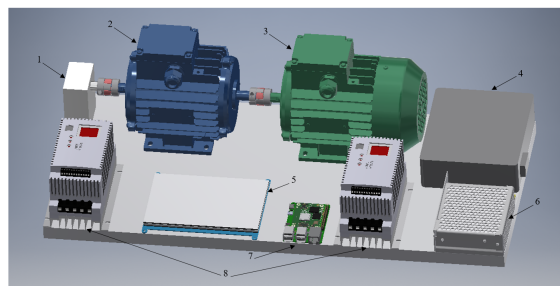


Figure 2: Demonstration device of an induction motor drivetrain. One two-pole (2) and one four-pole (3) induction motor were connected with flexible couplings. The motors were driven by frequency converters (8). A small DC motor was used as a tachogenerator (1). The power distribution network and control circuit were placed in a plastic box (4). The Raspberry Pi microcomputer (7) had a separate power supply (6) and was connected to a 7-inch display (5).

voltage and frequency is set according to the set speed by the analogue input.

An external MCP3008 Analog-to-Digital (A/D) converter and a MCP41010 8-bit digital potentiometer are connected to the Raspberry Pi. The A/D converter is used for the current monitoring and the potentiometer is used to set the reference speed in the VFD. Both integrated circuits communicate through Serial Peripheral Interface (SPI) communication with the microcomputer.

The first three tabs on the program consist of lessons concerning induction motors and VFDs as well as a tutorial for configuring the inverters. Videos are embedded in the fourth tab about induction motors and VFDs. At the time of writing, three measurement tasks are available on this device. One of them is manual control, where tasks written in the provided worksheet can be carried out. Automatic measurement tasks are located in the following two tabs, including a demonstration outlining how an induction motor can be started (Fig. 3) and example measurements of acceleration due to the centre of gravity of the eccentric mass at multiple rotational speeds.

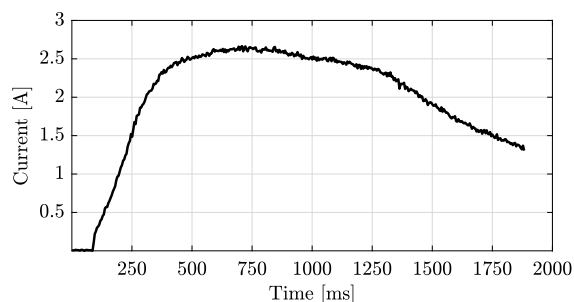


Figure 3: Measurement example of the induction motor drivetrain. The example presents the starting current of the motor as a function of time using frequency converters.

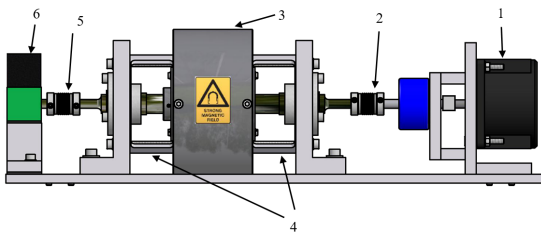


Figure 4: Demonstration device of a magnetorheological clutch. Our magnetorheological device uses an induction motor (1) as a torque source driven by a VFD, moreover, both the driver and driven parts are connected by a flexible coupling (2, 5) to the actual clutch (3). The clutch is held in place by slotted placeholders (4).

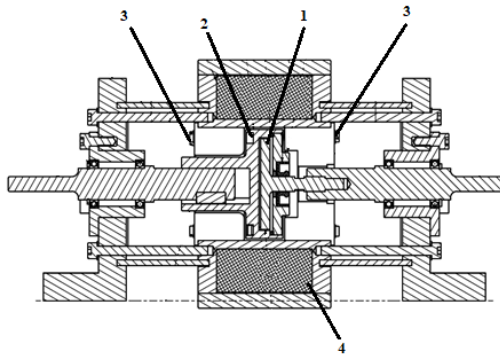


Figure 5: Schematic diagram of the magnetorheological clutch. The magnetorheological fluid was located between the input (1) and output (2) disks. The input disk was connected to the shaft by a ball bearing. The clutch was sealed by an O-ring at the output disk and an oil seal at the ball bearing. A coil (4) consisting of approximately 1200 turns of copper wire was located around the disks. The magnetic field lines were directed through the fluid with the help of magnetic flux guiders (4).

4. Magnetorheological clutch

Magnetorheological (MR) fluids are intelligent materials that exhibit the remarkable property of being able to change their rheological properties in the presence of an external magnetic field [6]. They are composed of small (10 μm) particles with permeability μ_p suspended in a carrier fluid with permeability μ_f ($\mu_f < \mu_p$). When a magnetic field is applied to the fluid, the particles acquire a magnetic dipole moment and become arranged in pairs before forming chain-like structures, which act against the shear force producing a change in the apparent viscosity. This phenomenon is used in various applications, namely in brakes [7], clutches [8], superfinishing [9], and dampers [10]. It can be used in clutches to precisely control the transmitted torque by varying the magnetic field. Magnetorheological clutches can be disk-type or cylindrical. For our demonstration, the disk-type MR clutch depicted in Fig. 4 was developed and built.

The transmitted static torque was measured indirectly by a strain gauge connected to a HX711 ADC (Analogue-

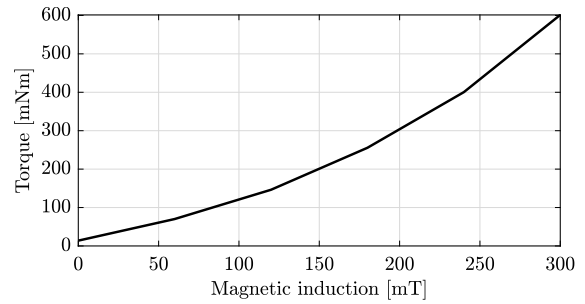


Figure 6: Measurement example of the MR clutch. The transmitted torque of the clutch at a constant speed as a function of the magnetic induction.

to-Digital Converter). Using the known force, the acting distance torque could be calculated. The induction motor was driven by a frequency converter and the coil excited by pulse-width modulation (PWM). A cross-section of the clutch can be seen in Fig. 5. The clutch can transmit approximately 0.6 Nm of torque at its maximum magnetic induction of 80 mT.

Students can measure the torque in the form of a graph as both a function of the magnetic field Fig. 6 and rotational speed using the provided sliders and displays.

5. Equipment used to measure the rolling resistance coefficient

The rolling resistance force and rolling resistance coefficient (RRC) play important roles in the automotive industry, because they are physical constants that describe the interaction between the road surface and tyres. The rolling friction is a driving resistance force that motor vehicles are subjected to which influences several parameters, including fuel consumption. The goal was to design and implement a piece of experimental equipment for demonstration purposes to measure the coefficient of rolling friction on different modelled road surfaces. The drum arrangement for measuring was chosen, which is widespread in the industry and occupies little space [11].

The measuring equipment consisted of a drum with a large diameter, which represented the modelled road surface, that was rotated by an AC induction motor; a test wheel, which was moved by linear stages; and a frame, which held the parts of the equipment together. Although the road surfaces, composed of rubber, textile and a foam-like material, were adhered to the surface of the drum, it was possible to change them.

A CAD model of the measuring equipment is shown in Fig. 7. The RRC was measured based on the measurement of the rolling resistance force. Since the rolling resistance is a force, this is the most direct method of measuring it. The rolling resistance acts on the connection point between the wheel and drum. Even though the line of action is vertical, its direction depends on the direction of rotation.

The apparatus measured the force using load cells rotated in both clockwise and anticlockwise directions be-

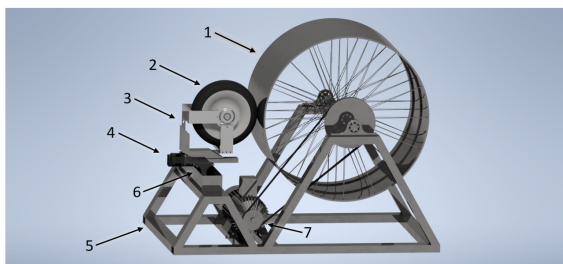


Figure 7: The CAD model of the apparatus: 1. drum using different modelled road surfaces, 2. test wheel, 3. test wheel mounted on load cells, 4. linear stage for moving the test wheel towards the drum, 5. frame, 6. linear stage for lowering the test wheel onto different surfaces, 7. AC motor driving the drum.

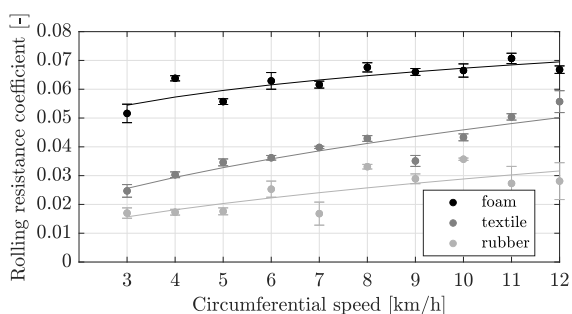


Figure 8: The rolling resistance coefficient measured on the three modelled road surfaces.

fore calculating the coefficient according to the difference between the two results. On a graphical user interface, the user can select the road surface to be modelled as well as the compressive force between the test wheel and drum. Each measurement is also presented on this graphical user interface.

Several test measurements were made using different settings and the repeatability of each measurement investigated. The RRCs on the different road surfaces are easily distinguishable and the relative standard deviations acceptable (smaller than 20%) for demonstration purposes. Although no values for these modelled road surfaces are found in the literature, the measured coefficients correspond to values measured of tyres on asphalt and dirt roads.

The dependence of the RRC on the circumferential speed, which varied between 3 km/h and 12 km/h, was investigated. Measurements on all three modelled road surfaces were made using the same parameters (20 N compressive force and 0.8 bar(g) tyre pressure). The results with descriptive statistics are shown in Fig. 8. The RRC increases proportionally to the circumferential speed as expected and is in agreement with the literature [12].

6. Ultrasonic distance measurements made by a sensor

Ultrasound are high-frequency sound waves ranging from 20 kHz to a few MHz that cannot be detected by the hu-

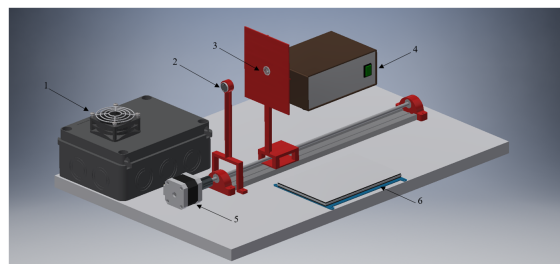


Figure 9: Measuring the ultrasonic distance. The device consisted of a fixed ultrasonic transmitter (2) and a receiver (3) moved by a linear stage driven by a stepper motor (5). The control system and circuit (1) as well as the power distribution and power supply system (4) were located in separate boxes. A 7-inch display was installed on the device (6).

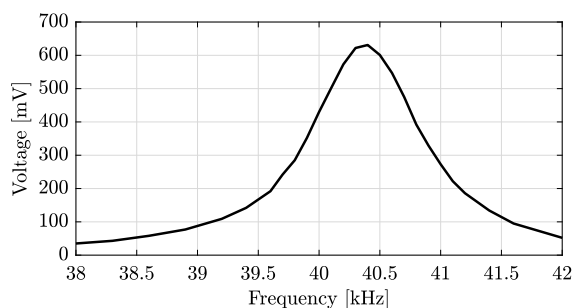


Figure 10: Example measurement made by the ultrasonic sensor demonstration device. The example shows the resonance curves of both the transmitter and receiver.

man ear. Ultrasound can be produced by piezoelectric crystals since when an AC voltage is applied across the crystals, mechanical displacement occurs. By choosing the appropriate degree of excitation, piezoelectric crystals may even exhibit ultrasonic emission. Piezoelectric crystals are polarized by mechanical deformation and the voltage can be measured between opposite plates of a crystal. As a result of vibrations (e.g., ultrasound), an alternating voltage can be measured between the opposite plates of a crystal at the same frequency as the vibrational frequency, i.e., these crystals can also act as an ultrasound receiver.

The measuring arrangement consisted of an ultrasonic transmitter and an ultrasonic receiver (Fig. 9). The distance between the transmitter and receiver could be set using a linear stage. Since the ultrasonic transmitter was driven by a PWM (Pulse-width modulation) signal, the fill factor and frequency of which could be changed, the device was suitable for two measurement tasks.

One of the measurement tasks was measuring the resonance curve (Fig. 10). The algorithm set the distance between the transmitter and receiver at 60 mm. By changing the frequency of the ultrasound emitted by the transmitter using a slider on the user interface, the resonance curve of the receiver could be determined. The amplitude of the receiver signal could be read on a pop-up window. By plotting the amplitudes as a function of frequency, both

the resonance curve and resonance frequency could be measured. The frequency could be set between 38 kHz and 42 kHz.

The other measurement task measured the amplitude of the voltage at the receiver as a function of the distance between the transmitter and receiver at the resonance frequency determined by the previous task. The distance could be set between 10 mm and 300 mm.

7. Summary

A framework for a demonstration device has been presented by four pilot projects which is capable of providing practical knowledge in distance learning environments. Since the device can connect to the Internet, students are able to complete tasks set by the educator remotely. The framework is user-friendly for both programmers and users. Only authorized persons are allowed to access the device, which also provides real-time monitoring and feedback for the educators. The framework is easily adaptable to many applications.

Acknowledgement

This study was supported by the European Union and co-financed by the European Social Fund. EFOP-3.6.2-16-2017-00002

REFERENCES

- [1] UNESCO IEASALC: COVID-19 and higher education: Today and tomorrow, Tech. Rep., UNESCO, 2020, <http://www.guninetwork.org>
- [2] Perea Martins, J.E.: An educational software for measurements demonstrations and data logging with Arduino boards, *Phys. Educ.*, 2020, **55**(6), 063004 DOI: 10.1088/1361-6552/abae25
- [3] La Rocca, P., Riggi, F., Pinto, C.: Remotely teaching Arduino by means of an online simulator, *Phys. Educ.*, 2020, **55**(6), 063003 DOI: 10.1088/1361-6552/abaa21
- [4] Wilson, G., Stacey, E.: Online interaction impacts on learning: Teaching the teachers to teach online, *Australas. J. Educ. Technol.*, 2004, **20**(1), 106675 DOI: 10.14742/ajet.1366
- [5] Richardson, R.T., Drexler, T.L., Delparte, D.M.: Color and Contrast in E-Learning Design: A Review of the Literature and Recommendations for Instructional Designers and Web Developers, Tech. Rep., **10**(4), 2014 https://jolt.merlot.org/vol10no4/Richardson_1214.pdf
- [6] Rankin, P.J., Ginder, J.M., Klingenberg, D.J.: Electro- and magneto-rheology, *Curr. Opin. Colloid Interface Sci.*, 1998, **3**(4), 373–381 DOI: 10.1016/S1359-0294(98)80052-6
- [7] Li, W.H., Du, H.: Design and experimental evaluation of a magnetorheological brake, *Int. J. Adv. Manuf. Technol.*, 2003, **21**(7), 508–515 DOI: 10.1007/s001700300060
- [8] Latha, K.H., Usha Sri, P., Seetharamaiah, N., Assistant, S.: Design and Manufacturing Aspects of Magneto-rheological Fluid (MRF) Clutch, *Mater. Today: Proc.*, 2017, **4**(4), 1525–1534 DOI: 10.1016/j.matpr.2017.01.175
- [9] Jang, K.I., Seok, J., Min, B.K., Jo Lee, S.: An electrochemomechanical polishing process using magnetorheological fluid, *Int. J. Mach. Tool. Manu.*, 2010, **50**(10), 869–881 DOI: 10.1016/j.ijmactools.2010.06.004
- [10] Guan, X.C., Guo, P.F., Ou, J.P.: Modeling and analyzing of hysteresis behavior of magneto rheological dampers, *Procedia Eng.*, 2011, **14**, 2756–2764 DOI: 10.1016/j.proeng.2011.07.347
- [11] Andersen, L.G., Larsen, J.K., Fraser, E.S., Schmidt, B., Dyre, J.C.: Rolling Resistance Measurement and Model Development, *J. Transp. Eng.*, 2015, **141**(2), 04014075 DOI: 10.1061/(ASCE)TE.1943-5436.0000673
- [12] Ehsani, M., Gao, Y., Gay, S.E., Emadi, A.: Modern Electric, Hybrid Electric, and Fuel Cell Vehicles (CRC Press), 2004 DOI: 10.1201/9781420037739

OPTIMISATION OF THE PHYSICAL PROPERTIES OF RICE HUSK ASH IN CERAMIC MATERIALS USING THE RESPONSE SURFACE METHODOLOGY

ASOTAH WISDOM^{*1}, UDOCHUKWU MARK¹, ELAKHAME ZEBERU², AND ABRAHAM ADELEKE³

¹Department of Metallurgical and Materials Engineering, Federal University of Technology, Owerri, Imo State, NIGERIA

²Federal Institute of Industrial Research Oshodi, Lagos State, NIGERIA

³Department of Materials Science & Engineering, Obafemi Awolowo University, Ile-Ife, NIGERIA

Optimisation of the physical properties of rice husk ash (RHA) in ceramic materials was carried out using Response Surface Methodology. The independent variables, namely the firing temperature and residue content, were statistically combined in a Central Composite Design with the effects on water absorption, linear shrinkage, bulk density, apparent porosity and apparent specific gravity determined. Physical and microstructural analyses were carried out to obtain information on the processes that occurred within the ceramic materials. The results obtained were analysed to determine the optimum physical properties of the ceramic materials within the range investigated. The residue content had a significant influence (at 95% confidence level) on the bulk density, water absorption, apparent porosity and apparent specific gravity but not on the linear shrinkage. The firing temperature had a more significant effect on the linear shrinkage than on the residue content, so that when elevated it contributed to an increase in linear shrinkage. The optimum residue content and firing temperature to enhance physical properties within the range investigated were 5.85% RHA and 1029.64 °C, respectively. These optimal conditions are expected to produce a ceramic material with a bulk density, linear shrinkage, apparent porosity, water absorption and apparent specific gravity of 1.64 g/cm³, 0.29%, 0.29 g/cm³, 18.26% and 2.11, respectively with a composite desirability of 100%.

Keywords: Ceramics, Rice Husk Ash, Central Composite Design, Linear Shrinkage, Water Absorption

1. Introduction

Global concerns remain with regard to how best to manage the ballooning quantity of waste materials generated on an annual basis. Waste is made up of different materials and could be classified more specifically based on its physical state (solid, liquid, gas), source (agricultural, industrial, mining) or environmental impact (hazardous and non-hazardous waste) [1]. Agricultural (food) waste is common and has been on the rise globally, with an average annual increase of between 5 and 10% [2].

Rice husk ash (RHA) is a residue generated when rice husk is burnt to ashes. Rice husk itself is a form of agricultural waste and a by-product of rice cultivation. Rice is a staple food that is widely cultivated and consumed globally. Therefore, waste generated from its production is abundant. The estimated global production from rice paddies is 600 million tonnes with 21 million tonnes of ash generated per year [3]. Open burning of the husk has a deleterious effect on the environment, polluting our air by the release of harmful gases, smoke and dust particles,

which, when inhaled, can cause respiratory diseases [2]. This has led researchers to focus on managing this waste stream to reduce potential environmental concerns.

Rice husk ash has been found to contain a very significant percentage of silica, namely about 85 – 90% [3, 4]. Given its high silica content, RHA is an excellent potential surrogate to replace quartz in triaxial ceramic bodies [5]. Research has shown that clay-based ceramics can tolerate the incorporation of waste materials in terms of their product formulation. This natural inclination has encouraged researchers to incorporate various industrial and agricultural by-products into ceramic bodies, potentially reducing environmental pollution [5–8].

The introduction of RHA as a substitute for quartz in triaxial ceramic bodies has been found to reduce the thermal expansion and maturing temperature as well as increase the glassy phase while marginally improving their strength. This reduction in the maturing temperature will lead to cost savings in terms of energy consumption, lowering overall production costs [9]. However, the introduction of this type of residue in compositions used to produce ceramic tiles needs to be further analysed. One way

*Correspondence: wisdomasotah@gmail.com

Table 1: Analysed parameters: firing temperature (FT), residue content (RC) – their levels and coded values.

Factor	Coded Levels				
	$-\alpha$	Low	Medium	High	$+\alpha$
	-1.414	-1	0	1	1.414
FT (°C)	1030	1040	1065	1090	1100
RC (%RHA)	5.85	10	20	30	34.12

of analysing the effects of replacing rice husk ash in tri-axial ceramic bodies is through the statistical design of experiments, which has many advantages over the one-factor-at-a-time method.

The factorial design of the experiment allows for the simultaneous investigation of the effects (direct and interactive) of two or more independent variables on the dependent variable [10]. Response surface methodology is a powerful statistical tool that allows researchers to develop a second-order polynomial model to determine the optimum condition for an improved response [11].

This study has dual objectives. The first is to create a mathematical model that describes the physical properties (dependent variables) as a function of the firing temperature (FT) and the residue content (RC, in unit %RHA), the independent variables. This modelling is based on the central composite design of experiments and regression analysis, an efficient statistical technique, to determine the regression coefficients that ensure the best fit of the predictive polynomial. Data analysis would involve evaluating the experimental design using various estimates of the regression matrix and model analysis. The second objective was to determine the optimum conditions (FT, RC) that improve its physical properties.

2. Experimental

The following raw materials were used in this study: rice husk collected within Epe, a town in Lagos State; as well as feldspar and kaolin sourced in the vicinity of Ogijo and Shagamu in Ogun State. To evaluate the effect of the FT and RC on the physical properties of the material, Response Surface Methodology combined with Central Composite Design were used. The Central Composite Design method consisted of two factors at two levels, namely 2^2 , which yielded 4 cube points with 4 axial (star) points and 5 center points. Minitab 19 Statistical Software (Minitab Inc., USA) was used to design the experiment and analyse the results. Table 1 presents the factors as well as their levels and coded values.

Initially, the kaolin was beneficiated by being soaked in water for 24 hours and then sieved through the mesh of a $150\ \mu\text{m}$ sieve (particles with diameters of less than $150\ \mu\text{m}$ down to submicron and nanoparticles passed through). Particles larger than $150\ \mu\text{m}$ (predominantly sand, silt and debris) were extracted. The slurry was left to stand and the excess water decanted. The wet clay was air-dried and milled using a ball mill (Model 87002



Figure 1: Fired ceramic samples.

Limongs – France A50 – 43). Feldspar rock was also milled to particle sizes of less than $150\ \mu\text{m}$. The rice husk ash was dried and sieved to particle sizes of less than $150\ \mu\text{m}$. All the sieving was conducted using a BS 410 sieve to eliminate ions and other debris.

The dry powders were measured in the right proportions according to the experimental design using the coded and uncoded values presented in Table 2 as well as a metro weighing scale with a sensitivity of 0.001 mg. Water was added and the mixture homogenized to make it workable. A quantity of the ceramic composite was put into a metal mould and placed on a press die's mantle-piece. A minimum pressure of $300\ \text{kN/m}^2$ was applied uniaxially upon the sample in the press die. The mould was constantly lubricated to facilitate the easy removal of the composite. The pressed specimens were stored overnight before being dried at $90 \pm 100\ ^\circ\text{C}$ for 48 hrs in an oven (Memmert GmbH, Germany). The dried specimens were fired in a laboratory electric furnace (Thermolyne 46200) at a rate of $5\ ^\circ\text{C}/\text{min}$ between $1000\ ^\circ\text{C}$ and $1100\ ^\circ\text{C}$ according to the phase change corresponding to the composition of the mixture. The chosen parameters for the firing cycle on a laboratory scale were adapted from the parameters used in industry.

The following physical properties were evaluated: water absorption (WA), bulk density (BD), apparent porosity (AP), apparent specific gravity (AP-SG), and linear shrinkage (LS). The LS was determined from the variation in the linear dimension of the specimen. According to Archimedes' method, WA and BD were determined using water at room temperature as the immersion fluid. The volume of open pores was determined by the AP, while the AP-SG evaluated how impervious the ceramic is to water.

The crystalline phases of the fired samples were analysed by the X-ray diffraction (XRD) technique using a Rigaku MiniFlex Benchtop X-ray Diffractometer. The fracture surfaces of the samples were morphologically characterised by Scanning Electron Microscopy (SEM) using a Phenom ProX SEM and Energy Dispersive X-ray (EDX) analysis determined the elemental composition of the samples. The fired samples are presented in Fig. 1.

3. Results and Discussion

Table 3 describes the elemental composition of the ceramic samples. By analysing the morphology and elemental composition of the various structures, information on the processes that occurred within the ceramic body when subjected to independent variables and on the nature of the minerals was obtained. EDX measurements showed that the ceramic samples were mainly composed of primary metals such as Na, K, Ca, Mg, Fe, Ag and Ti as well as non-metals like P and S – the contents of which vary between samples and even within individual samples depending on the composition of the investigated area.

The high concentrations of Si and Al are related to the raw materials, that is, rice husk ash and kaolin. Silica, an oxide of Si, is commonly found in several mineralogical clay-rich and clay-deficient phases such as kaolin, mica, feldspar and quartz. Alumina, an oxide of Al, is usually associated with some of these mineralogical phases. Potassium (K₂O) and sodium (Na₂O) oxides generally originate from feldspars, hence the presence of P and Na in the EDX data. The low content of Fe is essential to produce white ceramics since it can lead to the development of a reddish colour during sintering [6, 12].

Values of the dependent variables (observed and predicted), namely LS, WA, AP, AP-SG, and BD, from the ceramic samples are listed in Table 4. All values were calculated using the experimental planning matrix produced by Minitab 19 software. The results of the regression analysis, namely the values of the polynomial equation for the dependent variables, are shown in Eqs. 1–5 and the corresponding coefficients of the regression analysis, that is, *R*-squared (*R*²) and adjusted *R*-squared (*R*²(adj.)), are presented in Table 5.

$$\text{BD}(\text{g}/\text{cm}^3) = -28.92 + 0.015 \text{RC} + 0.0572 \text{FT} - 0.000337 \text{RC}^2 - 0.000027 \text{FT}^2 \quad (1)$$

$$\text{WA}(\%) = -25.44 + 0.0188 \text{RC} + 0.04789 \text{FT} - 0.000295 \text{RC}^2 - 0.000022 \text{FT}^2 - 0.000006 \text{RC} \times \text{FT} \quad (2)$$

$$\text{AP}_{\text{SG}} = -388.1 + 0.233 \text{RC} + 0.730 \text{FT} - 0.003957 \text{RC}^2 - 0.000341 \text{FT}^2 - 0.000062 \text{RC} \times \text{FT} \quad (3)$$

$$\text{AP}(\text{g}/\text{cm}^3) = -52.50 + 0.0348 \text{RC} + 0.0987 \text{FT} - 0.000596 \text{RC}^2 - 0.000046 \text{FT}^2 - 0.000009 \text{RC} \times \text{FT} \quad (4)$$

$$\text{LS} = -32.7 + 0.0420 \text{RC} + 0.0600 \text{FT} + 0.000104 \text{RC}^2 - 0.000027 \text{FT}^2 - 0.000042 \text{RC} \times \text{FT} \quad (5)$$

Table 6 shows the regression coefficients obtained when the observed values of LS in Table 4 were fitted to the quadratic model. The statistical significance of each independent variable on this fitting was determined using the P Value, F Statistic on its linear and quadratic terms as well as the interaction between regression coefficients. The smaller the P Value, the more significant the corresponding regression coefficient; P Value < 0.05 indicated that the regression coefficient was statistically significant at 95% confidence interval. As can be seen in Table 6, only the FT exhibited statistical significance over the range investigated. The main regression coefficients (linear and quadratic) for the RC did not show any significance. Therefore, the FT had a more significant effect on changing the LS than the RC.

The LS determines the degree of compaction and densification by analysing the linear variation with regard to the length of the sample after firing, which is essential for

Table 2: Parameters with coded and uncoded values.

Run/Sample	Coded Form of Independent Variables		Uncoded Form of Independent Variables	
	<i>X</i> ₁	<i>X</i> ₂	<i>X</i> ₁	<i>X</i> ₂
1	0	0	1065	20
2	0	-1.414	1065	5.8579
3	1	-1	1090	10
4	-1.414	0	1030	20
5	0	0	1065	20
6	1	1	1090	30
7	0	0	1065	20
8	1.414	0	1100	20
9	0	1.414	1065	34.1421
10	0	0	1065	20
11	-1	-1	1040	10
12	0	0	1065	20
13	-1	1	1040	30

*X*₁ = firing temperature (celsius); *X*₂ = residue content (%RHA)

Table 3: EDX data of ceramic samples.

Sample	Element (Atomic Concentration %)								
	9	11	4	2	13	3	6	8	7
Si	62.15	57.98	62.44	59.97	58.85	56.15	68.07	58.03	54.70
Al	21.66	27.71	17.12	26.02	24.19	29.44	18.62	28.46	29.07
Fe	3.20	2.78	3.15	2.9	4.51	3.43	1.99	3.32	3.52
K	2.48	1.65	2.72	1.57	2.33	1.75	2.15	1.48	2.19
Na	0.53	0.58	1.43	0.67	0.55	0.54	0.31	0.79	0.39

Table 4: Observed and predicted values of the linear shrinkage (LS), water absorption (WA), bulk density (BD), AP-SG (AP-SG) and apparent porosity (AP).

LS		BD (g/cm ³)		AP		AP-SG		WA	
Observed	Predicted	Observed	Predicted	Observed	Predicted	Observed	Predicted	Observed	Predicted
0.086	0.086	0.086	0.086	0.499	0.499	3.525	3.525	0.283	0.283
0.054	0.087	1.687	1.675	0.371	0.361	2.684	2.605	0.22	0.216
0.135	0.962	1.683	1.701	0.384	1.403	2.732	2.868	0.228	0.236
0.026	0.023	1.72	1.726	0.421	0.436	2.968	3.059	0.245	0.253
0.086	0.086	0.086	0.086	0.499	0.499	3.525	3.525	0.283	0.283
0.114	0.103	1.722	1.731	0.421	0.425	2.972	3.018	0.244	0.245
0.086	0.086	0.086	0.086	0.499	0.499	3.525	3.525	0.283	0.283
0.051	0.081	1.752	1.735	0.462	0.446	3.259	3.137	0.264	0.257
0.133	0.127	1.717	1.718	0.389	0.399	2.814	2.862	0.227	0.232
0.086	0.086	0.086	0.086	0.499	0.499	3.525	3.525	0.283	0.283
0.05	0.034	1.694	1.696	0.395	0.391	2.798	2.782	0.233	0.231
0.086	0.086	0.086	0.086	0.499	0.499	3.525	3.525	0.283	0.283
0.071	0.083	1.733	1.726	0.441	0.423	3.1	2.995	0.255	0.246

Table 5: Relevant statistics for the analysis of variance of the mathematical models that describe the variables BD, AP, AP-SG, WA and LS.

Variable	Model	F Statistic	P Value	R ²	R ² (adj.)
BD	Quadratic	15.78	0.001	0.92	0.86
AP	Quadratic	29.38	0	0.95	0.92
AP-SG	Quadratic	29.58	0	0.95	0.92
WA	Quadratic	30.06	0	0.96	0.92
LS	Quadratic	2.95	0.096	0.68	0.45

controlling the dimensions of the finished ceramic product [6]. The model yielded a positive value (0.06) for the regression coefficient of the FT (Eq. 5), suggesting that the FT is directly dependent on the LS. It is expected that as the temperature rises, the degree of LS increases. As the temperature rises during firing, a more significant amount of the liquid phase is produced and its viscosity decreases. This facilitates the elimination of pores, thereby increasing the extent of LS. The adequacy of the model was determined by the correlation coefficient R, which was calculated as 0.68, moreover, the high P Value and low coefficient of determination are indicative of the model's considerable degree of variability (Table 5). The data points in the normal percentage distribution curves shown in Fig. 2 lie close to the line indicating no significant deviation from normality nor any need for response

Table 6: Statistics for the analysis of the variance of the model that describes linear shrinkage (LS).

Model Term	Regression Coeff.	P Value	F Statistic
Intercept	-32.7	-	-
RC	0.042	0.144	2.7
FT	0.06	0.047	5.78
RC ²	0.000104	0.292	1.3
FT ²	-0.000027	0.102	3.54
RC×FT	-0.000042	0.411	0.76

transformation. The residual versus fitted plot should resemble a scatter plot as shown in Fig. 3. If the plots do not present a random scattering of data as represented in Fig. 2, then any trends will indicate flaws in the assumptions [6, 11].

Regression coefficients obtained when the observed values of BD, WA, AP and AP-SG were fitted in the quadratic model are shown in Tables 7–10, respectively. The main independent variable, namely the FT, did not exhibit any significance over the range investigated. Among the interacting regression coefficients shown in Tables 7–10, interactions between the RC and FT were not found to be statistically significant.

The WA capacity is directly related to the type of microstructure that developed while the samples were sin-

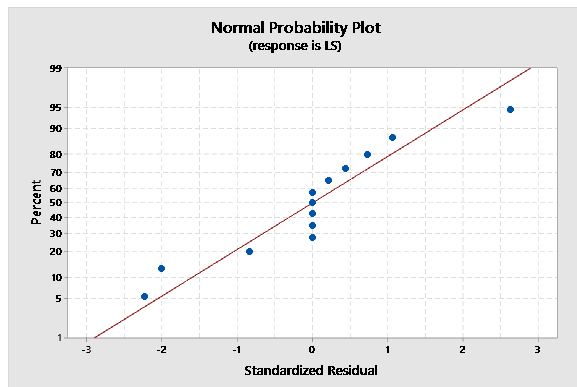


Figure 2: Normal probability plot of the residual plot for linear shrinkage (LS).

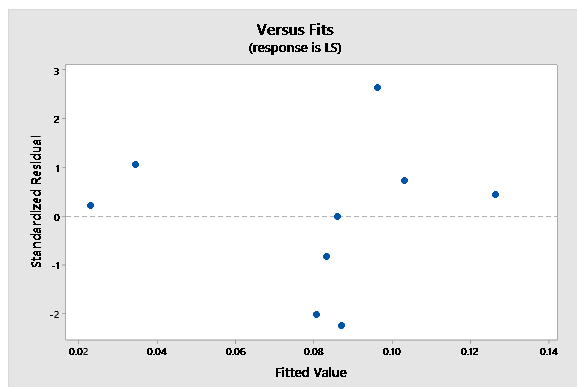


Figure 3: Residual plot against the fitted plot for linear shrinkage (LS).

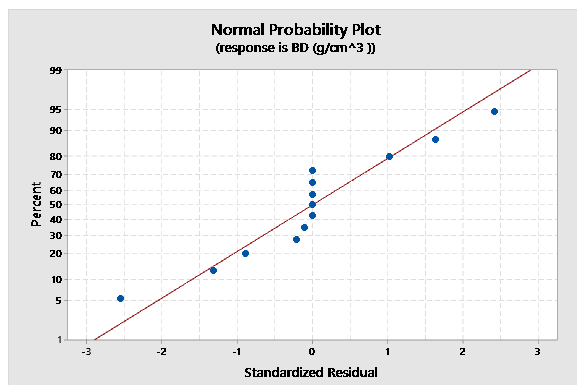


Figure 4: Normal probability plot of the standardized residual of the bulk density (BD).

tering and its level of porosity. This is regarded as a simple way to predict the technological properties of the final products [6, 13]. Within the range investigated, the RC was shown to be more dependent on the WA, BD, AP and AP-SG, which is in good agreement with the model prediction.

The adequacy of this prediction is confirmed by the coefficient of determination, R^2 , values of BD, AP, AP-SG and WA which were calculated to be 0.92, 0.95, 0.95 and 0.96, respectively (Table 5). The high values of R^2 given as 0.86, 0.92, 0.92 and 0.92 (Table 5) indicate that the adjusted models do not present a considerable degree of variability. This is also evident on the normal percent-

Table 7: Statistics for analysis of variance of the model that describes the bulk density (BD).

Model Term	Regression Coeff.	P Value	F Statistic
Intercept	-28.92	-	-
RC	0.015	0.008	13.14
FT	0.0572	0.506	0.49
RC ²	-0.000337	0	57.44
FT ²	-0.000027	0.007	14.15
RC×FT	0	1	0

Table 8: Statistics for analysis of variance of the model that describes water absorption (WA).

Model Term	Regression Coeff.	P Value	F Statistic
Intercept	-25.44	-	-
RC	0.0188	0.043	6.08
FT	0.04789	0.593	0.31
RC ²	-0.000295	0	128.25
FT ²	-0.000022	0.001	28.88
RC×FT	-0.000006	0.676	0.19

Table 9: Statistics for analysis of variance of the model that describes apparent specific gravity (AP-SG).

Model Term	Regression Coeff.	P Value	F Statistic
Intercept	-388.1	-	-
RC	0.233	0.031	7.23
FT	0.73	0.447	0.65
RC ²	-0.003957	0	119.58
FT ²	-0.000341	0.001	34.79
RC×FT	0.000062	0.755	0.11

Table 10: Statistics for analysis of variance of the model that describes apparent porosity (AP).

Model Term	Regression Coeff.	P Value	F Statistic
Intercept	-52.5	-	-
RC	0.0348	0.03	7.33
FT	0.0987	0.522	0.45
RC ²	-0.000596	0	123.29
FT ²	-0.000046	0.001	28.91
RC×FT	-0.000009	0.76	0.1

age distribution curve and the residuals versus fits plot (Figs. 4 and 5, respectively), which show that the data set is normally distributed and falls within $(-2, 2)$ for BD. Furthermore, similar plots are produced for WA, AP and AP-SG with a statistical significance of 95% and less than 5% as outliers observed.

Fig. 6 shows the XRD patterns of the ceramic samples with RCs of 5.85% and 34.14%, that is, the lowest and highest RCs studied in the present work. According to the XRD patterns, all the ceramic samples consisted of similar minerals, namely kaolinite $[\text{Al}_2\text{Si}_2\text{O}_5(\text{OH})_4]$, montmorillonite $[\text{NaMgAlSiO}_2(\text{OH})\text{H}_2\text{O}]$, suessite $[\text{Fe}_3\text{Si}]$, and illite $[\text{KAl}_2\text{Si}_3\text{AlO}_{10}(\text{OH})_2]$. With RCs of 34.14%,

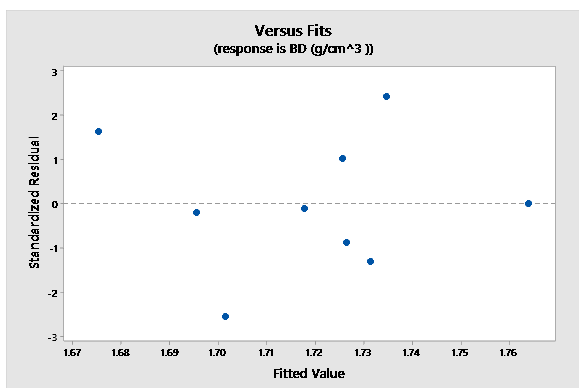
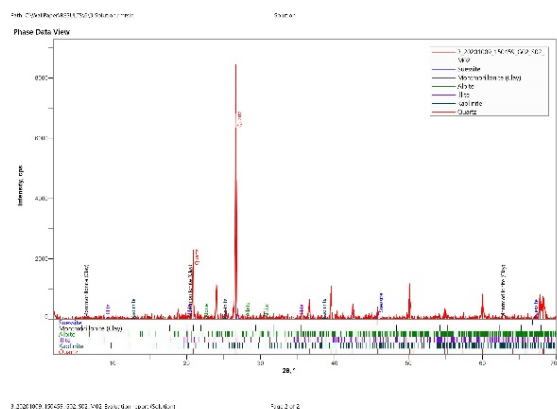
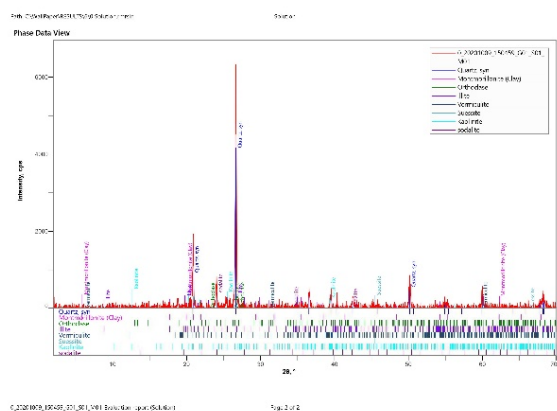


Figure 5: Plot of the standardized residual against the fitted values of the bulk density (BD).



(a) 5.86% RHA



(b) 34.14% RHA

Figure 6: XRD patterns of samples against their RCs (%RHA).

orthoclase and synthesised quartz were present. Quartz exhibited the highest peak, which confirms the high concentration of Si according to the EDX data. Little or no difference was detected between the intensities of the peaks. All ceramic samples contained clay minerals; quartz, kaolinite, illite and albite are the mineral phases of the raw materials used.

The micrograph (Fig. 7) shows that the ceramic matrix of samples sintered at higher temperatures (1090 °C

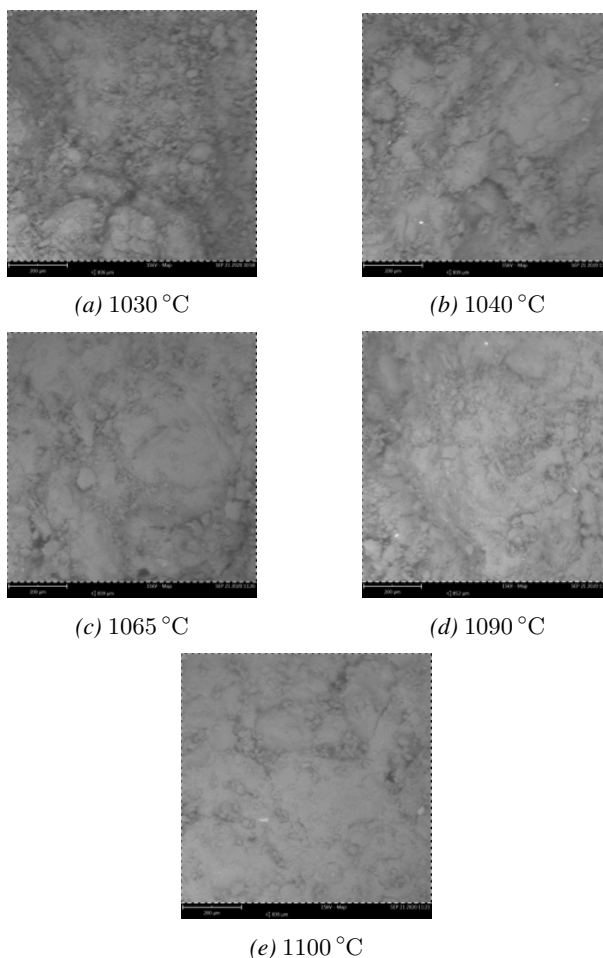


Figure 7: SEM micrograph of fracture surfaces of ceramic samples against RC.

and 1100 °C) was more finely dispersed and densely packed. A reduction in porosity was observed compared to samples sintered at lower temperatures (1030 °C, 1040 °C and 1065 °C) which were more porous and irregular as at higher sintering temperatures. As observed, increase in FT led to an increase in vitreous phase, facilitating the elimination of pores and an increase in densification. This hypothesis is in good agreement with other research [6, 12, 13].

3.1 Response optimisation

The optimised responses with regard to the physical properties of ceramics in which rice husk ash is used as a silica precursor and their criteria are presented in Table 11, moreover, the desired quality is shown in Fig. 8. From the optimisation results and plot presented in Fig. 8, the optimum RC and FT to achieve the desirable physical properties are 5.85% and 1029.64 °C, respectively. These optimal conditions are expected to produce a ceramic product with a BD of 1.64 g/cm³, LS of 0.29, AP of 0.29 g/cm³, WA of 18.26%, and AP-SG of 2.11.

The optimal combination of the factors shown in Fig. 8 effectively maximises the LS as well as minimises the

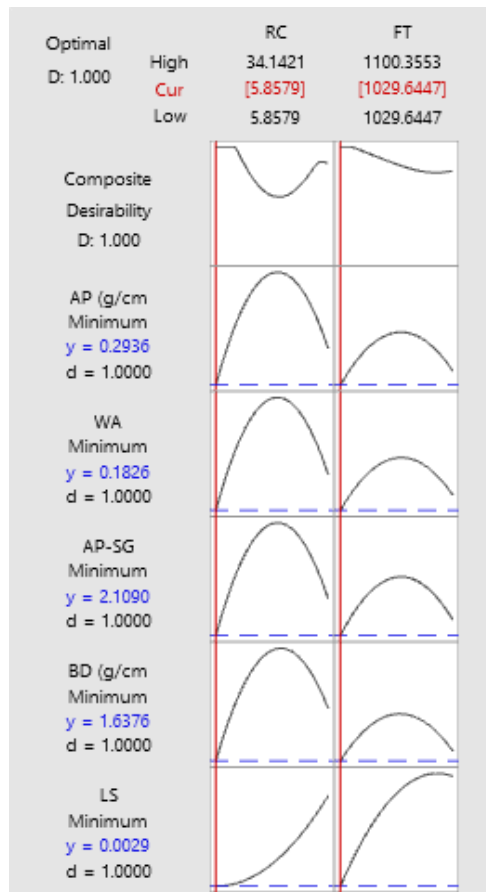


Figure 8: Optimisation plot of the variables.

BD, WA, AP-SG, and AP. The composite desirability of 100% showed how the settings optimise all five quality responses when they are considered as objective response functions simultaneously [11].

4. Conclusions

The physical properties of the ceramic samples using the response surface methodology were optimised. The modelling was based on central composite design and it was

Table 11: Criteria and results of the optimisation of the process conditions.

Response	Goal	Response	Desirability
Linear Shrinkage (%)	Minimum	0.29	100%
Bulk Density (g/cm ³)	Minimum	1.64	100%
Apparent Porosity (g/cm ³)	Minimum	0.29	100%
Apparent Specific Gravity	Minimum	2.11	100%
Water Absorption (%)	Minimum	18.26	100%

Composite desirability = 100%

possible to obtain significant mathematical models which correlate the factors FT and RC with the dependent variables LS, WA, AP, AP-SG, and BD. The FT had a statistically significant effect on the LS so that raising the temperature enhanced the degree of shrinkage. However, the RC had a more significant effect on the BD, AP, AP-SG, and WA. It can be concluded that the optimum physical properties within the range investigated are a BD of 1.64 g/cm³, LS of 0.29, AP of 0.29 g/cm³, WA of 18.26%, and AP-SG of 2.11 with a RC of 5.85% and a FT of 1029.64 °C. The composite desirability to achieve the optimal settings is 100% and yielded favourable results for all responses when the objective functions were considered simultaneously.

REFERENCES

- [1] Amasuomo, E.; Baird, J.: The concept of waste and waste management, *J. Manage. Sust.*, 2016, **6**(4), 88–96 DOI: 10.5539/jms.v6n4p88
- [2] Wang, B.; Dong, F.; Chen, M.; Zhu, J.; Tan, J.; Fu, X.; Wang, Y.; Chen, S.: Advances in recycling and utilisation of agricultural wastes in China: Based on environmental risk, crucial pathways, influencing factors, policy mechanism. *Procedia Env. Sci.*, 2016, **31**, 12–17 DOI: 10.1016/j.proenv.2016.02.002
- [3] Jamo, U.; Maharaz, M. N.; Pahat, B.: Influence of addition of rice husk ash on porcelain composition. *Sci. World J.* 2015, **10**(1), 7–16 <https://www.ajol.info>
- [4] De Silva, G. H. M. J. S.; Surangi, M. L. C.: Effect of waste rice husk ash on structural, thermal and run-off properties of clay roof tiles. *Constr. Build. Mater.*, 2017, **154**, 251–257 DOI: 10.1016/j.conbuildmat.2017.07.169
- [5] Correia, S. L.; Dienstmann, G.; Folgueras, M. V.; Segadaes, A. M.: Effect of quartz sand replacement by agate rejects in triaxial porcelain. *J. Hazard. Mater.*, 2009, **163**(1), 315–322 DOI: 10.1016/j.jhazmat.2008.06.094
- [6] Silva, K. R.; Campos, L. F. A.; de Lima Santana, L. N.: Use of experimental design to evaluate the effect of the incorporation of quartzite residues in ceramic mass for porcelain tile production. *Mater. Res.*, 2018, **22**(1), 1–11 DOI: 10.1590/1980-5373-MR-2018-0388
- [7] Bragança, S. R.; Vicenzi, J.; Guerino, K.; Bergmann, C. P.: Recycling of iron foundry sand and glass waste as raw material for production of whiteware. *Waste Manage. Res.*, 2006, **24**(1), 60–66 DOI: 10.1177/0734242X06061155
- [8] Ogunro, A. S.; Apeh, F. I.; Nwannenna, O. C.; Ibhado, O.: Recycling of waste glass as aggregate for clay used in ceramic tile production. *Am. J. Eng. Res.*, 2018, **7**(8), 272–278 <http://www.ajer.org>
- [9] Vernon, E.: Substitution of rice husk ash for quartz in ceramic wall tiles (PhD Thesis), Department of Industrial Design 2015

- [10] Halim, R.; Webley, P. A.: Nile red staining for oil determination in microalgal cells: A new insight through statistical modelling. *Int. J. Chem. Eng.*, 2015, **2015**(695061) DOI: [10.1155/2015/695061](https://doi.org/10.1155/2015/695061)
- [11] Ogunbiyi, M. O.: Optimisation of parboiling process using response surface methodology (RSM) to improve the physical properties of parboiled milled rice. *Int. J. Eng. Res. Technol.*, 2018, **V7**(07), 312–318 DOI: [10.17577/ijertv7is070117](https://doi.org/10.17577/ijertv7is070117)
- [12] Oancea, A. V.; Bodi, G.; Nica, V.; Ursu, L. E.; Droboata, M.; Cotofana, C.; Vasiliu, A. L.; Simionescu, B. C.; Olaru, M.: Multi-analytical characterization of cucuteni pottery. *J. Eur. Ceramic Soc.*, 2017, **37**(15), 5079–5098. DOI: [10.1016/j.jeurceramsoc.2017.07.018](https://doi.org/10.1016/j.jeurceramsoc.2017.07.018)
- [13] Torres, P.; Manjate, R. S.; Quaresma, S.; Fernandes, H. R.; Ferreira, J. M. F.: Development of ceramic floor tile compositions based on quartzite and granite sludges. *J. Eur. Ceramic Soc.*, 2007, **27**(16), 4649–4655 DOI: [10.1016/j.jeurceramsoc.2007.02.217](https://doi.org/10.1016/j.jeurceramsoc.2007.02.217)

COMPARATIVE STUDY ON ANAEROBIC DEGRADATION PROCESSES OF PRESSED LIQUID FRACTION OF ORGANIC SOLID WASTE

TAMÁS RÓZSENBERSZKI^{*1}, LÁSZLÓ KOÓK¹, PÉTER BAKONYI¹, NÁNDOR NEMESTÓTHY¹, AND
KATALIN BÉLAFI-BAKÓ¹

¹Research Centre for Biochemical, Environmental and Chemical Engineering, University of Pannonia,
Egyetem u. 10, Veszprém, 8200, HUNGARY

Anaerobic degradation processes: anaerobic digestion (biogasification), biohydrogen fermentation (dark) and microbial fuel cells were applied to treat the organic fraction of a municipal solid waste. The processes were compared based on their ability of energy recovery and Chemical Oxygen Demand reduction.

Keywords: organic waste, anaerobic biodegradation, microbial fuel cell, energy recovery, process comparison

1. Introduction, background

1.1 Waste challenges

The world population has more than doubled over the last 60 years. Due to this growing tendency and urbanization the world's energy consumption and value of waste generation present us with major challenges with sustainable development in mind. Furthermore, it is obvious that waste treatment is one of the most critical global issue, because it has significant impacts for the health, local and global environment and economy [1]. According to the World Bank Group, 2.01 billion tonnes of municipal solid waste (MSW) around the world are generated annually, and at least one third of that is not managed environmentally acceptable manner [2]. The average waste generated per person per day is 0.74 kilogram, but there are significant differences between data by countries, from 0.11 to 4.54 kilograms. Actually, high-income countries only cover for 16 percent of world's community, although generate around 34 percent of the world's waste. Based on their estimation global waste will grow to 2.2 billion tonnes by 2025 and to 3.40 billion tonnes by 2050 [1, 2]. These facts make solid waste management (SWM) is a challenging task for decision-makers, who are required to provide essential waste collection and disposal services, generally under increasingly stringent budgetary pressures and regulatory requirements [3].

1.2 Biowaste

MSW typically consists of food waste, paper, glass, metals, plastics, textiles, etc. In developed countries the

amount of paper and plastics are relatively higher than the case of developing countries, where the main part of MSW is organic waste [4]. There are variations in the characteristics of MSW across the world, but remarkable part of the municipal solid waste is containing biodegradable organic components (world average: 46%) [1, 5]. There is a variety of treatment alternatives that provide not only disposal of this organic part but also energy recovery options. This section is going to present some anaerobic biodegradation processes so the following part of this section will focus on the organic waste.

Based on the data of the Food and Agriculture Organization roughly one-third of food produced for human consumption is lost or wasted globally, which amounts more than 1.2 billion tons per year [6, 7]. In the European Union, more than 85 million tonnes of food waste are generated per year with associated costs estimated at around 143 billion euros [7, 8]. According to San Martín et al. vegetable waste deposited as landfill could be reduced to 30% [9]. Some studies in this topic have indicated that vegetable waste has a remarkable potential for use as a raw material for animal feed. For example, Garcia et al. concluded that some part of various organic wastes (meat, fish, restaurant and household waste, fruit and vegetable) was possible to use in animal feed formulations [10].

1.3 Treatment processes for the municipal solid waste

It is important to notice the reduction of the waste problem should be started at the prevention and reduce the level of the overconsumption. However, in our consumer

*Correspondence: rozsenberszki.tamas@uni-pannon.hu

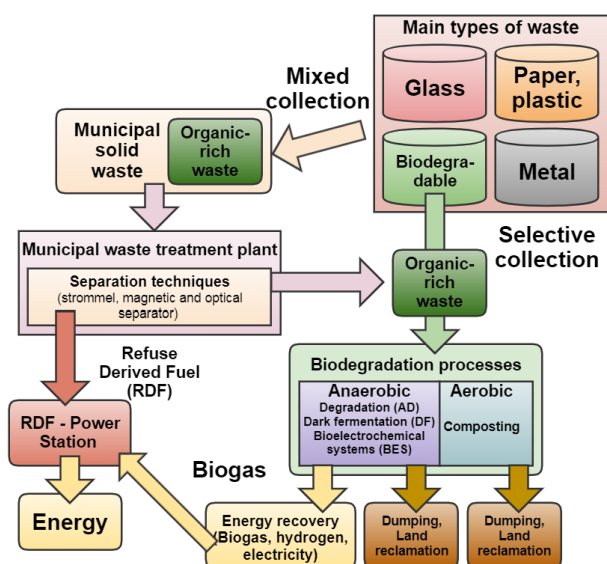


Figure 1: Schematic illustration of an example how to integrate bioprocesses in the MBT for the efficient MSW treatment

society today the market sphere is not interested in the reduction of the consumption, because the drop of consumption means less profit. It is still common to dump the treated or not treated waste, instead of produce valuable products to sell commercially or for own use, possibly recover energy from them [11]. Waste dumping seems convenient and cheap solution but in the long term it is unprofitable and unsustainable technique. As long as this practice is followed, efforts should be made to continue the development such research that can minimize the negative effects of excess use. In the case of society it is an important task to focus on how can expand the environmental friendly thinking already from the basic education.

Fig. 1 presents the main treating processes of the MSW. In most cases the aim is to reduce the toxicity of the waste in addition energy generation and in the case of composting soil conditioners could be recovered. The most unpreferable technique of them is the waste dumping without gas collection or recovery [12]. Somewhat better choice is the landfilling which is currently the main technological facility applied to treat and dispose MSW worldwide. But this represents still low level based on the waste treatment hierarchy [13, 14]. Although landfill seems a cheap alternative, it can pollute the surrounding area (air, soil and also the water). Over the years the collected landfill gas has limited use (no more than 60% methane content) [15]. Landfill gas with low CH_4 content (low calorific gas) is difficult to directly burn so it does not seem to be the best solution [15]. The thermal processes can reduce significantly the volume of the waste but the cost of the plant installation and operation is relatively high. Moreover the flue gas and ash resulted need further treatments from environmental point of view [12].

1.4 Biodegradation processes for waste treatment

In the case of aerobic biological methods composting can stabilize the organic waste and could produce soil conditioners but the bound energy of the waste cannot be utilized. On the other hand it needs relatively large area and longer time to get valuable products [4]. Nevertheless, due to the comparatively simple operation it is still a widely used technique for the treatment of organic rich fraction.

Staying on the biological line the anaerobic digestion (AD) or biogasification is operating under anaerobic conditions. Consequently, organic matter is degraded by a microbial community consisting of bacteria in the absence of oxygen and generating methane, carbon dioxide, and useable residue without any exothermic heat. It seems advantageous to choose AD because the biogas (around 60 – 70% methane content) and biomethane are economically more valuable products than compost or the landfill gas. In addition the residue resulted by an anaerobic process integrated with an aerobic stage has the same quality parameters like compost [16].

Before the installation of an AD system it is necessary to focus on the typical waste composition for the area because it can show significant diversity. It is not a simple process but there are modelling possibilities. According to Cermiato et al. these combined bioprocesses including AD and digestate composting resulted higher performance than those applied pure composting [16]. In addition AD usually causes lower environmental impact than composting because it can fulfill two levels of the waste hierarchy at the same time. Actually, the biodegradable waste (e.g., food loss, green waste) can be considered as a type of sustainable resources. In this view through AD process the energy is generated by a renewable source (biowaste) thus avoiding the energy which produced from conventional or fossil sources. Generally around 120 m^3 of biogas can be produced with a total electricity yield of about 250 kWh and a net electricity yield of 204 kWh from one ton of biowaste [16].

Fei et al. carried out life cycle assessment on MSW treatment technologies. Results showed that the mechanical-biological treatment (MBT) had higher efficiency than landfill and incineration [17]. According to the life cycle assessment the worst option was the raw land filling. The incineration had a higher energy efficiency (20.5% energy recovery) but in this case the large amount of fly ash and exhaust treatment caused more environmental impacts. It seemed the MBT had the highest energy efficiency (38.5%) when it combined with biogas purification method. Montejo et al. found similar results about connection MBT and AD [18]. In addition, MBT had less environmental impacts and relatively good stability for the changing composition of MSW. On the other hand, MBT had weak economy performance and required economy support policy.

Table 1: Main types of the municipal solid waste treatment [12]

Treatment process	Thermal treatment			Biological treatment			Landfilling	
Method	Incineration	Pyrolysis	Gasification	Refuse derived fuel	Anaerobic digestion	Composting	Landfill with gas recovery	Landfill without gas recovery
Product	Heat, Power	Gas, Oil, Charcoal	Syngas	Heat, Power	Biogas	Compost	Landfill gas	-
Energy recovery	yes	yes	yes	yes	yes	no	yes	no

Table 2: Summary of the results coming from the sample utilization by various anaerobic degradation methods

Process	AD	HDF	MFC
Amount of sample (cm ³)	25	25	25
Volume of inoculum (cm ³)	25	25	25
Valuable product	methane*(299 cm ³)	hydrogen*(91 cm ³)	electricity
Theoretical energy recovery**	11.7 kJ	1.14 kJ	0.031 kJ
Particular energy recovery***	4.1 kJ	0.8 kJ	0.031 kJ
Operation time (day)	40	2	30
Reduction of COD	medium	low	high

* Referring to standard temperature and pressure

** Referring to maximal utilization rate with no losses

*** Referring to utilization with losses: AD: biogas motor, HDF: fuel cell, MFC: direct use

2. MBT with other anaerobic processes

In this subsection a particular example for an integrated anaerobic treatment is presented. A special sample coming from the organic fraction of a municipal solid waste was studied [19–21]. Actually it was concentrated organic rich wastewater produced from mixed collected solid waste by pressing in a MBT plant (Királyszentistván). During the MBT separation technology a biodegradable fraction generated called biofraction utilized by the Plant's biological stabilizing hall (compostation) to treat it before the dumping (Fig. 1). The aim was to utilize the sample (before the composting process) with different anaerobic biodegradation methods to reduce the organic content and produce energy or valuable products (hydrogen, methane). Thus the volume of waste will decrease (from the aspect of environmental protection) whilst the energy content of the waste can be exploited.

In the first stage of experimental work the sample was characterized by analytical methods. It has high Chemical Oxygen Demand (COD) and Biochemical Oxygen Demand (BOD) content 111 g L⁻¹ and 61 g L⁻¹ respectively, which parameters are promising for the biological treatment used. The various methods were the anaerobic digestion (AD), biohydrogen dark fermentation (HDF) and a kind of bioelectrochemical system (BES): the microbial fuel cell (MFC). As an inoculum mesophilic sludge from a biogas plant was used in each cases. The details about the materials and methods used were described in our previous studies [19–21].

Based on the experiments presented in Table 2, AD seems to be the most preferable method to integrate in the MBT process. It resulted high cumulative energy recovery

(11.7 kJ) and medium COD removal, but it needs long time for the degradation mechanism (methanogenic pathways). HDF lasted a few days and during the process 1.14 kJ cumulative energy was generated however the COD removal was in low level, thus the effluent needed further treatment. There were successful experiments where AD and MFC were combined to treat the COD of the effluent from HDF. On the other hand HDF is a promising method if the desired final product is the hydrogen which is otherwise an encouraging energy sources for the future [22]. During the two chambered MFC process direct electrical energy was generated, but it had lot of limitation factors including type and structure of the system, electrode materials used, type of membrane, external and internal resistant, operation and adaptation period, biofouling, etc. Our results showed that if MFC system was integrated to HDF or AD the system's energy recovery (coulombic efficiency) and COD removal could be higher.

3. Conclusion

In many countries the waste management still does not get enough attention. The technologies of the biowaste treatment are already known just need to optimize for the characteristics of the waste streams in that area. Decision makers should choose the sustainable and low risk ways for the environment. The results of our and other experimental works showed that MBT combined with anaerobic degradation processes could be an acceptable way to the clean and economical treatment in the case of significant amount of mixed collected MSW. However, selectively collected biowaste has even more potential to maximize the recovery of their energy content. Depending on the composition of the waste it may be advantageous to

integrate the different treatment methods to improve for an appropriate level of the effectiveness.

Acknowledgements

The authors thank for the financial support provided by the Széchenyi 2020 Programme under the project EFOP-3.6.1-16-2016-00015, and by the Excellence of Strategic R+D Workshops under the project GINOP-2.3.2-15-2016-00016 entitled “Development of modular, mobile water treatment systems and wastewater treatment technologies based at the University of Pannonia to enhance growing dynamic exportation from Hungary between 2016 and 2020”.

REFERENCES

- [1] Hoorweg, D.; Bhada-Tata, P.: What a Waste: A Global Review of Solid Waste Management. Urban Development Series. Knowledge Papers No. 15, World Bank, 2012, 1. <https://openknowledge.worldbank.org>
- [2] Kaza, S.; Yao, L.C.; Bhada-Tata, P.; Van Woerden, F.: What a Waste 2.0: A Global Snapshot of Solid Waste Management to 2050. World Bank Publications, 2018. DOI: 10.1596/978-1-4648-1329-0
- [3] Roberts, K.P.; Turner, D.A.; Coello, J.; Stringfellow, A.M.; Bello, I.A.; Powrie, W.; Watson, G.V.R.: SWIMS: A dynamic life cycle-based optimisation and decision support tool for solid waste management. *J. Clean. Prod.*, 2018, **196**, 547–63 DOI: 10.1016/j.jclepro.2018.05.265
- [4] Logan, M.; Visvanathan, C.: Management strategies for anaerobic digestate of organic fraction of municipal solid waste: Current status and future prospects. *Waste Manag. Res.*, 2019, **37**(1), 27–39 DOI: 10.1177/0734242X18816793
- [5] Edjabou, M.E.; Jensen, M.B.; Götze, R.; Pivnenko, K.; Petersen, C.; Scheutz, C.; Astrup, T.F.: Municipal solid waste composition: Sampling methodology, statistical analyses, and case study evaluation. *Waste Manag.*, 2015, **36**, 12–23 DOI: 10.1016/j.wasman.2014.11.009
- [6] Gustavsson, J.; Cederberg, C.: S.U.; Global Food losses and Food waste. Unep, 2011, 1. <http://www.fao.org>
- [7] *Preparatory Study on Food Waste Across EU 27*, European Commission (DG ENV); Final Report, 2011. ISBN: 978-92-79-22138-5 <https://ec.europa.eu>
- [8] Stenmarck, L.; Jensen, C.; Quedsted, T.; Moates, G.; Cseh, B.; Juul, S.; Parry, A.; Politano, A.; Redlingshofer, B.; Scherhauer, S.; Silvennoinen, K.; Soethoudt, H.; Zübert, C.; Östergren, K.: FUSIONS - Estimates of European food waste levels IVL Swedish Environmental Research Institute: Stockholm, Sweden. 2016 <https://www.eu-fusions.org>
- [9] San Martin, D.; Ramos, S.; Zuffa, J.: Valorisation of food waste to produce new raw materials for animal feed. *Food Chem.*, 2016, **198**, 68–74 DOI: 10.1016/j.foodchem.2015.11.035
- [10] García, A.J.; Esteban, M.B.; Márquez, M.C.; Ramos, P.: Biodegradable municipal solid waste: Characterization and potential use as animal feed-stuffs. *Waste Manag.*, 2005, **25**(8), 780–787. DOI: 10.1016/j.wasman.2005.01.006
- [11] Torretta, V.; Ferronato, N.; Katsoyiannis, I.A.; Tolkou, A.K.; Airolidi, M.: Novel and conventional technologies for landfill leachates treatment: A review. *Sustainability*, 2017, **9**(1), 9 DOI: 10.3390/su9010009
- [12] Kumar, A.; and Samadder, S.R.: A review on technological options of waste to energy for effective management of municipal solid waste. *Waste Manag.*, 2017, **69**, 407–422 DOI: 10.1016/j.wasman.2017.08.046
- [13] Trulli, E.; Ferronato, N.; Torretta, V.; Piscitelli, M.; Masi, S.; Mancini, I.: Sustainable mechanical biological treatment of solid waste in urbanized areas with low recycling rates. *Waste Manag.*, 2018, **71**, 556–564 DOI: 10.1016/j.wasman.2017.10.018
- [14] Hansen, W.; Christopher, M.; Verbuecheln, M.: EU Waste Policy and Challenges for Regional and Local Authorities, Background Paper for the Seminar on Household Waste Management, “Capacity Building on European Community’s Environmental Policy”, Ecological Institute for International and European Environmental Policy: Berlin, Germany, 2002. <https://www.ecologic.eu>
- [15] Khalil, A.E.E.; Arghode, V.K.; Gupta, A.K.; Lee, S.C.: Low calorific value fuelled distributed combustion with swirl for gas turbine applications. *Appl. Energy*, 2012, **98**, 69–78 DOI: 10.1016/j.apenergy.2012.02.074
- [16] Cremiato, R.; Mastellone, M.L.; Tagliaferri, C.; Zaccariello, L.; Lettieri, P.: Environmental impact of municipal solid waste management using Life Cycle Assessment: The effect of anaerobic digestion, materials recovery and secondary fuels production. *Renew. Energy*, 2018, **124**, 180–188 DOI: 10.1016/j.renene.2017.06.033
- [17] Fei, F.; Wen, Z.; Huang, S.; De Clercq, D.: Mechanical biological treatment of municipal solid waste: Energy efficiency, environmental impact and economic feasibility analysis. *J. Clean. Prod.*, 2018, **178**, 731–739 DOI: 10.1016/j.jclepro.2018.01.060
- [18] Montejo, C.; Tonini, D.; Márquez, M. del C.; Fruergaard Astrup, T.: Mechanical-biological treatment: Performance and potentials. An LCA of 8 MBT plants including waste characterization. *J. Environ. Manage.*, 2013, **128**, 661–673 DOI: 10.1016/j.jenvman.2013.05.063
- [19] Rózsenszki, T.; Koók, L.; Hutvágner, D.; Nemestóthy, N.; Bélafi-Bakó, K.; Bakonyi, P.; Kurdi, R.; Sarkady, A.: Comparison of anaerobic degradation processes for bioenergy generation from liquid fraction of pressed solid waste.

- Waste Biomass Valori.*, 2015, **6**, 465–473 DOI: [10.1007/s12649-015-9379-y](https://doi.org/10.1007/s12649-015-9379-y)
- [20] Rózsenszki, T.; Koók, L.; Bakonyi, P.; Nemestóthy, N.; Logroño, W.; Pérez, M.; Urquizo, G.; Recalde, C.; Kurdi, R.; Sarkady, A.: Municipal waste liquor treatment via bioelectrochemical and fermentation (H_2+CH_4) processes: Assessment of various technological sequences. *Chemosphere*, 2017, **171**, 692–701 DOI: [10.1016/j.chemosphere.2016.12.114](https://doi.org/10.1016/j.chemosphere.2016.12.114)
- [21] Koók, L.; Rózsenszki, T.; Nemestóthy, N.; Bélafi-Bakó, K.; Bakonyi, P.: Bioelectrochemical treatment of municipal waste liquor in microbial fuel cells for energy valorization. *J. Clean. Prod.*, 2016, **112**(5), 4406–4412 DOI: [10.1016/j.jclepro.2015.06.116](https://doi.org/10.1016/j.jclepro.2015.06.116)
- [22] Hosseini, S.E.; Wahid, M.A.: Hydrogen production from renewable and sustainable energy resources: Promising green energy carrier for clean development. *Renew. Sustain. Energy Rev.*, 2016, **57**, 850–866 DOI: [10.1016/j.rser.2015.12.112](https://doi.org/10.1016/j.rser.2015.12.112)

ELECTRIC VEHICLE MODELLING AND SIMULATION OF A LIGHT COMMERCIAL VEHICLE USING PMSM PROPULSION

AMINU BABANGIDA*¹ AND PÉTER TAMÁS SZEMES¹

¹Department of Mechatronics Engineering, University of Debrecen, Debrecen, HUNGARY

Even though the Internal Combustion Engine (ICE) used in conventional vehicles is one of the major causes of global warming and air pollution, the emission of toxic gases is also harmful to living organisms. Electric propulsion has been developed in modern electric vehicles to replace the ICE. The aim of this research is to use both the Simulink and Simscape toolboxes in MATLAB to model the dynamics of a light commercial vehicle powered by electric propulsion. This research focuses on a Volkswagen Crafter with a diesel propulsion engine manufactured in 2020. A rear-wheel driven electric powertrain based on a Permanent Magnet Synchronous Motor was designed to replace its front-wheel driven diesel engine in an urban environment at low average speeds. In this research, a Nissan Leaf battery with a nominal voltage of 360 V and a capacity of 24 kWh was modelled to serve as the energy source of the electric drivetrain. The New European Driving Cycle was used in this research to evaluate the electric propulsion. Another test input such as a speed ramp was also used to test the vehicle under different road conditions. A Proportional Integral controller was applied to control the speed of both the vehicle and synchronous motor. Different driving cycles were used to test the vehicle. The vehicle demonstrated a good tracking capability in each type of test. In addition, this research determined that the fuel economy of electric vehicles is approximately 19% better than that of conventional vehicles.

Keywords: MATLAB, New European Driving Cycle, Permanent Magnet Synchronous Motor, Proportional Integral, Volkswagen, Internal Combustion Engine

1. Introduction

Environmental effects such as air pollution and global warming which are harmful to our health are primarily caused by internal combustion engines (ICE) in conventional vehicles. “In recent decades, the research and development activities related to transportation have emphasized the development of high-efficiency, clean and safe transportation.” [1] Nowadays, electric vehicles are being developed to reduce these toxic effects and achieve safer transportation networks. In Ref. [2], Un-Noor et al. stated that the development of electric vehicles is immensely beneficial to our environment since this will lead to a reduction in the adverse effects of greenhouse gas emissions. After reviewing the literature on Electric Vehicles (EV), they drew up different design and development processes in terms of vehicle modelling, EV configurations, battery management and electrical machine drives. In EVs, ICE propulsion has been replaced by electric propulsion, consisting of electric motor drives, energy sources and other auxiliaries. Therefore, a reasonable amount of effort has been made in the field of industrial automation to make the transition from vehicles powered by traditional ICEs to those driven by EVs [3]. However, Shariff et al. [4] stated that ‘Greenhouse gas

emission and the increased cost of petroleum products are the major factors that need a shift from internal combustion engines to Electric Vehicles.’ Electric vehicles are solutions to this problem [5]. In this paper, a Volkswagen Crafter with a 2.0 diesel TDI CR engine manufactured in 2020 is examined by focusing on the replacement of its ICE with rear-wheel-driven electric motor propulsion.

According to our literature review, numerous papers have focused on electric vehicles, e.g., Wahono et al. [6] who compared three forms of range extender engines for electric cars based on simulations to overcome some disadvantages (such as the weight) of EVs over conventional vehicles driven by ICEs. A further study by Marmaras et al. [7] simulated the driver behaviour of EVs in road transport networks and electrical grids. The EV studied was modelled to investigate its integration in both the electrical grid and road transport networks. Although a multi-agent platform was used to model driver behaviour, a fleet of 1000 EVs were used as a case study where known and unknown profiles were chosen to explore the results. The cars were considered to be typical smart mechatronics systems. New trends in smart systems are summarised in Ref. [8]. Since it is difficult to formulate the exact dynamic equations of a car, Aracil et al. [9] proposed the Hardware-In-the-Loop simulation as an opti-

*Correspondence: aminubabangida24@gmail.com

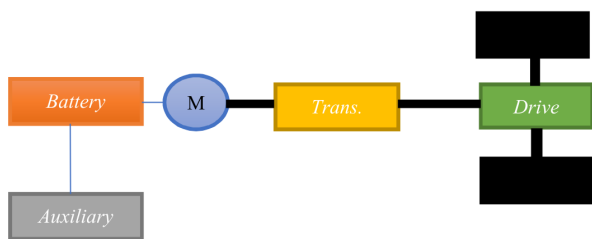


Figure 1: Battery electric vehicle

mal solution.

They discovered that electric vehicles have direct and indirect implications on road transport networks and electrical grids. Another study [10] presented a “ride comfort performance evaluation on EV conversion via simulations.” This study aimed to investigate the ride comfort of a vehicle before being converted into an electric vehicle. The study considered a full car model with 7 degrees of freedom (DOF). The two results were validated by evaluating the performance of the vehicle before and after replacing its conventional ICE with an electric motor.

2. Electric powertrain

The electric powertrain of a Battery Electric Vehicle (BEV) consists of two components, namely the electrical and mechanical parts. A schematic diagram of the general layout of the electric powertrain of a BEV is depicted in Fig. 1 where M denotes the electric motor, while the thin and thick lines represent the electrical and mechanical parts, respectively.

2.1 Electrical parts

The electrical parts consist of the battery, DC-DC converter, inverter and the controller of the electrical machine, which all depend on the electrical machine applied as the EV.

2.2 Mechanical parts

The mechanical parts of the electric powertrain consist of the transmission system, axles, wheels and chassis. In this paper, a three-phase Permanent Magnet Synchronous Motor (PMSM) was applied in a simplified energy-equivalent PMSM model that makes use of the losses resulting from the detailed PMSM model.

3. Simulation of the dynamic system of the electric powertrain

A simplified closed-loop representation of the electric powertrain applied in our electric Crafter (e-Crafter) is presented in Fig. 2, which consists of a Nissan Leaf battery as well as the PMSM drives, transmission and chassis subsystems adapted from Refs. [11] and [12], where V_{ref} denotes the speed reference and V_{ehspd} stands for the vehicle speed.

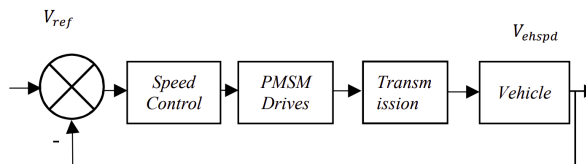


Figure 2: Simplified EV powertrain

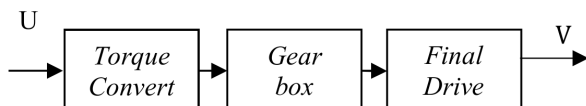


Figure 3: Transmission system [1]

3.1 Vehicle transmission system

A single-speed transmission system consists of various elements such as the gearbox, torque converter and the final drive. As is described in Ref. [1], the torque converter couples the gearbox to the vehicle and the gearbox contains the appropriate gear ratios, where U denotes the velocity required and V represents the actual velocity as a result of the final drive.

However, Fig. 3 shows a simplified single speed transmission used in modeling our electric vehicle. The presence of the torque converter in the transmission system of Fig. 3 clearly indicates that it is automatic transmission.

3.2 Vehicle modelling

Vehicle dynamics is the study of the motion of a vehicle and is comprised of three categories, that is, longitudinal, lateral and vertical dynamics. In this paper, the longitudinal dynamics of the car are modelled in a MATLAB/Simscape/Simulink environment. “In practical terms, a vehicle not only travels on a level road but also up and down the slope of a roadway as well as around corners.” [13] A simplified model and more detailed description of dynamical behaviour can be found in Ref. [8]. To model the vehicle dynamics, it is necessary to describe the forces acting on the vehicle using a Free Body Diagram as shown in Fig. 4.

The tractive force acting on the chassis can be described by [3, 14]

$$F_t = F_{ad} + F_{rr} + F_{hc} + F_A, \quad (1)$$

where F_{ad} denotes the wind resistance, which depends on the density of air ρ , surface area of the front of the vehicle A_f , drag coefficient C_d and its speed V , calculated from

$$F_{ad} = 0.5\rho C_d A_f V^2. \quad (2)$$

The rolling resistance F_{rr} depends on the weight of the vehicle w ($w = mg$), rolling resistance coefficient C_{rr} and the angle of inclination α :

$$F_{rr} = w C_{rr} \cos \alpha. \quad (3)$$

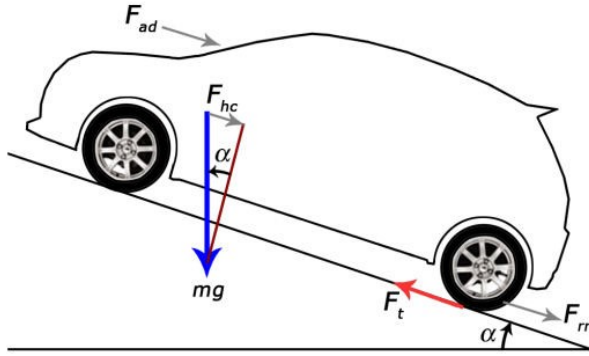


Figure 4: Vehicle dynamics [3]

Table 1: Vehicle specifications

Parameters	Specifications
Vehicle Mass	3500 kg
Centre of Gravity	0.254 m
Front Axle	1 m
Rear Axle	1.346 m
Rolling Resistance	0.013
Drag Coefficient	0.3
Air Density	1.225 kg/m ³
Gravity	9.81 m/s ²

The forces resulting from the grade resistance and resistance to acceleration are given as

$$F_{hc} = w \sin \alpha, \quad (4)$$

$$F_A = 1.04 ma, \quad (5)$$

where m denotes the mass of the vehicle in kg, 1.04 is its inertia and a stands for its acceleration. The tractive power and energy needed to propel the vehicle are given by the following equations:

$$P = FV, \quad (6)$$

$$E = Pt, \quad (7)$$

where F denotes the tractive force in newtons and t represents the time in seconds. However, the vehicle dynamics system was simulated using the parameters as specified in Table 1.

3.3 Tyre Dynamics using the Magic Formula

“The Tire-Road Interaction (Magic Formula) block models the longitudinal forces at the tire-road contact patch using the Magic Formula of Pacejka.” [25] In this paper, both the tyres attached to the front and rear axles of the vehicle were modelled using the Magic Formula. The tyre coefficients used were B, C, D and E . The values of these coefficients, adapted from Ref. [25], are shown in Table 2.

Table 2: Tyre specifications [25]

Surfaces	Constant Coefficients			
	B	C	D	E
Dry Tarmac	10	1.9	1	0.97
Wet Tarmac	12	2.3	0.82	1
Snow	5	2	0.3	1
Ice	4	2	0.1	1

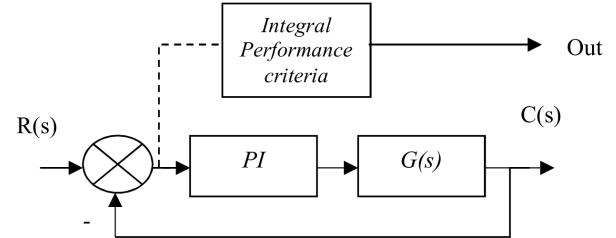


Figure 5: Control loop by applying a PI Controller

3.4 Speed controller

A PI controller was developed to control the speed of both the motor and vehicle. This PI controller was implemented in the energy-equivalent model of our PMSM. PID controllers are used in many industrial applications because of their simple structure and robustness [15]. Since noise is a measured parameter, the derivative part is not usually used [15]. The general representation of the PI controller is presented in Fig. 5.

3.5 Integral performance criteria

“Criteria based on disturbance rejection and system robustness are proposed to assess the performance of PID controllers.” [16] “A two-block structured singular value measures the robustness, and the disturbance rejection is measured by the minimum singular value of the integral gain matrix.” [16] In this paper, five criteria used in a closed-loop control system are employed to assess the performance of our PI controller. They are customarily calculated for different control setpoints such as step input and ramp input. In this research, the performance of our controller was assessed using various test inputs. “It is well-known that a well-designed control system should meet the disturbance attenuation, setpoint tracking, robust stability, and robust performance.” [16] “The first two requirements are traditionally referred to as ‘performance’ and the third, ‘robustness’ of a control system.” [16] The following are the criteria stated in Ref. [16]:

$$IAE = \int_0^{\infty} |e(t)| dt, \quad (8)$$

$$ITAE = \int_0^{\infty} t |e(t)| dt, \quad (9)$$

$$ISE = \int_0^{\infty} e^2(t) dt, \quad (10)$$

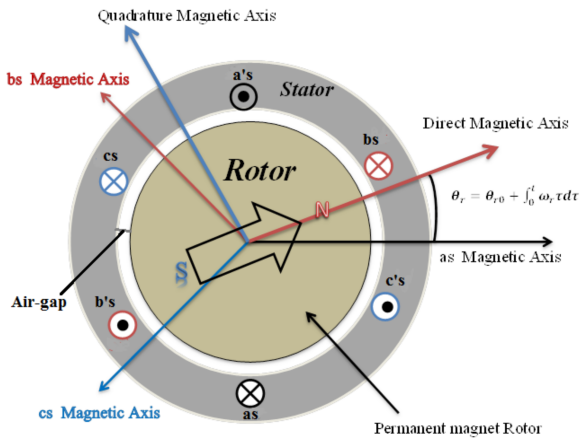


Figure 6: Structure of the PMSM [17]

$$\text{ITSE} = \int_0^{\infty} te^2(t) dt, \quad (11)$$

where IAE stands for the Integral Absolute Error, ITAE the Integral Time Absolute Error, ISE the Integral Square Error, and ITSE the Integral time Squared Absolute Error [16]. These performance indexes were used to tune our PID controller.

4. Permanent magnet synchronous motor

A PMSM, which is widely used to overcome the disadvantages of a Brushless DC Motor (BLDC) [17], is proposed in this research. Virani et al. employed the Field-Oriented Control (FOC) approach to control the speed and torque of the PMSM of an electric car [17]. Moreover, Espina et al. in their review of Speed Anti-Windup PI strategies for Field-Oriented Control of Permanent Magnet Synchronous Motors emphasized that PMSMs are gaining popularity when compared to other AC Motors due to their higher efficiency, lower inertia as well as reduction in weight and volume [18].

This study suggests PMSM has advantages in EV applications over other types of electric motors. The general structure of the PMSM motor is presented as shown in Fig. 6. The rotor having a permanent magnet mounted on it creates a rotating magnetic field, which in turn produces a sinusoidal electromagnetic field.

4.1 PMSM Mathematical Model

The modelling of a PMSM was carried out based on the following assumptions [17, 26]:

1. There is distribution of the sinusoidal Magnetomotive Force (MMF) in the air gap.
2. Restriction in the saliency according to the rotor position.
3. Ignoring the hysteresis and saturation.
4. Assuming a balanced 3-phase supply voltage.

5. Assuming that the back EMF (electromotive force) is sinusoidal.

The 3-phase supply voltage is given by [17]

$$V_A = P\Psi_A + I_A R_S, \quad (12)$$

$$V_B = P\Psi_B + I_B R_S, \quad (13)$$

$$V_C = P\Psi_C + I_C R_S, \quad (14)$$

where I_A , I_B and I_C denote the phase currents, V_A , V_B , and V_C represent the phase voltages, Ψ_A , Ψ_B and Ψ_C stand for the flux linkages, and R_S and P are the phase resistance and "derivative operator," respectively [17].

However, using the reference frame d_q , the model of the PMSM can be represented in the rotating reference frame d_q as

$$V_q = R_S I_q + \omega_r \lambda_d + P \lambda_p, \quad (15)$$

$$V_d = R_S I_d - \omega_r \lambda_p + P \lambda_q, \quad (16)$$

$$\lambda_q = L_q I_q \quad \text{and} \quad \lambda_d = L_d I_d + \lambda_r, \quad (17)$$

$$V_q = R_S I_q + \omega_r (L_d I_d + \lambda_r) + P L_q I_q, \quad (18)$$

$$V_d = R_S I_d - \omega_r L_q I_q + P (L_d I_d + \lambda_r), \quad (19)$$

Therefore, the torque developed by the PMSM is given by

$$T_e = \frac{3P}{2} (\Psi_r I_q + (L_d - L_q) I_d I_q), \quad (20)$$

where P denotes the number of poles of the machine [17]; the electric torque derived in Eq. 20 is divided into two components, namely the "mutual reactance torque" [17] and "reluctance torque", the latter results from the difference in reluctance between the q - and d -axes [17].

However, for the PMSM, when $L_q = L_d = L_S$, the torque generated by the PMSM is [17]

$$T_e = \frac{3P}{2} (\Psi_r I_q). \quad (21)$$

The three-phase voltages of the detailed PMSM model are presented in Fig. 7. Since it can be seen that the simulation runs with a stop time of 0.2 s, which is very slow, it runs more slowly than in real time. To resolve this issue, a methodology was adapted using this detailed model of the PMSM to obtain the electrical losses of an energy-equivalent model.

The corresponding 3-phase currents obtained by simulating the detailed three-phase PMSM are shown in Fig. 8. In this model, the torque induced by the structure of the chassis is not included in the modelling process, namely the cogging torque [19]. Flux harmonics are also present since the magnet in the PMSM is composed of "neodymium, iron and boron". [19] Therefore, its magnetic flux density is usually affected by variations in temperature. [19]

Similarly, there parametric uncertainties are present due to mechanical and electrical parameters. In terms

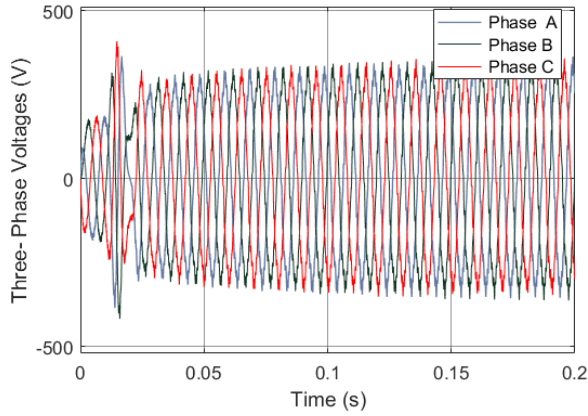


Figure 7: Three-phase voltages

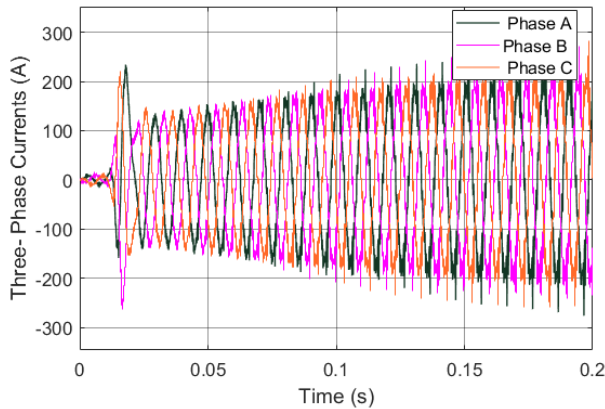


Figure 8: Three-phase currents

of mechanical ones, the inertia of the PMSM is uncertain due to its changing behaviour under different operating conditions. Regarding electrical ones, the stator resistance, which is a function of the temperature, influences the control of the current loop performance [19].

The electrical losses resulting from the simulation of the PMSM are presented in Table 3. These losses were obtained by using the corresponding torque and speed vectors, moreover, this method was adopted from Ref. [11].

4.2 Simplified PMSM model

In this paper, a three-phase model of the PMSM designed was converted into an equivalent energy model based

Table 3: PMSM electrical losses

Speed [rpm]	Torque [Nm]	experimental electrical losses (kW)				
99	9	0.0811	0.321	0.943	2.146	4.379
454	45	0.0621	0.299	0.925	2.191	4.567
803	80	0.0454	0.281	0.9	2.217	4.796
1149	114	0.0298	0.262	0.858	2.217	4.950
1499	149	0.016	0.251	0.873	2.23	4.998

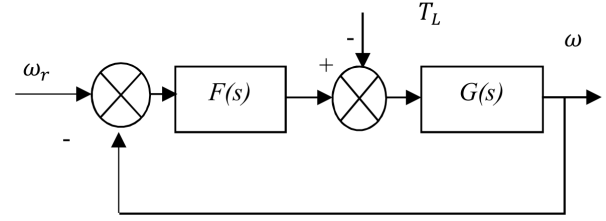


Figure 9: PMSM equivalent energy model

Table 4: Motor specifications

Parameters	Specifications
Maximum Power	80 kW
Maximum Torque	280 Nm
Time Constant	0.02 s
Series Resistance	0
Rotor Inertia	3.9×10^{-4} kg m ²
Rotor Damping	10^{-5} Nm/(rad/s)

on the electrical losses obtained from the detailed three-phase model of the PMSM. The motor parameters used during the simulation are presented in Table 4.

From Fig. 9, the transfer function from T_L to ω is given by

$$G(s) = \frac{1}{sJ + B}, \quad (22)$$

$$H(s) = \frac{\omega}{\omega_r} = \frac{F(s)G(s)}{1 + F(s)G(s)} = \frac{\alpha/s}{1 + \alpha/s}, \quad (23)$$

where T_L denotes the load torque, ω represents the achieved speed, ω_r refers to the reference speed, J stands for the total of the moments of inertia, B is the coefficient of viscosity and α denotes the bandwidth of the speed control [20]

$$F(s) = \frac{\alpha}{s} \left(\frac{1}{sJ + B} \right). \quad (24)$$

Transforming Eq. 3 into the PI form [14] yields

$$F(s) = \alpha J + \frac{\alpha B}{s} = K_p + \frac{K_i}{s}. \quad (25)$$

Therefore, in the case of the simplified equivalent PMSM Model, only the outer loop was analysed, which uses a PI controller to control the speed of the motor. Generally, a three-phase PMSM, using the FOC (Field-Oriented Control) strategy, consists of two control loops with two PIs in the inner loop to control the current vectors.

The PI controller can be mathematically represented as

$$u(t) = k_p e(t) + k_i \int e(t) dt, \quad (26)$$

where k_p and k_i denote the proportional and integral coefficients, respectively and $e(t)$ represents the error between the reference and the feedback signal [21].

Table 5: Battery parameters [13]

Chemistry	Symbol	Cell Voltage (V)	Specific Energy (Wh/kg)	Cycle Life	Specific Power (W/kg)	Self-Discharge (per month)
Lead-Acid	PbA	2	35	≈ 500	250 – 500	5
Nickel-metal hydride	NiMH	1.2	30 – 100	> 1000	200 – 600	> 10
Lithium-ion	Li-ion	3.8	80 – 160	> 1000	250 – 600	< 2
Lithium-titanate	LTO	2.5	50 – 100	$> 20,000$	N/A	N/A
Alkaline	ZnMnO ₂	1.5	110	N/A	N/A	< 0.3

Table 6: Battery specifications

Parameters	Specifications
Battery Nominal Voltage	360 V
Battery Capacity	24 kWh
Battery Charge	66.2 Ah
Energy Density	140 Wh/kg
Power Density	2.5 kW/kg
Battery Power	90 kW

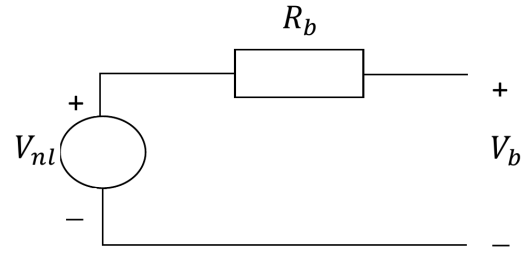


Figure 10: Battery equivalent circuit model

5. Nissan Leaf Battery

In this research, a Nissan Leaf Battery manufactured in 2011 was used to design the electric vehicle. The battery has a nominal voltage of 360 V and a capacity of 24 kWh [13]. It consists of 48 modules and 4 cells (2 in parallel, 2 in series), amounting to 192 cells [14]. The total voltage of the battery pack is approximately 403.2 V. The possible arrangement of the cells in a battery pack has been studied in general by Emadi [22].

Table 5 shows the batteries available along with their chemistries. In this paper, a lithium-ion battery was used. The specific energy defines the energy stored in the battery per unit of weight. The cell voltage is 4.2 V when fully charged and 2.5 V when discharged.

While the battery specifications for a Nissan Leaf manufactured in 2011 are detailed in Table 6, this paper used a model of a built-in battery simulated using Simulink based on these specifications to simulate our traction battery.

5.1 Battery modelling

Generally, our battery was analysed using an equivalent circuit model from the literature to study its behaviour mathematically. This equivalent circuit was modelled based on a Nissan Leaf to carry out the analysis before being compared with the built-in battery simulated using MATLAB. The cell voltage of the battery as studied in Ref. [23] is given by

$$V_b = V_r^0 - \frac{RT}{nF} \ln Q_R, \quad (27)$$

where R denotes the ideal gas constant, T represents the temperature and Q_R stands for the reaction quotient, which is a function of the concentrations of the reactants.

However, since each battery is associated with an ohmic drop [23], the equation can be modified as

$$V_b = V_r^0 - \frac{RT}{nF} \ln Q_R - R_b I_b. \quad (28)$$

The above equation can then be modified to include the battery capacity as

$$V_b(I_b, y) = V_r^0 - A \ln(By) - Ky - Fe^{G(y-y_3)} - R_b I_b, \quad (29)$$

where y denotes a variable that can be related to the capacity, DoD (depth of discharge), SoC (state of charge) or the cell energy, y_3 represents the value at which the exponential decay begins, and A , B , K , F and G stand for values determined by curve fitting [23]. The above equation can be expressed in terms of the DoD as

$$V_b(I_b, \text{DoD}) = V_r^0 - A \ln(B \text{DoD}) - K \text{DoD} - Fe^{G(\text{DoD}-\text{DoD}_3)} - R_b I_b \quad (30)$$

In terms of the no-load, the ohmic drop can be expressed as

$$V_{b(nl)}(\text{DoD}) = V_r^0 - A \ln(B \text{DoD}) - Fe^{G(\text{DoD}-\text{DoD}_3)}. \quad (31)$$

The aforementioned equations can be modelled to represent the equivalent circuit shown in Fig. 10.

Therefore, the above mathematical model of the battery can be represented by the simplified battery model presented in Fig. 10 based on the already built-in Simulink model.

5.2 Battery parameters

The design considerations of a battery ensure it functions safely and reliably. Therefore, the battery management

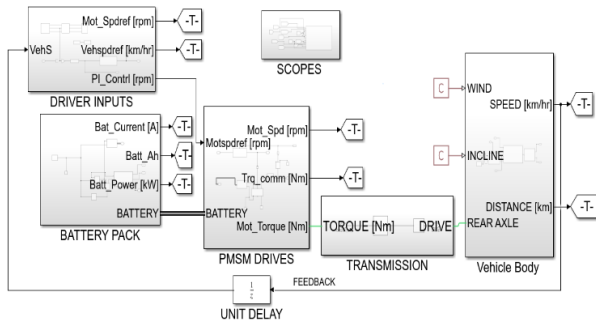


Figure 11: Simulink model of the EV

system takes into account three parameters, namely the total voltage of the battery pack, the total temperature of an individual cell in the pack and the total current, before calculating the State of Charge (SoC), State of Health (SoH), Safe Operating Envelope (SOE) and faults. The SoC, which is expressed as a percentage, determines the amount of voltage also as a percentage. In this paper, the SoC was found to be 99%, that is, almost fully charged. A friction brake was used to stop our vehicle. The battery was naturally recharged due to regenerative braking. The SoH represents the battery's capacity relative to its capacity when initially installed. Finally, the SOE shows the amount of current that can be charged or discharged at any given time.

6. Matlab model

The complete model of our electric vehicle simulated in a Simulink environment is depicted in Fig. 11. The model consists of the Nissan Leaf battery, the PMSM drives, the transmission systems and the vehicle subsystems.

7. Results

The "New European Driving Cycle (NEDC)" used in this research to test our vehicle and other driving cycles to comply with energy consumption and emissions reduction targets is presented in Fig. 12. In this paper, only three cycles of 200 seconds in duration were used in the "NEDC." Other driving cycles such as the "Urban Dynamometer Driving Schedule (UDDS)," were used to test our electric vehicle.

The NEDC, adopted from the literature, is mainly used to determine the consumption of electric vehicles, gas emissions, etc. The reference speed and the speed achieved by the vehicle over 200 seconds are both represented in Fig. 13. The power consumption of the battery in kilowatts is shown in Fig. 14. The Nissan Leaf can provide over 90 kW of power, 50 kW of which was consumed by our electric vehicle. The energy consumption of the battery in kWh is presented in Fig. 15.

Given that the SoC achieved by our battery was 99%, i.e., it was almost fully charged, the operating temperature used by our Battery Management System was ne-

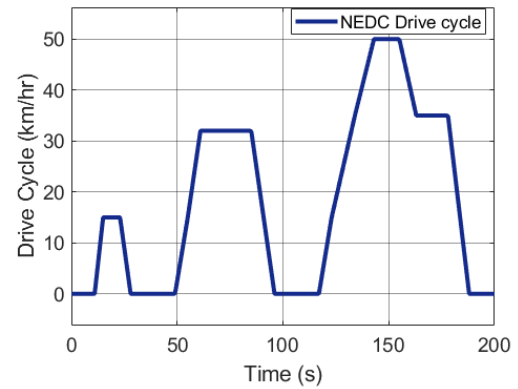


Figure 12: NEDC driving cycle

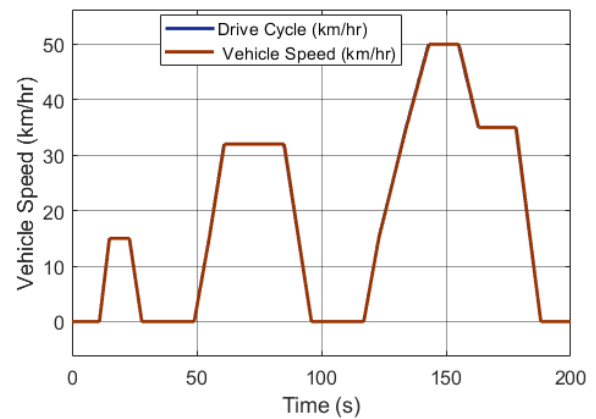


Figure 13: Speed achieved by the vehicle

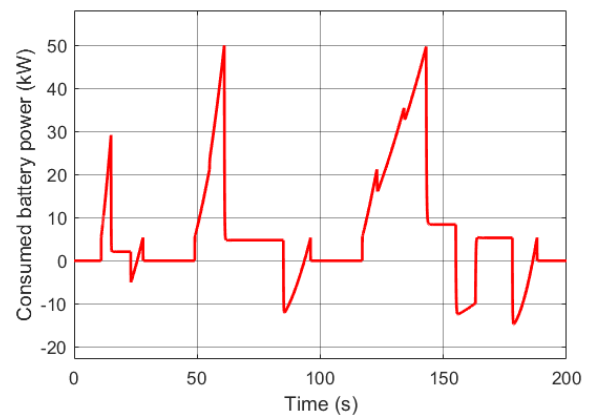


Figure 14: Power consumption of the battery

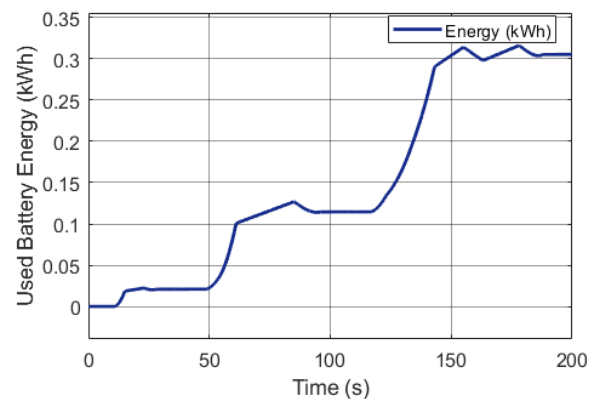


Figure 15: Energy consumption of the battery

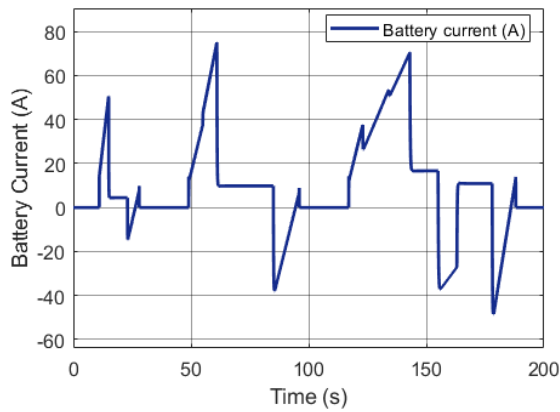


Figure 16: Battery current

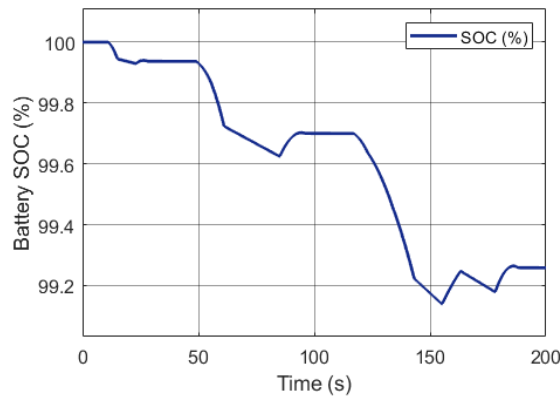


Figure 17: Battery SoC

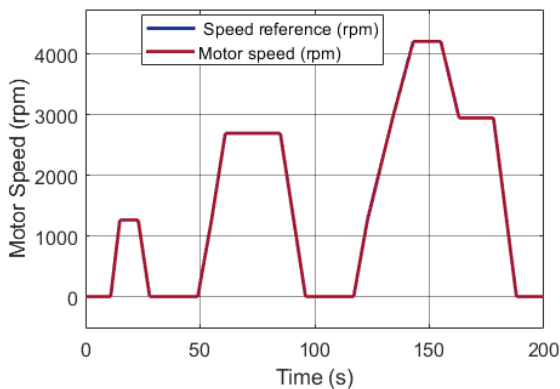


Figure 18: Achieved motor speed

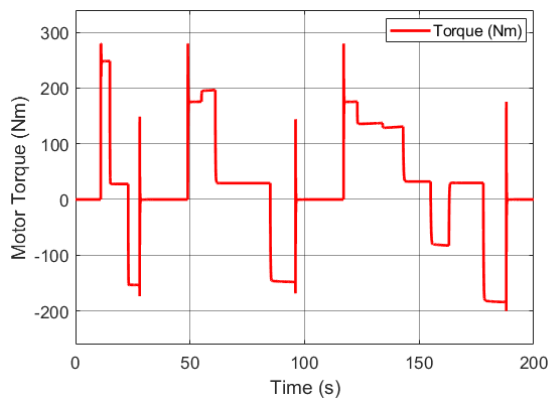


Figure 19: Motor torque

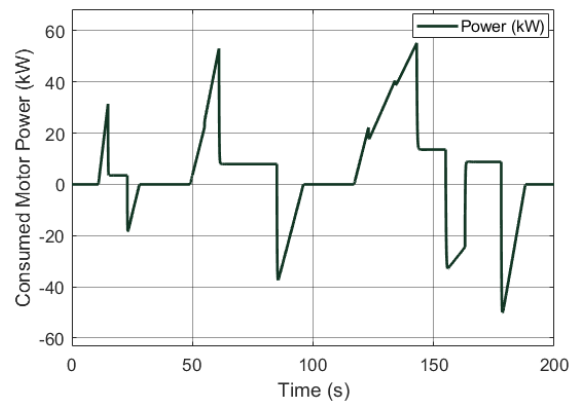


Figure 20: Power consumption of the motor

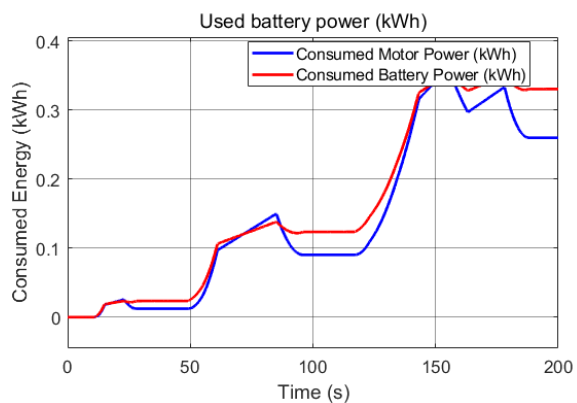


Figure 21: Energy consumption of the motor and battery

glected. In a future study, a complete Battery Management System will be implemented to determine and ensure safe operating conditions for our battery system.

The battery current is represented in Fig. 16. The battery draws a maximum current of 75 A when the vehicle is accelerating and a minimum current of -55 A when decelerating. The SoC of the battery as a percentage, which is approximately maintained at 99% due to natural regenerative braking, is presented in Fig. 17:

The reference speed of the motor was 4250 rpm, which accurately tracks the actual rate, and is shown in Fig. 18. The maximum torque of 280 Nm, as seen in Table 4 of the motor specifications, is shown in Fig. 19, while the power consumption of the motor, which is approximately 49 kW, is presented in Fig. 20. The losses can be analysed in terms of the energy transmitted from the storage system, namely from the battery to the wheels of the vehicle. The energy consumption of both the battery and motor are plotted in Fig. 21.

The difference between the plots in Fig. 21 is the energy lost when transmitting from the energy supply system, that is, from the battery to our PMSM. It can be seen that: if $E_b = 0.3305$ kWh is the energy consumed by our Nissan Leaf battery and $E_m = 0.2599$ kWh is the energy consumed by our PMSM, then the energy efficiency, $\eta = E_m/E_b = 78.63\%$.

Therefore, our electric vehicle is approximately 19%

Table 7: PI controller parameters

Gains		Performance Indices			
K_p	K_i	IAE	ISE	ITAE	ITSE
60	60	4.1141×10^{-6}	1.0935×10^{-12}	2.8676×10^{-5}	5.1996×10^{-12}
60	40	1.353×10^{-4}	1.0372×10^{-9}	0.0011	6.3622×10^{-9}
5	20	7.9202×10^{-10}	3.1365×10^{-20}	7.9202×10^{-9}	3.1363×10^{-19}

more efficient than conventional vehicles. However, Du et al. determined that an EV can be up to approximately 15% more efficient than conventional vehicles driven by ICEs in terms of fuel consumption (fuel economy) [24]. The speed of the vehicle when tested by a ramp input is depicted in Fig. 22. In this case, the vehicle accelerates from rest to a final speed of 5.55 m/s (20 km/hr).

The PMSM implemented as a result of a ramp test signal is presented in Fig. 23 below. The consumption of vehicles was less during this test to prove the performance of our motor and electric vehicle under these ideal conditions.

7.1 Settings of the PI controller based on the performance matrix

The settings of the PI controller based on the performance matrix obtained by conducting several experiments until optimized gains had been achieved is presented in Table

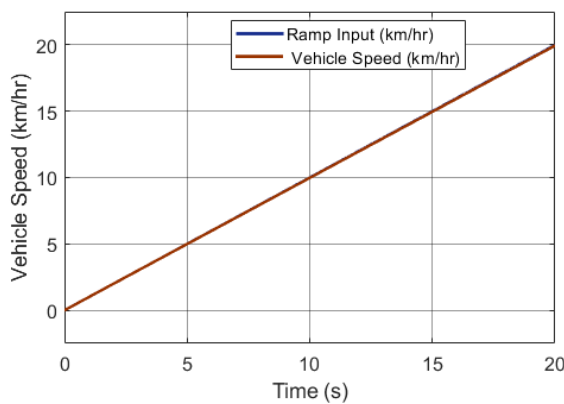


Figure 22: Speed of the vehicle due to a ramp input

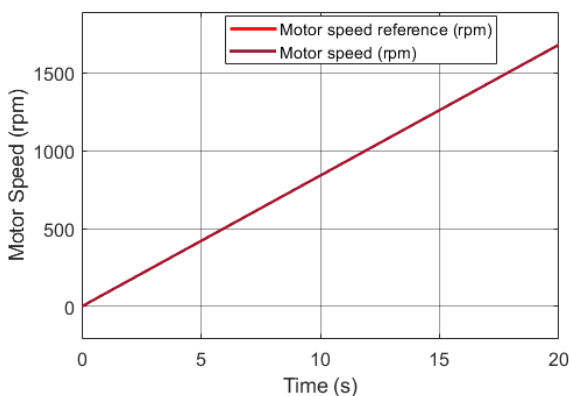


Figure 23: Speed of the motor due to a ramp input

7. It can be seen from this table that minimum values of these performance indices were required to obtain these optimal gains. Moreover, the system is stable and the controller somewhat reliable. However, a future study may propose intelligent tuning techniques to achieve a realistic level of performance by accurately taking into consideration the model uncertainties and parameter variations due to operating conditions, e.g., temperature and humidity amongst other considerable factors.

8. Conclusions

The modelling and simulation of an electric powertrain based on the PMSM Motor of a light commercial vehicle, a VW Crafter manufactured in 2020, has been presented. A PI-based classical control algorithm of the outer control loop of the PMSM was used to control the speed of the vehicle and motor.

PMSM-based electrical-rear-wheel-driven traction of a VW Crafter manufactured in 2020 was modelled. This motor was chosen due to its high degree of efficiency over other electrical traction machines. This motor propelled the vehicle during its motoring action and while recharging the battery when acting as a generator.

A Nissan Leaf battery with a rating of 360 V manufactured in 2011 and an energy supply to the system of 24 kWh was used. The battery was used to supply energy to propel the vehicle. This research determined that the fuel consumption decreased by a significant percentage by replacing conventional vehicles driven by ICEs with electric vehicles.

Acknowledgments

This research work is supported by TKP2020-NKA-04. Project no. TKP2020-NKA-04 has been implemented with the support provided from the National Research, Development and Innovation Fund of Hungary, financed under the 2020-4.1.1-TKP2020 funding scheme.

REFERENCES

- [1] Ehsani, M.; Gao, Y.; Longo, S.; Ebrahimi, K.M.: Modern Electric, Hybrid Electric, and Fuel Cell Vehicles, Third ed. (CRC Press) 2018 DOI: [10.1201/9780429504884](https://doi.org/10.1201/9780429504884)
- [2] Un-Noor, F.; Padmanaban, S.; Mihet-Popa, L.; Mollah M. N.; Hossain, E.: A comprehensive study of key electric vehicle (EV) components, technologies, challenges, impacts, and future direction

- of development, *Energies*, 2017, **10**(8), 1–82 DOI: [10.3390/en10081217](https://doi.org/10.3390/en10081217)
- [3] Mohd, T. A. T.; Hassan, M. K.; Aziz, WMK. A.: Mathematical modeling and simulation of an electric vehicle, *J. Mech. Eng. & Sci.*, 2015, **8**, 1312–1321, DOI: [10.15282/jmes.8.2015.6.0128](https://doi.org/10.15282/jmes.8.2015.6.0128)
- [4] Shariff, S. M.; Iqbal, D.; Saad Alam, M.; Ahmad, F.: A state of the art review of electric vehicle to grid (V2G) technology, *IOP Conference Series: Materials Science and Engineering*, 2019, **561**(1), 012103 DOI: [10.1088/1757-899X/561/1/012103](https://doi.org/10.1088/1757-899X/561/1/012103)
- [5] Cioroianu, C. C.; Marinescu, D. G.; Iorga, A.; Sibiceanu, A. R.: Simulation of an electric vehicle model on the new WLTC test cycle using AVL CRUISE software *IOP Conference Series: Materials Science and Engineering*, 2017, **252**(1), 012060 DOI: [10.1088/1757-899X/252/1/012060](https://doi.org/10.1088/1757-899X/252/1/012060)
- [6] Wahono, B.; Nur, A.; Santoso, W. B.; Praptijanto, A.: A comparison study of range-extended engines for electric vehicle based on vehicle simulator, *J. Mech. Eng. Sci.*, 2016, **10**(1), 1803–1816 DOI: [10.15282/jmes.10.1.2016.5.0173](https://doi.org/10.15282/jmes.10.1.2016.5.0173)
- [7] Marmaras, C.; Xydias, E.; Cipcigan, L.: Simulation of electric vehicle driver behavior in road transport and electric power networks, *Transp. Res. Part C Emerg. Technol.*, 2017, **80**, 239–256 DOI: [10.1016/j.trc.2017.05.004](https://doi.org/10.1016/j.trc.2017.05.004)
- [8] Fodor, D.; Enisz, K.: Vehicle dynamics based ABS ECU verification on real-time hardware-in-the-loop simulator *International Power Electronics and Motion Control Conference and Exposition*, 2014, 1247–1251 DOI: [10.1109/EPEPEMC.2014.6980683](https://doi.org/10.1109/EPEPEMC.2014.6980683)
- [9] Aracil, C.; Sziebig, G.; Korondi, P.; Oh, S.; Tan, Z.; Ruderman, M.; He, W.; Ding, L.; Luo, H.; Yin, S.: Toward smart systems: Their sensing and control in industrial electronics and applications, *IEEE Industrial Electronics Magazine*, 2021, **15**(1), 104–114 DOI: [10.1109/MIE.2020.3042171](https://doi.org/10.1109/MIE.2020.3042171)
- [10] Abu Bakar, S. A.; Muhamad Said, M. F.; Aziz, A. A.: Ride comfort performance evaluations on electric vehicle conversion via simulations, *ARPJ J. Eng. Appl. Sci.*, 2015, **10**(17), 7794–7798 <http://www.arpnjournals.com/jeas>
- [11] Ito, I.: Battery Electric Vehicle Model in Simscape, 2021 <https://github.com>
- [12] MathWorks Student Competitions Team (2020). Student Competitions - Physical Modeling Trainingm, MATLAB Central File Exchange, 2020 <https://www.mathworks.com>
- [13] Yang, S.; Lu, Y.; Li, S.: An overview on vehicle dynamics, *Int. J. Dyn. Control*, 2013, **1**, 385–395 DOI: [10.1007/s40435-013-0032-y](https://doi.org/10.1007/s40435-013-0032-y)
- [14] Saleem, A.; Liu, N.; Junjie, H.; Iqbal, A.; Hayyat, M. A.; Mateen, M.: Modelling of an electric vehicle for tractive force calculation along with factors affecting the total tractive power and energy demand, *2020 3rd International Conference on Computing, Mathematics and Engineering Technologies (iCoMET)*, 2020, 1–5 DOI: [10.1109/iCoMET48670.2020.9073845](https://doi.org/10.1109/iCoMET48670.2020.9073845)
- [15] Dogruer, T.; Tan, N.: Design of PI controller, using optimization method in fractional order control systems, *IFAC-PapersOnLine*, 2018, **51**(4), 841–846 DOI: [10.1016/j.ifacol.2018.06.124](https://doi.org/10.1016/j.ifacol.2018.06.124)
- [16] Tan, W.; Marquez, H. J.; Chen, T.: Performance assessment of PID controllers, *Control Intell. Syst.*, 2004, **32**(3), 158–166 DOI: [10.2316/journal.201.2004.3.201-1309](https://doi.org/10.2316/journal.201.2004.3.201-1309)
- [17] Virani, V.; Arya, S.; Baria, J.: Modelling and control of PMSM drive-by field oriented control for HEV, *Advances in Power Generation from Renewable Energy Sources (APGRES)*, 2019, 1–11 DOI: [10.2139/ssrn.3442515](https://doi.org/10.2139/ssrn.3442515)
- [18] Espina, J.; Arias, A.; Balcells, J.; Ortega, C.: Speed anti-windup PI strategies review for field-oriented control of permanent magnet synchronous machines, *Compatibility and Power Electronics*, 2009, 279–285 DOI: [10.1109/CPE.2009.5156047](https://doi.org/10.1109/CPE.2009.5156047)
- [19] Yang, J.; Chen, W. H.; Li, S.; Guo, L.; Yan, Y.: Disturbance/uncertainty estimation and attenuation techniques in PMSM drives - A survey, *IEEE Trans. Ind. Electron.*, 2017, **64**(4), 3273–3285 DOI: [10.1109/TIE.2016.2583412](https://doi.org/10.1109/TIE.2016.2583412)
- [20] Han, W.: Simulation model development of electric motor and controller, Master's thesis, Chalmers University of Technology, Gothenburg, Sweden, 2017 <https://publications.lib.chalmers.se>
- [21] Lina, W.; Kun, X.; De Lillo, L.; Empringham, L.; Wheeler, P.: PI controller relay auto-tuning using delay and phase margin in PMSM drives, *Chinese J. Aeronaut.*, 2014, **27**(6), 1527–1537, DOI: [10.1016/j.cja.2014.10.019](https://doi.org/10.1016/j.cja.2014.10.019)
- [22] Emadi, A.: *Advanced electric drive vehicles*, (CRC Press, Taylor & Francis Group, London–New York), 2015 ISBN: 978-1-4665-9770-9
- [23] Al azze, Q.: Field-oriented control of permanent magnet synchronous motors based on DSP controller, Master's thesis, Southern Illinois University, Edwardsville, USA, 2014
- [24] Du, G.; Cao, W.; Hu, S.; Lin, Z.; Yuan, T.: Design and assessment of an electric vehicle powertrain model based on real-world driving and charging cycles, *IEEE Trans. Vehicular Tech.*, 2019, **68**(2), 1178–1187 DOI: [10.1109/TVT.2018.2884812](https://doi.org/10.1109/TVT.2018.2884812)
- [25] Pacejka, H.: *Tire and vehicle dynamics*, (Butterworth-Heinemann, Elsevier Ltd., Oxford, UK), 2005 ISBN: 978-0-0809-7017-2
- [26] Szalay, I.; Fodor, D.; Kohlrusz, G.: Modeling of slotless surface-mounted PM synchronous motor for sensorless applications, *2014 IEEE International Electric Vehicle Conference (IEVC)*, 2014, 1–5 DOI: [10.1109/IEVC.2014.7056198](https://doi.org/10.1109/IEVC.2014.7056198)

DEVELOPMENT OF COMPARTMENT MODELS FOR DIAGNOSTIC PURPOSES

BÁLINT LEVENTE TARCSAY^{*1}, ÁGNES BÁRKÁNYI¹, TIBOR CHOVÁN¹, AND SÁNDOR NÉMETH¹

¹Research Centre for Biochemical, Environmental and Chemical Engineering, University of Pannonia, Egyetem u. 10, Veszprém, 8200, HUNGARY

The importance of recognizing the presence of process faults and resolving these faults is continuously increasing parallel to the development of industrial processes. Fault detection methods which are both robust and sensitive help to recognize the presence of faults in time to avoid malfunctions, financial loss, environmental damage or loss of human life. In the literature, the use of various model-based fault detection methods has gained a considerable degree of popularity. Methods usually based on black-box models, data-based techniques or models using symbolic logic, e.g. expert systems, have become widespread. White-box models, on the other hand, have been applied less despite their considerable robustness because of multiple reasons. Firstly, their complexity and the relatively vast amount of technological and modelling knowledge needed to construct them for industrial systems. Secondly, their large computational demand which makes them less suitable for online fault detection. In this study, the aim was to resolve these problems by developing a method to simplify the complex Computational Fluid Dynamics models employed to describe the equipment used in the chemical industry into less complex model structures. These simpler structures are Compartment Models, a type of white-box model which breaks down a complex system into smaller units with idealized behaviour. In the case of a small number of compartments, the computational load of such models is not significant, therefore, they can be employed for the purposes of online fault detection while providing an accurate representation of the system. For the purpose of identifying the compartmental structure, fuzzy logic was employed to create a model which approximates the real behaviour of the system as accurately as possible. Our future objective is to explore the possibility of combining this model with various diagnostic methods (expert systems, Bayesian networks, parity relations, etc.) and derive robust tools for the purpose of fault detection.

Keywords: Compartment Model, Computational Fluid Dynamics, expert system, fuzzy logic

1. Introduction

Fault detection and isolation has become a cardinal problem in industrial practices. As the intricacy of technological processes increases, the probability of faults arising also grows. However, due to the stricter demands for environmentally friendly and profitable technologies, the presence of faults which could potentially cause financial loss, environmental hazards or loss of life cannot be tolerated. Faults such as those defined by Venkatasubramanian et al. [1] describe the consequences when an observed process variable deviates from its expected value. The source of such process faults is known as a root cause. Naturally, if left unmanaged, faults can propagate and lead to serious disasters, e.g., the Bhopal disaster or the Texas City Refinery explosion [2, 3]. To circumvent such occurrences, modern knowledge-based fault detection techniques have become commonplace.

These methods use the same common principle for fault detection. Firstly, some knowledge is used to cre-

ate a model of the system under normal operating conditions. Then the actual operation of the system is observed and, if the behaviour of the system does not match the assumptions drawn from the model, then an abnormality is present [4]. After identifying the presence of an abnormality, various approaches using different techniques trace the fault signature back to the root cause depending on the type of knowledge used to create the system model. Therefore, it is possible to differentiate between knowledge that originates from quantitative as well as qualitative models and that from relations based on process history [1, 5, 6].

The aforementioned categorization of knowledge used for fault detection methods stems from the early works of Venkatasubramanian [1] and is arbitrary. The expectations of fault detection and isolation methods are that they should be robust, sensitive and accurate. Robust, in this sense, means that the method should work reliably, even in the presence of noise, disturbances and changes in operating conditions. Sensitive and accurate means that the method should even be able to recognize small pro-

^{*}Correspondence: tarcsayb@fmt.uni-pannon.hu

cess faults and reliably identify their root causes. Usually, the bigger issue with most fault detection methods is their robustness. Commonly used models for the purposes of fault detection, e.g., a posteriori models, neural networks and statistical methods, all employ arbitrary relationships between system variables which only hold true in a certain operating regime [4].

If the system itself or the operating point changes, these models often become unreliable. Therefore, they lack both robustness and flexibility. Among quantitative models used for fault detection, another type of model, the a priori or white-box model, is listed. This modelling technique uses the laws of physics, chemistry or any applicable scientific discipline to describe the behaviour of various systems. Since the laws of nature cannot be violated, these models are incredibly robust and hold true for a system regardless of its operating point.

The problem is that these models are complex and difficult to create for industrial systems since they require a vast amount of technological and modelling knowledge. Additionally, they often require a significant computational load to be solved that renders them impractical for the purposes of online fault detection [1]. This is why they have not garnered widespread use in the field of diagnostic procedures.

Over the course of this work, our goal was to propose a method for simplifying the complex Computational Fluid Dynamics (CFD) of white-box modelling techniques to describe the behaviour of units used in the chemical industry. CFD methods have become widespread over the last few decades for the purpose of solving the material and energy balance equations of complex systems to describe transport phenomena as well as evaluate flow patterns, velocity fields and mixing in fluid systems. These numerical methods involve the discretization of the differential equations that describe the behaviour of the unit as well as solving them through direct or iterative computation methods [7].

An alternative to these methods is the use of Compartment Models (CM). CMs emulate the behaviour of complex systems by identifying individual elements of the system that can be approximated using idealized models [8]. In the case of chemical technologies, the flow and transport phenomena in a system can be approximated by breaking down the system into compartments that exhibit idealized flow behaviour. CMs have become widespread in pharmacokinetic experiments to simulate drug transport in biological systems as well as during the evaluation and modelling of bioreactors and chemical systems. Savic et al. [9] used a transit CM in pharmacokinetic studies involving the absorption of four different substances. They compared the results to those of a lag time model and concluded that the proposed CM produced a significantly better match to the observed experimental data and can be used as an alternative to the lag time model. Pigou and Morchain [10] employed a CM combined with a population balance model and metabolic model to estimate the behaviour of a microbial population within industrial

bioreactors. Their approach was validated by applying it to a bioreactor containing the *Escherichia coli* species using experimental data. Spann et al. [11] created a risk assessment methodology for the cultivation of lactic acid bacteria based on a CM. They combined a CM with a biochemical model to monitor the species *Streptococcus thermophilus* online. Using Monte Carlo methods, they evaluated the risk of the biomass size not achieving its desired extent under the operating conditions of the system with regard to uncertainties in the production process. Kaur et al. [12] developed a model for the simulation of a top spray fluidized bed granulator. In their work, they defined two compartments within the system, a “wet” compartment in which aggregation of the particles is dominant and a “dry” compartment in which the breaking up of the particles is mainly observed. By combining the flow model with a population balance model, they managed to observe the effects of operational parameters on the particle size distribution of the granulated product.

The examples show that the CM is a contemporary and popular approach to system modelling. The main question, however, when developing a CM is how to select the appropriate number and characteristics of as well as connections between compartments to obtain a model that accurately represents the flow patterns of the real system. The CM usually employs two types of idealized compartments to approximate a velocity field in a system. These are compartments which are assumed to be perfectly stirred and homogeneous (Continuous Stirred Tank Reactor (CSTR) model) or compartments exhibiting turbulent plug flow (Plug Flow Reactor (PFR) model). These compartments are linked through mixer (M) and distributor (D) models [13]. These latter units are usually only of mathematical significance and their volume is assumed to be zero. The component balance model for the units is showcased in the following equations.

For unit CSTR:

$$\frac{dc_{\text{CSTR}}(t)}{dt} = \frac{F_{\text{in}}}{V_{\text{CSTR}}} (c_{\text{in}}(t) - c_{\text{CSTR}}(t)) \quad (1)$$

$$F_{\text{CSTR}} = F_{\text{in}} \quad (2)$$

For unit PFR:

$$\frac{\partial c_{\text{PFR}}(t, x)}{\partial t} = -v_{\text{PFR}} \frac{\partial c_{\text{PFR}}(t, x)}{\partial x} \quad (3)$$

$$F_{\text{PFR}} = F_{\text{in}} \quad (4)$$

For unit M:

$$c_{\text{M}} = \frac{\sum_{i=1}^{n_{\text{in}}} c_{\text{in},i} F_{\text{in},i}}{\sum_{i=1}^{n_{\text{in}}} F_{\text{in},i}} \quad (5)$$

$$F_{\text{M}} = \sum_{i=1}^{n_{\text{in}}} F_{\text{in},i} \quad (6)$$

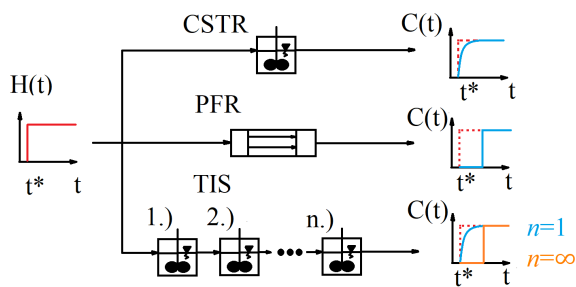


Figure 1: Step responses of ideal flow models [14]

For unit D:

$$\vec{c}_D = \vec{\alpha}c_{in} \quad (7)$$

$$\vec{F}_D = \vec{\alpha}F_{in} \quad (8)$$

The volumetric flow rate (F) entering and exiting the units is also provided by assuming a constant temperature and dilute solutions. The models establish relationships between the volume of the unit (V), the inlet velocity (v) and the inlet as well as actual concentrations in each idealized unit (c). The concentration is introduced as a function of time (t) and/or Cartesian coordinates (x). In the case of the distributor unit, the outlet concentration and flow rate depend on the division rate (α). The idealized CSTR and PFR models exhibit characteristic responses to known input signals such as the Heaviside step function (H) or the Dirac delta function (δ). The step response (C) of the ideal flow models as well as the serial combination of CSTR units in the Tanks in Series (TIS) model are shown in Fig.1.

The response functions can be used to characterize the residence time distribution (RTD) of a chemical species within the system [14]. Therefore, a popular identification method is to obtain the step response of the system and use the RTD function as a basis for identifying the structure of a compartment and the connections between the various compartments. Claudel et al. [15] employed the discipline of possibility theory to provide a method for estimating the structure of a compartment in a unit based on the RTD of the unit and the physical description of the system. They introduced “possibility” and “necessity” rules as well as weighing factors for these rules to assess the RTD function. They summarized the results of the rules to propose the structure of a compartment based on the characteristics of the RTD function.

Egedy et al. [13] used a qualitative approach to identify the structures of compartments in various systems. Their developed algorithm utilized qualitative indicators of the RTD function in an identification algorithm to propose and filter out various CM structures based on their fitness. Approaches which use the CFD model as a basis for the estimation of the CM structure have also become popular in recent studies. Delafosse et al. [16] utilized CFD methods to create a CM structure for approximating the flow characteristics of a bioreactor. Fogarasi et al. [17] developed the CM of a copper leaching reactor based on

experimental and CFD results. Using the CM, they optimized the operational parameters of the leaching reactor. Nauha et al. [18] used a hybrid CFD/CM approach to investigate industrial bioreactors and predict the effects of equipment scale-up on mixing properties within the unit. Weber et al. [19] investigated the use of a hybrid CFD-based CM model for analysing a multiphase loop-reactor. They used the CM model to estimate the mass transfer and drop size distribution within the liquid-liquid extraction part of the loop reactor.

While all of these publications contained significant contributions towards the development of the CFD/CM hybrid model approach, they mostly suffer from the fact that the compartmentalization was conducted manually. Algorithms to automatize the identification of CM structures from CFD have been proposed before. Bezzo et al. [8, 20] used spatial partitioning in their works to develop an algorithm that is capable of aggregating volumes in a unit into compartments and estimating the cross flow between the compartments based on CFD results. Tajssoleiman et al. [21] utilized a similar methodology for the classification of zones within a bioreactor that, based on CFD results, yielded distinctive flow patterns and clustered the results into a CM. Nørregaard et al. [22] developed an algorithm to identify CM structures based on CFD results by using hypothesis-driven logic. They evaluated circumferential, axial and radial bulk flows at different locations within a continuous stirred tank reactor. Using the obtained flow profile, they developed the CM model which resulted in a structure with 56 compartments.

Over the course of this work, the goal was to develop an algorithm capable of identifying the CM structure of a system based on results obtained from CFD methods. The algorithm utilizes two steps to first identify the CM structure and then the flow rates between the individual compartments. Expectations for the algorithm were

- Production of compartments that accurately correspond to the investigated volumes of the physical system
- A small number of compartments to make the CM practical for online computations
- Possibility to integrate empirical knowledge about the system into the compartmentalization process

In future works, the possibility of using the acquired CM as a basis for a fault diagnostic system will be explored.

2. Modelling concept

The proposed algorithm uses CFD results concerning the velocity field within a unit as a basis for identifying the structure of CMs. After partitioning the unit into numerous smaller cells, the algorithm utilizes fuzzy logic to evaluate the local velocity field within the cells and categorize them into one of the idealized models. Adjacent

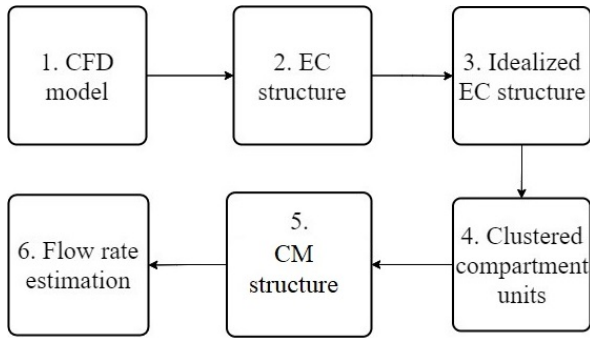


Figure 2: The proposed algorithm

cells that exhibit similar flow behaviour are agglomerated to form compartments showing idealized behaviour. The flow rate between the individual compartments is estimated through optimization. The chart of the proposed algorithm is displayed in Fig. 2.

To summarize the procedure, the compartmentalization process is conducted over six steps.

1. Calculation of a reliable steady state estimate for the velocity field of the system in question using CFD methods.
2. Definition of elementary cells (EC) by dividing the investigated volume.
3. Evaluating the flow characteristics in the individual ECs through fuzzy logic and identifying them as CSTR, PFR or dead volumes.
4. Agglomerating adjacent ECs that exhibit similar flow characteristics into compartments.
5. Defining possible connections between compartments based on the physical geometry of the system.
6. Estimating flow rates between linked compartments through an optimization based on the step response function of the system.

The steps of the proposed method and the results derived from it will be presented in a model system derived from the applications library of a commercial CFD simulator (COMSOL Multiphysics Version 5.2a). The top and side views of the system are shown in Fig. 3 with its characteristic dimensions.

To complete the first step of the algorithm, the CFD model of the unit was developed. The system was the model of a wastewater treatment reactor which originally consisted of four baffles, two of which were removed. To model the system, the fluid within the unit was assumed to exhibit the same properties as water. To investigate the behaviour of the system, the steady-state velocity field of the unit as well as the step response function of the system to an inert tracer were necessary.

To obtain these characteristics, the mass, impulse and component mass balance equations of the system have been solved numerically. The impulse balance of the system was solved assuming incompressible turbulent flow

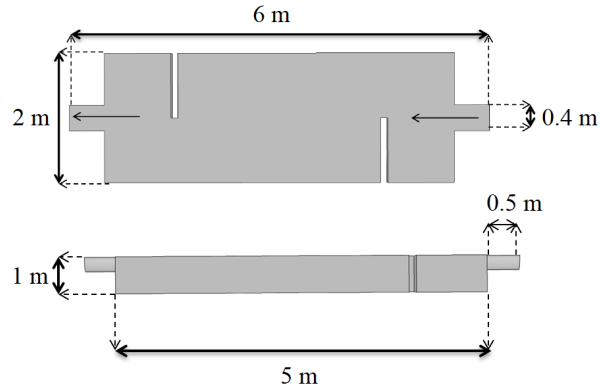


Figure 3: Top and side views of the investigated system

($Re_{\min} \approx 2 \cdot 10^5$ for the flow at the maximum diameter) within the unit using the $k - \epsilon$ turbulence model. The form of the Reynolds-averaged Navier-Stokes equations under these flow conditions is summarized in

$$\rho(\vec{v}\nabla)\vec{v} = \nabla \left[-p\vec{I} + (\mu + \mu_T) \left(\nabla(\vec{v}) + (\nabla\vec{v})^T \right) \right] + F \quad (9)$$

$$\rho\nabla\vec{v} = 0 \quad (10)$$

$$\rho(\nabla\vec{v})k = \nabla \left[\left(\mu + \frac{\mu_T}{\sigma_k} \right) \nabla k \right] + P_k - \rho\epsilon \quad (11)$$

$$\rho(\nabla\vec{v})\epsilon = \nabla \left[\left(\mu + \frac{\mu_T}{\sigma_\epsilon} \right) \nabla \epsilon \right] + C_{\epsilon,1} \frac{\epsilon}{k} P_k - C_{\epsilon,2} \frac{\epsilon^2}{k} \quad (12)$$

$$\mu_T = \rho C_\mu \frac{k^2}{\epsilon} \quad (13)$$

$$P_k = \mu_T \left[\nabla\vec{v} (\nabla\vec{v} + \nabla\vec{v}^T)^{-1} \right] \quad (14)$$

The component mass balance and the step response function were calculated assuming that the velocity field within the unit had reached its steady state. No reactions were considered within the system and the change in the tracer concentration was attributed to convection and diffusion. The tracer was assumed to have the same physical properties as the water within the tank. Under these assumptions, the component mass balance within the unit can be expressed using the partial differential equation

$$\frac{\partial c}{\partial t} = -\vec{v}\nabla c - \nabla(-D\nabla c) \quad (15)$$

To solve the balance equations within the unit, a computational mesh was refined by taking into account both the computation time and accuracy of calculations, which was checked by calculating the relative mass balance error within the unit using

$$E_{\text{mass}} = \frac{\left(\sum_{i=0}^{n_{\text{sim}}} A_{\text{in}} \vec{v}_{\text{in},i} \rho_{\text{in}} - \sum_{i=0}^{n_{\text{sim}}} A_{\text{out}} \vec{v}_{\text{out},i} \rho_{\text{out}} \right)^2}{\max \left(\sum_{i=0}^{n_{\text{sim}}} A_{\text{in}} \vec{v}_{\text{in},i} \rho_{\text{in}}; \sum_{i=0}^{n_{\text{sim}}} A_{\text{out}} \vec{v}_{\text{out},i} \rho_{\text{out}} \right)} \quad (16)$$

Table 1: Parameters of the mesh

Cell type	Tetrahedral
Minimal size (mm)	23.1
Maximal size (mm)	77.4
E_{mass}	$5 \cdot 10^{-4}$

Table 2: Operating conditions of the unit

T (°C)	20
Component	Water
v_{in} (m s^{-1})	0.1
p_{out} (bar)	1
c_{in} (mol m^{-3})	2

The mesh was defined with a construction that allows for both an effectively short computation time and adequate degree of accuracy. The parameters of the mesh are shown in Table 1.

The steady-state velocity field and step response of the unit were calculated under the operating conditions listed in Table 2. After testing different numerical methods, it was found that in the case of the steady-state impulse balance calculations, the Generalized Minimal Residuals iterative algorithm was optimal for computations both with regard to computation time and computational accuracy. In the case of the component mass balance, by taking the same aspects into consideration, the conjugate gradient iterative method was utilized.

After solving the impulse balance of the unit under the previously displayed conditions, the streamlined steady-state velocity profile could be observed in Fig. 4. The streamlines were defined using the internal option of COMSOL, while their densities were set proportional to the local velocity field within an observed volume.

The figure shows that after the fluid enters the unit (on the left-hand side), various zones with different flow characteristics emerge due to the baffles. The flow entering the unit is at first unidirectional with PFR tendencies. The first baffle breaks this flow profile and creates a secluded area within which a well-mixed, circular, vortex-like flow could be observed. On the opposite side of the first baffle, a volume where small-scale mixing occurred could be observed. By following the main path of the flow, the area between the two baffles was a mixed regime with the presence of a significant dead volume. The area obstructed by the second baffle also showed dead volume tendencies. The flow above the second baffle assumed a tendency that was on the verge of being mixed and PFR-like with a clear PFR tendency dominating near the outlet. During the proposed method, the velocity field was converted into a vector field which is shown in Fig. 5. The vectors on the chart represent the tangents of the velocity streamlines within the unit. Their density, length and direction, as with the streamlines, was set to be proportional to the local magnitude and direction of the velocity

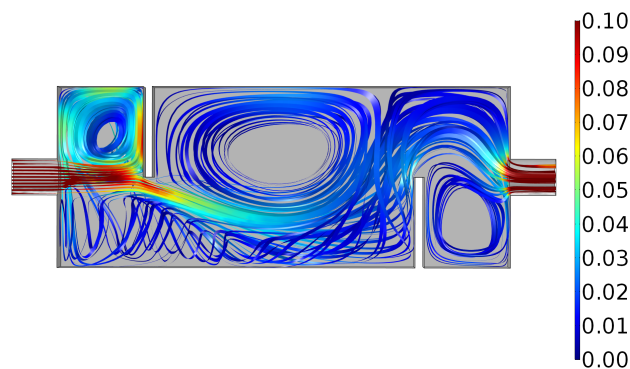
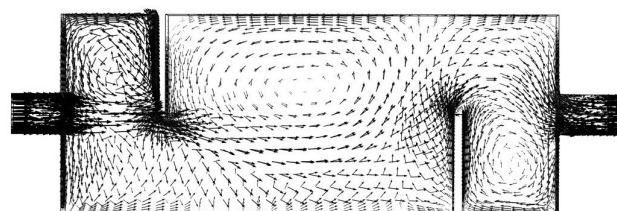
Figure 4: Steady-state streamlines within the unit (m s^{-1})

Figure 5: Steady-state velocity vector field within the unit

field within the reactor.

The step function used to test the system and the response function of the unit are shown in Fig. 6. During the solution of the component mass balance equation diffusion coefficient $D = 10^{-4} \text{ m}^2 \text{ s}^{-1}$ was used.

Based on the step response, the unit exhibited behaviour similar to a mixed CSTR unit combined with a PFR unit. The time delay between the step and response functions (0.05 h) is indicative of PFR behaviour within the system, while the curvature of the response shows CSTR tendencies. Irregularities and jumps within the response, as can be seen at approximately 0.08 h, might be due to internal circulation flows and backflow within the unit.

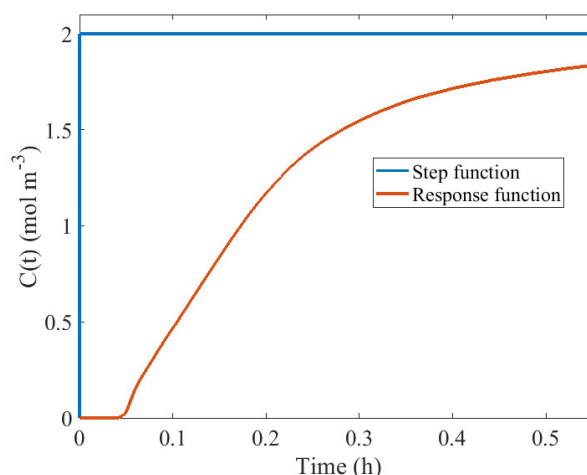


Figure 6: Step and response functions of the unit

3. Modelling results

Once the CFD results had been acquired, the results were processed using MATLAB R2020b. The geometry of the system was partitioned into EC units. Over the course of this investigation, the total volume of the tank reactor (4.96 m³) was broken down into 25 rectangular ECs of equal volumes (0.2 m³) and sizes in accordance with Step 2 of the proposed algorithm (Fig. 2). Investigations using different numbers of ECs were conducted and it was concluded that the most accurate results can be achieved by using a number of ECs where the size of the individual cells is approximately the same as that of the cells used in the CFD simulation. After the partitioning, the vectors characterizing the velocity field displayed in Fig. 5 were observed within the ECs. Since the magnitude, direction and density of the vectors are all based on the attributes of the local velocity field within the tank, key observations can be derived from them about the local flow characteristics within the unit. The following general rules were established:

1. In areas where the flow exhibits PFR characteristics, the velocity vectors are mostly unidirectional with little variance in their magnitude. The magnitude of the velocity vectors is relatively large compared to the magnitude of the inlet velocity.
2. In areas where circular flow is present that exhibits CSTR characteristics, the variance with regard to the directional components of the velocity vectors is higher. The magnitude of the velocity vectors in these areas vary but are comparable to the magnitude of the inlet velocity.
3. In areas where little to no flow is present, also referred to as dead volumes, the magnitude of the velocity vectors is negligible compared to that of the inlet velocity.

Based on these rules, the flow characteristics within a certain volume of the system can be approximately categorized. Therefore, the velocity vectors within the individual ECs were observed and classified based on their flow characteristics. To achieve this, three measures were introduced. The average velocity within a cell (v_1), the variance in the directional components of the velocity vectors within a cell (v_2) and the skewness (v_3) with regard to the distribution of velocity vectors within a cell. To calculate the mean velocity within the cells, the total of the velocity vectors was calculated and averaged. Then the magnitude of the averaged vector was computed from

$$v_1 = \left| \frac{\sum_{i=1}^{n_{\vec{v}}} \vec{v}_i(x, y, z)}{n_{\vec{v}}} \right| \quad (17)$$

The variance and skewness were calculated using similar approaches. Since the coordinates determine the directions, ECs that exhibit PFR behaviour where vectors are unidirectional will have a high mean velocity,

while those that contain circular flow with varying vector directions will generally have lower mean velocities. However, the variance will increase within ECs that exhibit strong circular flow with velocity vectors pointing in various directions. Dead volumes have exceptionally low mean velocities. In the case of all three variables, their numerical values were evaluated in the individual ECs. To properly compare these parameters, the numerical value of each variable within an EC was compared to its maximum value within the investigated system from

$$u_i = \frac{v_i}{\max(v_i)} \quad (18)$$

Therefore, for each variable, a quantity was produced that determines its fractional value compared to its maximum value within the unit. The values of the three parameters within the system can be seen in Fig. 7.

Fig. 7 shows that the indicated variables can be used to differentiate between the flow behaviour of the unit based on the preliminary rules. The figure also explains the need for the inclusion of the skewness of the velocity distribution. Given that in the area adjacent to the first baffle, the flow velocity was rather high, the variance in the magnitude and direction of the velocity vectors in that area was exceptionally high. Compared to this value, most values of variance within the system were minuscule, except near the outlet where the circular flow met the plug-like flow exiting the reactor. The skewness parameter describes the asymmetry of a given distribution function. In areas with strong circular flow patterns, the directions of the velocity vectors are more evenly distributed on both sides of the mean velocity value, resulting in a more symmetric distribution of the velocity vector direction and lower skewness. However, in areas that exhibit plug flow-like behaviour, the distribution is generally more skewed due to the mostly unidirectional velocity vectors.

After obtaining the three quantities used to characterize the flow, their values within the individual ECs were evaluated in accordance with the previously defined rules to obtain the idealized EC structure mentioned in Step 3 of the algorithm (Fig. 2). During this process, the PFR, CSTR and dead volume characteristics of all the individual ECs were examined by converting the established rules using traditional fuzzy logic [23]. Fuzzy expert systems utilize empirical knowledge from subject-matter experts to characterize and analyze processes [24].

They contain a working memory, inputs, a collection of rules and outputs. The working memory is the culmination of objects O_i , where \mathbf{O} denotes the set of all objects. Objects consist of a fuzzy vector (\vec{V}_i) where all members of the vector are fuzzy sets or fuzzy numbers ($\vec{V}_{i,1}, \vec{V}_{i,2}, \dots, \vec{V}_{i,n}$). These fuzzy sets describe qualitative information about the objects, which in this case were each of the individual ECs. The inputs of the fuzzy expert system were the variables u_i , which were used to describe the flow characteristics within an individual EC.

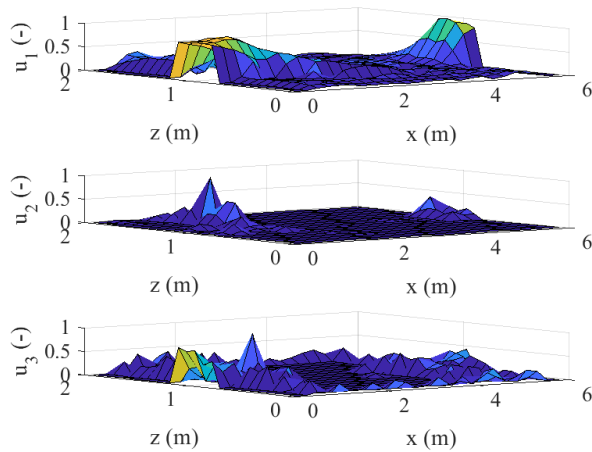


Figure 7: Characteristic velocity variables within the system

A set of rules (\mathbf{R}) was established, which in this case pertains to the flow characteristics within the unit. A fuzzy subset of \mathbf{R} denoted as R with the membership function f_{input} provides $f_{input}(R)$, which symbolizes the level of belief in R for each subset [25]. The degree of belief is a number between 0 and 1 with 0 and 1 denoting disbelief and wholehearted belief in the proposed statement, respectively. The rules are obtained in the form of “IF-THEN” rules with logical operators like “OR”, “AND”, etc. In the case of our system, the real number inputs u_i were converted into fuzzy numbers using monotonic sigmoidal membership functions, their general form is presented

$$f_{input,j}(u_i) = \frac{1}{1 + e^{-\left(\frac{u_i - b}{a}\right)}} \quad (19)$$

$$f_{input,j}(u_i) = 1 - \frac{1}{1 + e^{-\left(\frac{u_i - b}{a}\right)}} \quad (20)$$

for fuzzy numbers with index j generated from input i .

The first equation is used for membership functions which are increasing in tendency, while the latter is for membership functions which are decreasing. Parameters a and b define the spread of the fuzzy numbers either side of their central value and the central values of the fuzzy numbers, respectively. The fuzzy numbers obtained through the membership functions represent the linguistic variables P belonging to the set of basic linguistic variables \mathbf{P} . In our case, these linguistic variables consisted of the set $P_1 = \{\text{high, low}\}$ which was used to describe whether the mean value, variance and skewness of velocity vectors within an EC were high or low compared to the maximum value of the respective attribute within the system.

The output actions define a fuzzy set of conclusions. The set \mathbf{G} represents the set of possible conclusions of the expert system. A subset of this set represents the out-

Table 3: Parameters of the fuzzy membership functions

f_{input}	a	b	f_{output}	a	b
Input _{1,low}	0.01	0.05	Output _{low}	0.02	0.4
Input _{2,low}	0.01	0.05			
Input _{3,low}	0.02	0.1			
Input _{1,high}	0.03	0.2	Output _{high}	0.02	0.6
Input _{2,high}	0.02	0.2			
Input _{3,high}	0.03	0.3			

puts of our object, which in our case meant the characteristics of the PFR, CSTR and dead volume of individual ECs [25]. Given that the linguistic variables $P_2 = \{\text{high, low}\}$ are represented by membership function $f_{output,j}$ for each characteristic, the membership functions are monotonic and sigmoidal like the input membership functions as shown in

$$f_{output,j}(f_{input,j}(R)) = \frac{1}{1 + e^{-\left(\frac{f_{input,j}(R) - b}{a}\right)}} \quad (21)$$

$$f_{output,j}(f_{input,j}(R)) = 1 - \frac{1}{1 + e^{-\left(\frac{f_{input,j}(R) - b}{a}\right)}} \quad (22)$$

In this equation, $f_{input,j}(R)$ represents the degree of belief in R for each subset. After defuzzification, the expert system returned crisp values that determined the PFR, CSTR and dead-volume characteristics within each EC.

The input and output membership functions can be observed in Fig. 8 and Fig. 9, respectively. Since the output membership functions in the case of all three outputs were identical, they have only been displayed once. The first index within the legend represents the input which the membership function belongs to, while the second one corresponds to the linguistic subsets (1 \rightarrow Low, 2 \rightarrow High) [25].

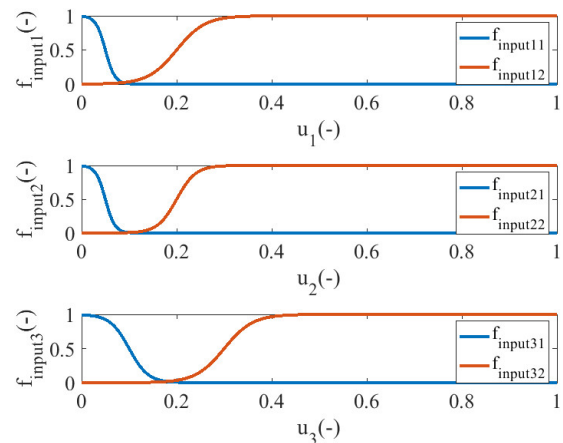


Figure 8: Input membership functions

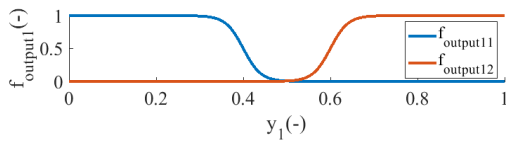


Figure 9: Output membership functions

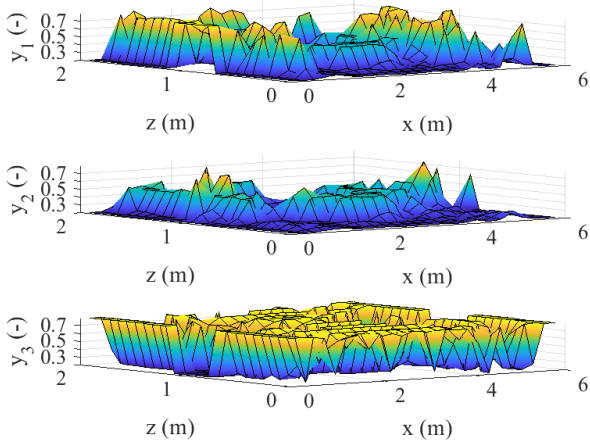


Figure 10: Flow characteristics of the different EC units

The parameters a and b of the membership functions are displayed in Table 3. Using the expert system, the flow characteristics of the ECs were characterized. The PFR (y_1), CSTR (y_2) and dead volume (y_3) characteristics within the ECs are shown in Fig. 10.

To achieve a flow map that describes the behaviour of the velocity field within each unit, the three characteristics were unified. The weighted average of the three output characteristics was computed and a function defined by $\text{Im}(L) \in [0, 2]$ where $L(y_1, y_2) = 0$ corresponds to the pure dead-volume behaviour, $L(y_1, y_2) = 1$ denotes the pure CSTR behaviour and $L(y_1, y_2) = 2$ stands for the pure PFR behaviour. $L(y_1, y_2)$ in each individual EC was calculated from

$$L(y_1, y_2) = \frac{2 \cdot y_1 + y_2}{3}. \quad (23)$$

Since the weighting factor of the dead-volume behaviour is 0, it was not included in the equation. The results of the process are shown in Fig. 11.

The correlation between Fig. 4 and Fig. 11 is apparent. The model predicts clear PFR behaviour within the flow near the inlet and outlet which can also be observed from Fig. 4. The area beyond the inlet and bounded by the first baffle showed CSTR tendencies with some PFR behaviour near the walls. A dead volume could be observed at the centre of the stirred volume which was similar to in the middle of the vortex seen in Fig. 4. The area opposite the volume bounded by the first baffle exhibited dead-volume tendencies with a low velocity and occasional circular flow patterns, indicative of slight CSTR behaviour. The area between the two baffles showed mixed, CSTR

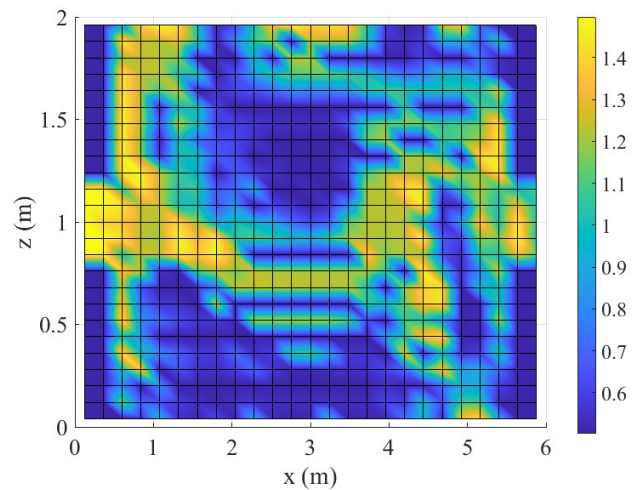


Figure 11: Characteristic flow behaviour within the unit

tendencies with a noticeable dead volume present in the middle of the vortex, as can be seen in Fig. 4. The area bounded by the second baffle mainly exhibited dead-volume tendencies with a medium degree of circulation. The volume opposite it consisted of a mixed flow. The flow near the outlet, as noted before, exhibited PFR tendencies.

The figure presents an approximately accurate description of the flow characteristics when compared to the streamlines obtained from the CFD methods. However, due to fuzzification and the weighted average calculations to ascertain the flow tendencies within the unit, individual flow characteristics of the ECs are unclear. To clarify these values, limits were introduced to clearly categorize the flow behaviour of all ECs, which were calculated according to Eq. 24. The limits for this clustering process were determined by observing flow patterns obtained using various limits. It was found that these limits facilitated the most efficient clustering and resulted in a cluster which strongly resembled the flow characteristics observed in the CFD results.

$$L_{\text{disc}}(y_1, y_2) = \begin{cases} 2, & \text{if } L(y_1, y_2) > 1.25 \\ 1, & \text{if } 1.25 \geq L(y_1, y_2) \geq 0.75 \\ 0, & \text{otherwise} \end{cases} \quad (24)$$

This equation shows that the values of the corrected function are discrete, that is, the ECs are categorized into three idealized classes of flow depending on which pure idealized class their behaviour most resembles.

The plot displaying the flowchart with ECs containing the corrected values is shown in Fig. 12. The figure also indicates the locations of the inlet, outlet and baffles. Since a rectangular mesh was used to divide the system into ECs, the locations that were not part of the geometry and the baffles were also included in the calculations. Since no flow was present at these locations, they have been categorized as clear dead volumes, which can be seen by comparing Fig. 11 and Fig. 12. For the sake of clarity, these areas were removed from the corrected fig-

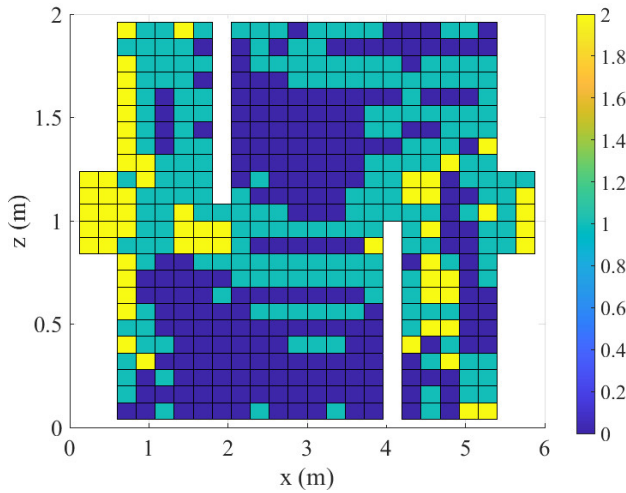


Figure 12: Recognized flow behaviour within the ECs

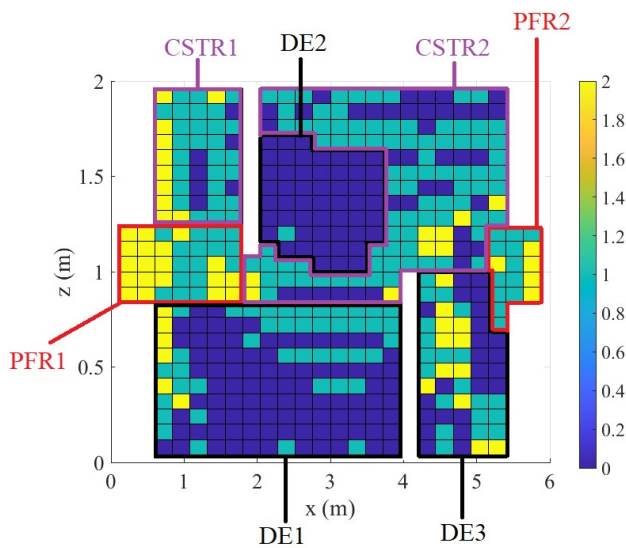


Figure 13: Defined compartments within the system

ure.

Fig. 12 shows a clear map indicating the idealized flow behaviour of individual ECs within the unit. Once agglomerated, adjacent ECs that exhibited similar characteristics could be grouped to form compartments of idealized behaviour in accordance with Step 4 of the proposed algorithm (Fig. 2). The agglomeration of the ECs within this paper was conducted manually. The resulting set of compartments is shown in Fig. 13.

The unit was partitioned into seven compartments, namely two PFR regions, two CSTR regions and three dead volumes. The volumes of the compartments were evaluated by totalling the volumes of the individual ECs which were assigned as part of the compartment in question. It can be seen that the resulting structure of the compartment strongly resembles the results obtained through CFD methods seen in Fig. 4. Based on the defined structure, a CM consisting of the compartments that exhibited idealized behaviour was constructed to complete Step 5 of the algorithm (Fig. 2). The CM structure is displayed

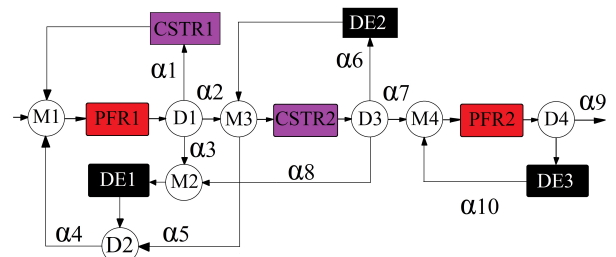


Figure 14: Estimated CM structure

in Fig. 14.

The constructed CM structure contains the previously identified compartments seen in Fig. 13. Connections between the different compartments were established through the use of theoretical mixer and divider units. During the evaluation of the possible connections between compartments, the geometry of the system was taken into account as well, e.g., the placement of baffles, positions of adjacent compartments, etc. The models of the individual compartments, mixers and dividers were formulated according to the equations provided in the Introduction.

After obtaining the CM structure, Step 6 of the identification algorithm (Fig. 2) involved estimating the flow rates between compartments. In the case of the structure shown in Fig. 14, the flow rates between compartments were defined through the division rates (α_i) of the D units. These values describe the ratio of mass flow entering the i th adjacent compartment compared to the total mass flow leaving the j th reference compartment.

For the identification of the α_i values optimization was conducted in MATLAB R2020b through the Simulink interface. The constructed CM structure was defined in Simulink along with its connections and individual compartments. The system of differential and algebraic equations describing the behaviour of the system were solved numerically using Rosenbrock methods for solving stiff differential equations. The step response of the CM was observed as a function of the α_i values and an objective function was formulated to estimate the α values displayed in

$$E_C(\vec{\alpha}) = \frac{\sum_{i=1}^{n_{sim}} (C_{CFD,i} - C_{CM,i})^2}{\max(\sum_{i=1}^{n_{sim}} C_{CFD,i}; \sum_{i=1}^{n_{sim}} C_{CM,i})} \quad (25)$$

The objective function estimates the squared difference between the step response function acquired through CFD methods and the CM over the observed discrete-time horizon relative to the maxima of the sum of the two functions. To minimize the objective function with regard to the α_i values, the interior-point method was utilized. The step response function of the system obtained through CFD methods and the optimized CM can be seen in Fig. 15.

The resulting figure shows that the step response of the CM after optimization fits the step response of the system obtained through CFD methods well with an aver-

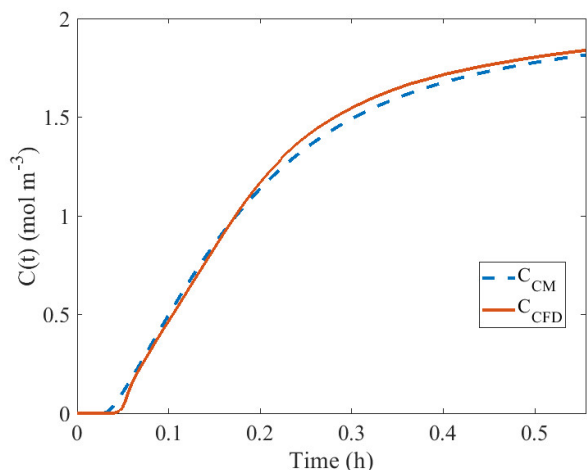


Figure 15: Step response of the system with CFD methods and CM

Table 4: Optimized α parameters

α_1	0.7	α_6	0
α_2	0.25	α_7	1
α_3	0.05	α_8	0
α_4	0.8	α_9	0.95
α_5	0.2	α_{10}	0.05

age fit of 92%. The optimized model parameters rounded up to two decimal places are presented in Table 4.

The estimated parameters in Table 4 are also in line with the general CM structure. It should be noted that the optimized α parameters of flows entering dead volumes ($\alpha_3, \alpha_6, \alpha_8, \alpha_{10}$) were exceptionally low, moreover, sometimes not even detectable when rounded up to two decimal places. This indicates that the step response of the system is most similar to the response obtained through CFD methods if almost no flow enters the listed volumes, indicating that they are truly dead volumes from a flow perspective.

4. Conclusions

Over the course of this study, the process of creating CMs from results obtained through CFD simulations has been presented. The proposed algorithm consisted of two phases. In the first phase, the CM structure of the object was defined. For these investigations, the steady-state velocity field of the system was utilized. The system was partitioned into ECs in which the local velocity field was investigated. By analyzing the direction and magnitude of local velocity vectors within the ECs using fuzzy logic, a set of rules was established to categorize the behaviour of individual ECs and correlate these ECs to units exhibiting idealized behaviour.

To characterize the flow behaviour, three measures were defined based on the distribution of the magnitude and direction of velocity vectors within individual ECs. Three types of ECs were considered, ones in which the

flow is well-mixed and circular, similar to a CSTR, ones in which the flow is unidirectional and resembles that found in a PFR, and ones in which little to no flow is present, that is, dead-volume behaviour is exhibited.

After the qualitative analysis using fuzzy logic, each EC was assigned an idealized trait. Adjacent ECs that exhibited similar traits were clustered into compartments showing idealized behaviour. After determining the idealized compartments, the flow rates between these compartments were estimated through optimization by calculating the flow rates for which the sum of the squared difference between the step response of the CFD model and CM was minimal. The estimated parameters and the observed compartments showed a strong correlation with the flow patterns which could be observed within the CFD results. The method is capable of effectively analyzing CFD results and converting them into CMs in a structured framework while also allowing the addition of empirical knowledge using fuzzy logic. The proposed method could serve as a basis for the estimation of robust and computationally inexpensive a priori models to describe equipment utilized within the chemical industry. The physical correlation between the model compartments and the actual flow regimes within the unit could provide opportunities to develop a priori model-based diagnostic strategies for online fault detection among many other applications.

5. Acknowledgements

This work was supported by the TKP2020-IKA-07 project financed under the 2020-4.1.1-TKP2020 Thematic Excellence Programme by the National Research, Development and Innovation Fund of Hungary.

Nomenclature

Fuzzy sets

\vec{V}	Set of fuzzy vectors/numbers
\mathbb{G}	Set of possible fuzzy conclusions
\mathbb{O}	Set of fuzzy objects
\mathbb{P}	Set of linguistic fuzzy variables
\mathbb{R}	Set of fuzzy rules

Greek letters

α	Distribution ratio [–]
ϵ	Turbulent dissipation rate [$\text{m}^2 \text{s}^{-3}$]
μ	Kinematic viscosity [$\text{m}^2 \text{s}^{-1}$]
μ_T	Turbulent viscosity [$\text{kg m}^{-1} \text{s}^{-1}$]
ρ	Density [kg m^{-3}]
σ_ϵ	Constant for change in ϵ [–]
σ_k	Constant for change in k [–]
τ	Residence time [h]

Latin letters

\vec{F}	Force [N]
-----------	-----------

\vec{I}	Impulse [kg m s ⁻¹]
\vec{v}	Velocity [m s ⁻¹]
A	Surface [m ²]
a	Fuzzy membership function central value [–]
b	Fuzzy membership function variance [–]
C	Step response function [mol m ⁻³]
c	Species concentration [mol m ⁻³]
$C_{\epsilon,1}$	Dissipation rate calculation constant 1 [–]
$C_{\epsilon,2}$	Dissipation rate calculation constant 2 [–]
C_{μ}	Turbulent viscosity calculation constant [–]
D	Diffusion rate [m ² s ⁻¹]
E	Error function [–]
F	Flow rate [m ³ s ⁻¹]
f	Fuzzy membership function
H	Heaviside (Step) function [mol m ⁻³]
i, j	Numeric indices [–]
k	Turbulent kinetic energy [m ² s ⁻²]
L	Continuous flow characteristic function [–]
L_{disc}	Discretized flow characteristic function [–]
n	Absolute number [–]
p	Pressure [Pa]
P_k	Turbulent kinetic energy due to mean velocity variations [kg m ⁻¹ s ⁻¹]
T	Temperature [°C]
t	Time [h]
u	Fuzzy expert system input variable [–]
V	Volume [m ³]
x	Longitudinal coordinate [m]
y	Fuzzy expert system output variable [–]
z	Lateral coordinate [m]

REFERENCES

- [1] Venkatasubramanian, V.; Rengaswamy, R.; Yin, K.; Kavuri, S.N.: A review of process fault detection and diagnosis: Part I: Quantitative model-based methods., *Comput. Chem. Eng.*, 2003, **27**(3), 293–311 DOI: [10.1016/S0098-1354\(02\)00160-6](https://doi.org/10.1016/S0098-1354(02)00160-6)
- [2] Broughton, E.: The Bhopal disaster and its aftermath: a review., *Environ. Health*, 2005, **4**(1), 1–6 DOI: [10.1186/1476-069X-4-6](https://doi.org/10.1186/1476-069X-4-6)
- [3] Isimite, J.; Rubini, P.: A dynamic HAZOP case study using the Texas City refinery explosion., *J. Loss. Prev. Process. Ind.*, 2016, **40**(1), 496–501 DOI: [10.1016/j.jlp.2016.01.025](https://doi.org/10.1016/j.jlp.2016.01.025)
- [4] J., G.: Fault detection and diagnosis in engineering systems. (CRC press), 1998. ISBN: 9780367400439
- [5] Venkatasubramanian, V.; Rengaswamy, R.; Kavuri, S.N.: A review of process fault detection and diagnosis: Part II: Qualitative models and search strategies., *Comput. Chem. Eng.*, 2003, **27**(3), 313–326 DOI: [10.1016/S0098-1354\(02\)00161-8](https://doi.org/10.1016/S0098-1354(02)00161-8)
- [6] Venkatasubramanian, V.; Rengaswamy, R.; Kavuri, S.N.; Yin, K.: A review of process fault detection and diagnosis: Part III: Process history based methods., *Comput. Chem. Eng.*, 2003, **27**(3), 327–346 DOI: [10.1016/S0098-1354\(02\)00162-X](https://doi.org/10.1016/S0098-1354(02)00162-X)
- [7] Solin, P.; Segeth, K.; Dolezel, I.: Higher-order finite element methods. (CRC press), 2003. ISBN: 9780429205279
- [8] Bezzo, F.; Macchietto, S.; Pantelides, C.C.: A general methodology for hybrid multizonal/CFD models: Part I. Theoretical framework., *Comput. Chem. Eng.*, 2004, **28**(4), 501–511 DOI: [10.1016/j.compchemeng.2003.08.004](https://doi.org/10.1016/j.compchemeng.2003.08.004)
- [9] Savic, R.M.; Jonker, D.M.; Kerbusch, T.; Karlsson, M.O.: Implementation of a transit compartment model for describing drug absorption in pharmacokinetic studies., *J. Pharmacokinet. Pharmacodyn.*, 2007, **34**(5), 711–726 DOI: [10.1007/s10928-007-9066-0](https://doi.org/10.1007/s10928-007-9066-0)
- [10] Pigou, M.; Morchain, J.: Investigating the interactions between physical and biological heterogeneities in bioreactors using compartment, population balance and metabolic models., *Chem. Eng. Sci.*, 2015, **126**(1), 267–282 DOI: [10.1016/j.ces.2014.11.035](https://doi.org/10.1016/j.ces.2014.11.035)
- [11] Spann, R.; Gernaey, K.V.; Sin, G.: A compartment model for risk-based monitoring of lactic acid bacteria cultivations., *Biochem. Eng. J.*, 2019, **151**(1), 2–11 DOI: [10.1016/j.bej.2019.107293](https://doi.org/10.1016/j.bej.2019.107293)
- [12] Kaur, G.; Singh, M.; Matsoukas, T.; Kumar, J. and De Beer, T.; Nopens, I.: Two-compartment modeling and dynamics of top-sprayed fluidized bed granulator., *Appl. Math. Model.*, 2019, **68**(1), 267–280 DOI: [10.1016/j.apm.2018.11.028](https://doi.org/10.1016/j.apm.2018.11.028)
- [13] Egedy, A.; Varga, T.; Chován, T.: Compartment model structure identification with qualitative methods for a stirred vessel., *Math. Comput. Model. Dyn. Syst.*, 2013, **19**(2), 115–132 DOI: [10.1080/13873954.2012.700939](https://doi.org/10.1080/13873954.2012.700939)
- [14] Levenspiel, O.: Chemical reaction engineering. (John Wiley & Sons), 1999. ISBN: 978-0-471-25424-9
- [15] Claudel, S.; Fonteix, C.; Leclerc, J.P.; Lintz, H.G.: Application of the possibility theory to the compartment modelling of flow pattern in industrial processes., *Chem. Eng. Sci.*, 2003, **58**(17), 4005–4016 DOI: [10.1016/S0009-2509\(03\)00269-0](https://doi.org/10.1016/S0009-2509(03)00269-0)
- [16] Delafosse, A.; Collignon, M.L.; Calvo, S.; Delvigne, F.; Crine, M.; Thonart, P.; Toye, D.: CFD-based compartment model for description of mixing in bioreactors., *Chem. Eng. Sci.*, 2014, **106**(1), 76–85 DOI: [10.1016/j.ces.2013.11.033](https://doi.org/10.1016/j.ces.2013.11.033)
- [17] Fogarasi, S.; Egedy, A.; Imre-Lucaci, F.; Varga, T.; Chován, T.: Hybrid CFD-compartment approach for modelling and optimisation of a leaching reactor., *Comput. Aided Chem. Eng.*, 2014, **33**(1), 1255–1260 DOI: [10.1016/B978-0-444-63455-9.50044-1](https://doi.org/10.1016/B978-0-444-63455-9.50044-1)
- [18] Nauha, E.K.; Kálal, Z.; Ali, J.M.; Alopaeus, V.: Compartmental modeling of large stirred

- tank bioreactors with high gas volume fractions., *Chem. Eng. J.*, 2018, **334**(1), 2319–2334 DOI: [10.1016/j.cej.2017.11.182](https://doi.org/10.1016/j.cej.2017.11.182)
- [19] Weber, B.; von Campenhausen, M.; Maßmann, T.; Bednarz, A.; Jupke, A.: CFD based compartment-model for a multiphase loop-reactor., *Chem. Eng. Sci.: X*, 2019, **2**, 100010 DOI: [10.1016/j.cesx.2019.100010](https://doi.org/10.1016/j.cesx.2019.100010)
- [20] Bezzo, F.; Macchietto, S.: A general methodology for hybrid multizonal/CFD models: Part II. Automatic zoning., *Comput. Chem. Eng.*, 2004, **28**(4), 513–525 DOI: [10.1016/j.compchemeng.2003.08.010](https://doi.org/10.1016/j.compchemeng.2003.08.010)
- [21] Tajssoleiman, T.; Spann, R.; Bach, C.; Gernaey, K.V.; Huusom, J.K.; Krühne, U.: A CFD based automatic method for compartment model development., *Comput. Chem. Eng.*, 2019, **123**(1), 236–245 DOI: [10.1016/j.compchemeng.2018.12.015](https://doi.org/10.1016/j.compchemeng.2018.12.015)
- [22] Nørregaard, A.; Bach, C.; Krühne, U.; Borgbjerg, U.; Gernaey, K.V.: Hypothesis-driven compartment model for stirred bioreactors utilizing computational fluid dynamics and multiple pH sensors., *Chem. Eng. J.*, 2019, **356**(1), 161–169 DOI: [10.1016/j.cej.2018.08.191](https://doi.org/10.1016/j.cej.2018.08.191)
- [23] Zadeh, L.: Fuzzy logic., *Computer*, 1988, **21**(4), 83–93 DOI: [10.1109/2.53](https://doi.org/10.1109/2.53)
- [24] Hadjimichael, M.: A fuzzy expert system for aviation risk assessment., *Expert Syst. Appl.*, 2009, **36**(3), 6512–6519 DOI: [10.1016/j.eswa.2008.07.081](https://doi.org/10.1016/j.eswa.2008.07.081)
- [25] Buckley, J.J.; Siler, W.; Tucker, D.: A fuzzy expert system., *Fuzzy Sets Syst.*, 1986, **20**(1), 1–16 DOI: [10.1016/S0165-0114\(86\)80027-6](https://doi.org/10.1016/S0165-0114(86)80027-6)

POLYVINYLPIRROLIDONE AS A CORROSION INHIBITOR FOR CARBON STEEL IN A PERCHLORIC ACID SOLUTION: EFFECT OF STRUCTURAL SIZE

ABBES BENCHADLI¹, TARIK ATTAR*^{1,2}, BOULANOVAR MESSAOUDI^{1,2}, AND ESMA CHOUKCHOU-BRAHAM¹

¹Laboratory of Toxicomed, University Abou Beker Belkaid Tlemcen, BP 119, 13000 Tlemcen, ALGERIA

²Higher School of Applied Sciences Tlemcen, BP 165 RP Bel horizon, 13000 Tlemcen, ALGERIA

Polymers are materials composed of macromolecules characterized by duplicates of smaller molecules that are covalently bonded together to provide a set of properties. Corrosion inhibition by such compounds is usually attributed to their adsorption on the metal-solution interface. The inhibition effect of different sizes of polyvinylpyrrolidone (PVP) on the corrosion of carbon steel (C-steel) in solutions of perchloric acid was investigated. The inhibition efficiency increases as the size of the inhibitor and its concentration increases, but decreases as the temperature increases and can reach a value of 81.53 % and $5.0 \times 10^{-3} \text{ mol L}^{-1}$ (PVP: $58,000 \text{ g mol}^{-1}$) at 30 °C. The most remarkable inhibition efficiency was confirmed by the presence of the film formed on the metal surface by scanning electron microscopy. The kinetic and thermodynamic parameters for the corrosion of C-steel and adsorption of the inhibitor were determined and discussed. The combination of PVP with potassium iodide produced a strong synergistic effect on the inhibition of C-steel corrosion leading to a significant improvement in the inhibition efficiency. Quantum chemical parameters were studied using density functional theory to determine the possible relationship between the inhibitor and its electronic properties.

Keywords: Polyvinylpyrrolidone, Weight loss, Synergistic effect, SEM, DFT

1. Introduction

Despite its relatively limited corrosion resistance, carbon steel (C-steel) is widely used in chemical processing, nuclear and fossil fuel power plants, the oil and gas industries, construction and metal-processing equipment, mining, pipelines, transportation and marine applications. The corrosion of C-steel in acidic media is important because of its high mechanical properties and low cost [1]. Levels of corrosion increase rapidly after the failure of the preventive barrier and are followed by a number of reactions that change the properties as well as composition of the metal surface [2].

Generally speaking, a corrosion inhibitor is a compound that reduces or stops the rate of metal dissolution whenever introduced or added in small quantities to a corrosive environment by producing a preventive barrier film [3]. Moreover, a good corrosion inhibitor presents many characteristics such as high solubility, non-toxicity, biodegradability, stability, short- and long-term durability and low cost. The inhibition efficiency is often related to different variables like the structural chemistry and amount of the inhibitor in the medium, the nature of the metal and aggressive electrolyte as well as its pH,

temperature, and immersion time [4, 5].

Organic inhibitors mostly contain triple bonds, aromatic rings, and heteroatoms such as O, N, and S which are active centers for the adsorption process on the metal surface [6]. These atoms are characterized by higher basicity and electron density, thus act as corrosion inhibitors. Organic compounds behave as effective inhibitors due to their ability to be adsorbed onto the metal surface. Green corrosion inhibitors are drawing much attention in the field of corrosion because of their biodegradability, safety, renewability and ecological acceptability [7]. The mechanism of adsorption can be either physical or chemical as a result of the protective layer or adsorbed blanketing on the metal surface [8]. Chemical adsorption implies charge transfer or charge sharing from the adsorbate to the atoms of the metal surface in order to form a coordinate bond. The free energy of chemisorption is higher than that of physisorption. The latter type is due to electrostatic attraction between the inhibiting organic ions or dipoles and the electrically charged surface of the metal.

The use of polymers as corrosion inhibitors has attracted considerable attention recently because of their ability to form complexes with metal ions on the electrode surface. These complexes occupy a large surface,

*Correspondence: att_tarik@yahoo.fr

thus blanketing the metal surface and protecting it from corrosive agents present in the solution [9, 10]. The applications of polyvinylpyrrolidone (PVP) are extensive in pharmaceutical, medicinal, cosmetics and industrial products [11]. It is used in food additives, adhesives, membranes, ceramics, paper, coatings and personal care products, e.g., toothpastes and shampoos, as well as in batteries, paints, environmental applications, etc. [12]. The PVP added to iodine (I_2) forms a complex called povidone-iodine (PVP-I) that is widely used in various products like liquid soaps, ointments, surgical scrubs and pessaries due to its antiseptic properties or as an antimicrobial and antibacterial agent in medical devices [13]. This complex is commonly known under the trade names of Wokadine, Pyodine, or even Betadine. Quantum chemistry calculations have been extensively used to explain experimental phenomena. They have proven to be very effective in evaluating the corrosion inhibition efficiency [14]. The conceptual density functional theory (CDFT) has been used to analyze the molecular activity of inhibitors [15].

The aim of the present work is to determine the effect of the size of polyvinylpyrrolidone compounds and their protection efficiencies on the corrosion of carbon steel in a solution of 1 M perchloric acid by weight loss methods. The synergistic corrosion inhibition effect between PVP and potassium iodide (KI) was also investigated and the steel surface examined by scanning electron microscopy (SEM). Afterwards, quantum chemical calculations using DFT were performed to elucidate the interaction between the main constituents of PVP and the carbon-steel surface.

2. Experimental

2.1 Material preparation

Four forms of PVP polymers with molecular weights of 8,000, 29,000, 40,000 and 58,000 $g\ mol^{-1}$ and the vinylpyrrolidone monomer were purchased from Sigma-Aldrich. The blank solution was 1 M perchloric acid prepared by diluting a concentrated solution of $HClO_4$ (Sigma-Aldrich). The tested samples employed in this work and the chemical composition of C-steel are shown in Table 1.

2.2 Preparation of the test sample

Before conducting any tests, the samples of C-steel were mechanically abraded using different grades of emery paper, namely 100, 400, 600, 800, 1000, and 1200, before

being washed with distilled water, degreased with acetone, air-dried then dipped into the corrosive or/and anti-corrosive medium. These samples were used to study the loss in weight.

2.3 Weight loss technique

Weight loss techniques provide more realistic results with regard to uniform corrosion than electrochemical techniques because the experimental conditions simulate real-life conditions. Weight loss measurements of the C-steel samples were calculated in the solution of perchloric acid with and without the addition of different concentrations and molecular weights of polyvinylpyrrolidone. Loss in the weight of the specimen was resolved by measuring the difference in weight between the carbon-steel substrates before and after being placed in the acidic medium. Each sample was weighed by an electronic balance ($\pm 0.0001\ g$) before being placed in the acid solution (50 mL). The immersion time was 2 h within the temperature range of 293 – 333 K. The experiments were each performed three times and the average weight loss noted [16]. The corrosion rate (CR) ($mg\ cm^{-2}\ h^{-1}$) was determined by [17]

$$CR = (m_b - m_a)/tS, \quad (1)$$

where m_b and m_a denote the weight losses (mg) before and after being immersed in the acidic solution, respectively, S stands for the total surface area of the specimen (cm^2), and t represents the immersion time (h). The inhibition efficiency (IE) (%) was calculated using [17]

$$IE = 100 (CR' - CR)/CR' \quad (2)$$

The degree of surface coverage (θ) which represents the part of the metal surface covered in inhibitor molecules was calculated using [17]

$$\theta = 1 - CR/CR', \quad (3)$$

where CR' and CR denote the corrosion rates of C-steel samples in the absence and presence of polyvinylpyrrolidone, respectively.

2.4 Synergism between inhibitors and iodide ions

One potential method to cost-effectively increase the corrosion inhibition efficiency is to use the concept of synergism and employ a combination of inhibitors [18]. The synergism phenomenon in terms of corrosion inhibition results in an improvement in the capacity of the inhibitor

Table 1: Chemical composition of C-steel (wt. %).

C	Mn	Cu	Cr	Ni	Si	S	Ti	Co	Fe
0.370	0.680	0.160	0.077	0.059	0.023	0.016	0.011	0.009	Bal

to resist corrosion in the presence of secondary compounds in the corrosive medium [19]. The presence of halide ions in acid media containing organic inhibitors has been found to stabilize the adsorption of organic cations, which leads to an increase in inhibition efficiency [20]. It has been shown that the synergistic effect of halide ions increases in the following order: chloride (Cl^-) < bromide (Br^-) < iodide (I) [21]. Iodide exhibited a higher synergistic effect compared to the other halide ions because of its large size and ease of polarization [22]. Therefore, the purpose of this study is to increase the inhibition efficiency by using iodide ions in a similar way to the synergistic effect with inhibitors tested with regard to the corrosion of C-steel in a solution of 1 M perchloric acid.

In order to determine the synergistic effect between inhibitors and iodide ions, the synergistic parameter (S_θ) was calculated from [23]

$$S_\theta = (1 - \theta_{\text{PVP+KI}})/(1 - \theta'_{\text{PVP+KI}}) \quad (4)$$

and

$$\theta_{\text{PVP+KI}} = (\theta_{\text{PVP}} + \theta_{\text{KI}}) - (\theta_{\text{PVP}} \times \theta_{\text{KI}}), \quad (5)$$

where θ_{PVP} denotes the surface coverage of the PVP inhibitor, θ_{KI} stands for the surface coverage of KI, and $\theta'_{\text{PVP+KI}}$ represents the combined surface coverage of PVP and KI.

If S_θ is less than unity, this indicates an antagonistic effect which may lead to competitive adsorption and when S_θ approaches unity, the inhibitor compounds stop interacting with each other, whereas when S_θ is greater than unity, a synergistic effect exists between the selected inhibitors [24].

2.5 Scanning electron microscopy (SEM)

The surface morphology of the specimens of carbon steel was studied by SEM using a Hitachi TM1000 Tabletop scanning electron microscope at a scale of 100 μm and magnification of $\times 1.0\text{K}$. The samples were immersed in a solution of 1 M HClO_4 and the effect of the inhibitors investigated. After 24 h of immersion under optimum conditions, the SEM images of both the polished specimens of carbon steel and those immersed in perchloric acid in the presence and absence of inhibitors were captured.

2.6 Theoretical calculations

The DFT method using the B3LYP/6-31G* approach was employed to test the quantum chemical calculations of the inhibitor using the Gaussian 09 program package. The values of the highest molecular orbitals (E_{HOMO}) and the lowest occupied ones (E_{LUMO}) were calculated. Other parameters such as electronegativity (χ), softness (σ), global hardness (η), electron affinity (A) and the ionization potential (I) were determined by Koopmans' theorem [25].

The HOMO energy is related to the ionization potential (I), whereas the LUMO energy is dependent on the electron affinity (A), as is shown in [26]

$$A = -E_{\text{LUMO}}, \quad I = -E_{\text{HOMO}}. \quad (6)$$

The energy gap (ΔE) and global electronic chemical potential (μ) are determined from

$$\Delta E = E_{\text{LUMO}} - E_{\text{HOMO}} \quad (7)$$

and

$$\mu = \frac{1}{2}(E_{\text{LUMO}} + E_{\text{HOMO}}), \quad (8)$$

respectively [27, 28]. Using the electron affinity (A) and ionization potential (I), the electronegativity (χ) and global hardness (η) can be calculated from

$$\chi = \frac{1}{2}(I + A) \quad (9)$$

and

$$\eta = \frac{1}{2}(I - A) \quad (10)$$

respectively [29]. Global softness (σ) demonstrates the capacity of an atom or group of atoms to receive electrons and is estimated from [30]

$$\sigma = 1/\eta. \quad (11)$$

The electrophilicity index (ω) is calculated from [31, 32]

$$\omega = \mu^2/2\eta. \quad (12)$$

The number of electrons transferred (ΔN) was calculated from [33]

$$\Delta N = (\chi_{\text{Fe}} - \chi_{\text{Inh}})/2(\eta_{\text{Fe}} + \eta_{\text{Inh}}), \quad (13)$$

where χ_{Fe} and χ_{Inh} denote the absolute electronegativities of iron and the inhibitor, while η_{Fe} and η_{Inh} stand for the absolute hardness of iron and the inhibitor, respectively. The theoretical values ($\chi = 7 \text{ eV mol}^{-1}$ and $\eta = 0 \text{ eV mol}^{-1}$) for iron were taken from the literature [34].

3. Results and discussion

3.1 Effect of the acid medium

Acidic solutions have been widely applied in industry, e.g., in the removal of mill scale from metal surfaces, acid pickling, acid descaling, acidizing oil wells and industrial acid cleaning. In the oil industry, the acidization of petroleum oil wells, an important stimulation technique, is used to enhance production [35]. HCl , HClO_4 and H_2SO_4 are the most applied acidic solutions because of their highly corrosive nature with regard to many metals and alloys even at low concentrations [36], whereas HNO_3 and H_3PO_4 are used occasionally. In this study, the inhibition efficiencies of polyvinylpyrrolidone are mainly applied in different acid media such as perchloric acid,

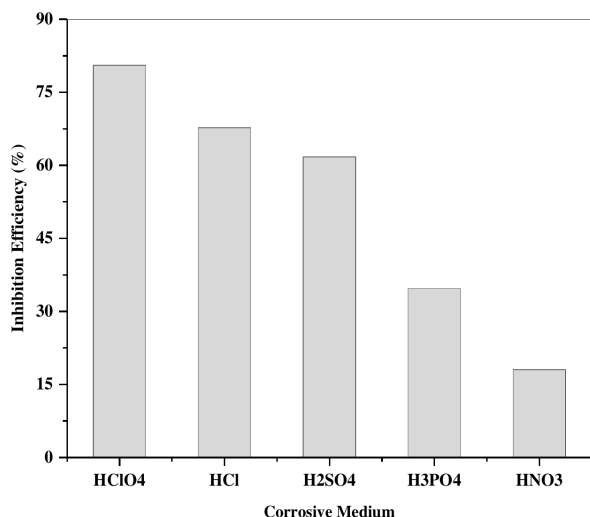


Figure 1: Variation in inhibition efficiency of carbon steel in different acid media (PVP: 58,000 g mol⁻¹ with 1.0 × 10⁻³ mol L⁻¹ of acid medium for 2 h at 303 K).

hydrochloric acid, sulfuric acid, phosphoric acid and nitric acid. According to Fig. 1, the best inhibition efficiency (80.55 %) is obtained in perchloric acid compared to hydrochloric acid (67.74 %), sulfuric acid (61.71 %), phosphoric acid (34.68 %) and nitric acid (18.01 %). This could be due to the beneficial adsorption of perchlorate ions on the C-steel surface.

The inhibitor molecules strongly interact with the metal surface in the presence of perchlorate ions due to the low coordination capacity of perchlorate ions. However, the coordination of chloride, sulfate, phosphate and nitrate ions with the metal surface render it less able to adsorb the inhibitor molecules. In this work, the study was conducted exclusively in perchloric acid because of the better adsorption of PVP in this acid compared to other acids that were tested.

3.2 Effect of concentration and molecular weight

The inhibition effect of PVP on the corrosion of carbon steel at 303 K in 1 M HClO₄ as the corrosive medium was evaluated by a weight loss method. The effect of different molecular weights, namely the monomer and polymers of 8,000, 29,000, 40,000, and 58,000 g mol⁻¹, on the inhibition efficiency (IE) was studied. The dependence of the inhibition efficiency on the concentration as well as on the different molecular weights of PVPs is presented in Fig. 2. The improvement in the inhibition efficiency compared to the polymer concentration and molecular weight of PVPs suggests that more molecules are required to cover the metal surface when the concentration of the inhibitor is low. No further increase in IE beyond 10⁻³ mol L⁻¹ of different molecular weights of PVP is attributed to the saturation of the adsorption process.

The experimental results prove that the PVP with a molecular weight of 58,000 g mol⁻¹ is more effective

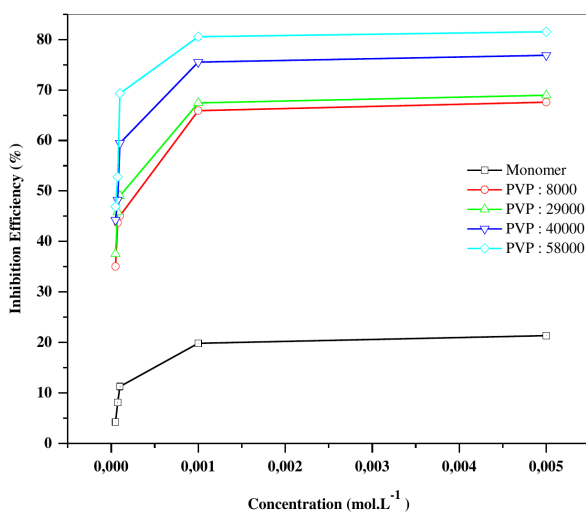


Figure 2: Variation in the inhibition efficiency against concentration in a 1 M HClO₄ solution, using various molecular weights of the inhibitor.

in inhibiting the corrosion of C-steel in the aggressive medium than any other molecular weight of PVP at all concentrations. The monomer presents the least corrosion inhibition at all the concentrations studied and reaches a maximum efficiency of 21.81 % at 5 × 10⁻³ mol L⁻¹.

3.3 Effect of immersion time

The study of this parameter was conducted in order to avoid any confusion between the phenomenon of passivation which could occur if the immersion time is very long and the inhibition rate of the inhibitors. The effect of the immersion time for all the inhibitors tested with regard to IE is shown in the results presented in Fig. 3. The inhibition efficiency is calculated from 1 to 24 hours in uninhibited HClO₄ and in the presence of the optimum concentration of the monomer (10⁻³ mol L⁻¹) and different molecular weights of PVP at 303 K. It can be concluded that the inhibition efficiency increases as the immersion time lengthens due to the stability of the adsorbed layer on the surface of C-steel up until 2 hours of immersion at different concentrations and molecular weights of the inhibitors. The inhibition efficiency decreases from 80.55 % to 68.25 % after immersion times of PVP58000 of 2 hours and 24 hours, respectively. This may be explained by the desorption of inhibitor molecules from the C-steel surface and the instability of the inhibitor film on the metal surface [37].

3.4 Effect of temperature and activation energy

The effect of the temperature introduces many changes on the metal surface such as adsorption, desorption, rearrangement or decomposition of the inhibitor. The effect of the temperature and different molecular weights of PVP on the corrosion inhibition of C-steel in 1 M HClO₄

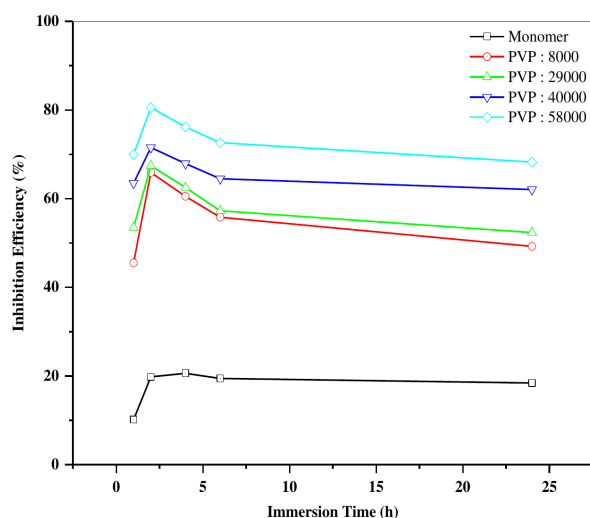


Figure 3: Variation in the inhibition efficiency against immersion time for carbon steel at various molecular weights of inhibition in a 1 M HClO₄ solution.

was studied between 293 and 333 K to determine the dependence of the inhibition efficiency on the temperature and corrosion behavior of C-steel in perchloric acid in the presence of inhibitors. According to the results presented in Table 2, at higher temperatures there is an appreciable decrease in the adsorption of the inhibitors on the metal surface leading to a rise in the corrosion rate.

At a temperature of 60°C, the polyvinylpyrrolidone with a molecular weight of 58,000 g mol⁻¹ showed a maximum inhibition efficiency of 69.41 %, while that of the monomer was only 6.35 %. Those for the other molecular weights of PVP, namely 8000, 29000, and 40000 g mol⁻¹, were equal to 56.55, 59.43 and 63.81 %, respectively, at the maximum tested concentration of 5 × 10⁻³ mol L⁻¹. An increase in the temperature of the solution reduces the inhibition effect by facilitating the counter-process of desorption [38]. The high rate of dissolution of C-steel in a 1 M HClO₄ solution observed at elevated temperatures could be attributed to an increase in the dissolution energy effect acquired by the corrosive agent within the aggressive medium. Moreover, the desorption of the adsorbed inhibitor caused by enhanced agitation of the solution as a result of higher rates at which hydrogen gas evolves as the temperature rises is possible and can cause the capacity of the inhibitor to be adsorbed on the C-steel surface to be reduced [39]. For chemical adsorption, the inhibition efficiency is expected to increase as the temperature rises, but for physical adsorption, the inhibition efficiency is expected to decrease as the temperature increases [40]. The Arrhenius equation can be used to show the effect of the temperature on the inhibition performance of the studied compounds [41]:

$$CR = A \exp(-E_{act}/RT), \quad (14)$$

where CR denotes the corrosion rate of carbon steel, A stands for the pre-exponential factor of the Arrhenius

equation, E_{act} (kJ mol⁻¹) represents the activation energy, R refers to the gas constant (8.314 J mol⁻¹ K⁻¹) and T is the temperature (K).

The activation enthalpy ΔH_{act} and entropy of activation ΔS_{act} can be calculated by the following transition state equation [42]:

$$\log\left(\frac{CR}{T}\right) = \log\left(\frac{R}{N_A h}\right) + \frac{\Delta S_{act}}{2.3R} - \frac{\Delta H_{act}}{2.3RT}, \quad (15)$$

where R denotes the gas constant, N_A stands for Avogadro's number, and h represents Planck's constant. A plot of $\log(CR/T)$ against $1/T$ yields a straight line with a gradient of $-\Delta H_{act}/2.3R$ and an intercept of $(\log(R/N_A h) + \Delta S_{act}/2.3R)$ from which the values of ΔH_{act} and ΔS_{act} can be calculated as is presented in Table 3.

$\Delta G_{act} > 0$, which means a non-spontaneous corrosion reaction, the rate of which increases as the concentration of the inhibitor increases [42]. The entropies of activation were negative in the absence and presence of inhibitors implying that a decrease in disorder occurred as the reaction proceeded. The higher activation energy of the process in the presence of an inhibitor compared to in its absence is attributed to its physisorption, whereas the opposite is a result of its chemisorption [43]. The positive values of the activation enthalpy in the presence and absence of different concentrations of the inhibitors reflect the endothermic nature of C-steel dissolution. This simply means that the dissolution process of steel is difficult [44].

3.5 Adsorption isotherm

The adsorption isotherms provide information about the interaction between the inhibitor and C-steel surface [45]. The type of interaction is related to the adsorption of inhibitor compounds as a result of chemisorption and physisorption [46]. It depends on many factors, e.g., the number of adsorption centers, mode of interactions with the metal surface, molecular weight and structure of the inhibitor. The data were used graphically using different isotherms such as Frumkin, Temkin and Langmuir. The Langmuir adsorption isotherm was found to best describe the adsorption. It can be seen that the results of the surface coverage in the presence of inhibitors are in good agreement with the weight loss technique (Eq. 3). The Langmuir adsorption isotherm model was employed using [47]

$$\frac{C}{\theta} = \frac{1}{K_{ads}} + C, \quad (16)$$

where θ denotes the surface coverage by the inhibitor molecules, C stands for the concentration, and K_{ads} represents the equilibrium constant for the adsorption-desorption process.

The value of the equilibrium constant obtained can be used to calculate the standard free energy by from [48]

$$\Delta G_{ads} = -RT \log(55.5 K_{ads}), \quad (17)$$

Table 2: The percentage inhibition efficiency of C-steel in 1 M HClO₄ using five inhibitors tested between 293 and 333 K.

	C (mol L ⁻¹)	293 K	303 K	313 K	323 K	333 K
Monomer	5×10^{-5}	6.25	4.22	3.1	2.25	1.50
	7.5×10^{-5}	8.33	8.05	5.63	4.55	3.42
	10^{-4}	15.5	11.25	8.1	6.6	4.2
	1×10^{-3}	20.65	19.81	10.43	8.7	6.15
	5×10^{-3}	21.97	21.34	10.5	8.78	6.35
8,000	5×10^{-5}	43.37	35.01	24.17	16.85	10.19
	7.5×10^{-5}	50.19	43.67	35.82	23.42	16.29
	10^{-4}	60.53	45.07	43.98	33.75	30.7
	10^{-3}	78.2	65.9	62.2	58.85	56.42
	5×10^{-3}	78.46	67.59	62.35	58.95	56.55
29,000	5×10^{-5}	45.5	37.55	29.24	19.31	12.23
	7.5×10^{-5}	62.51	45.81	41.21	25.93	21.54
	10^{-4}	65.17	49.02	45.03	41.97	36.91
	10^{-3}	82.17	67.44	64.61	61.35	59.39
	5×10^{-3}	82.12	68.95	64.68	61.42	59.43
40,000	5×10^{-5}	50.18	44.22	36.86	22.16	15.95
	7.5×10^{-5}	66.57	48.21	45.13	28.18	23.73
	10^{-4}	70.41	59.47	50.32	45.73	43.33
	10^{-3}	84.09	75.53	70.88	68.41	63.6
	5×10^{-3}	84.27	76.86	70.9	68.54	63.81
58,000	5×10^{-5}	55.19	46.89	38.91	26.17	19.07
	7.5×10^{-5}	70.07	52.77	46.50	31.04	25.66
	10^{-4}	75.23	69.33	58.53	52.72	48.71
	10^{-3}	85.1	80.55	77.21	75.13	69.34
	5×10^{-3}	85.34	81.53	77.29	75.2	69.41

Table 3: Thermodynamic activation parameters of the dissolution of carbon steel in 1 M HClO₄ in the absence and presence of different concentrations and molecular weights of the inhibitors by applying Arrhenius and transition state plots.

	C_{inh} (mol L ⁻¹)	E_{act} (kJ mol ⁻¹)	ΔH_{act} (kJ mol ⁻¹)	ΔS_{act} (J mol ⁻¹ K ⁻¹)	ΔG_{act} 303K (kJ mol ⁻¹)
HClO ₄	1	58.79	56.2	-105.43	88.21
Monomer	5×10^{-5}	59.8	57.21	-102.48	88.26
	7.5×10^{-5}	59.81	57.22	-102.66	88.31
	10^{-4}	61.08	58.48	-98.88	88.44
	10^{-3}	61.99	59.39	-96.27	88.55
	5×10^{-3}	62.05	59.46	-96.08	88.57
8,000	5×10^{-5}	68.35	65.75	-77.44	89.21
	7.5×10^{-5}	69.69	67.1	-74.13	89.56
	10^{-4}	69.53	66.94	-75.84	89.91
	10^{-3}	71.74	69.14	-72.78	91.19
	5×10^{-3}	72.28	69.69	-72.16	91.55
29,000	5×10^{-5}	68.61	66.01	-76.95	89.32
	7.5×10^{-5}	73.42	70.82	-63.04	89.92
	10^{-4}	69.61	67.02	-76.33	90.14
	10^{-3}	73.83	71.23	-66.83	91.48
	5×10^{-3}	74.07	71.47	-67.14	91.81
40,000	5×10^{-5}	69.96	67.37	-73.26	89.57
	7.5×10^{-5}	74.95	72.38	-58.54	90.11
	10^{-4}	71.86	69.27	-70.24	90.55
	10^{-3}	74.45	71.86	-66.34	91.96
	5×10^{-3}	74.95	72.36	-64.86	92.01
58,000	5.0×10^{-5}	71.07	68.47	-70.18	89.73
	7.5×10^{-5}	76.77	74.18	-53.27	90.32
	10^{-4}	74.21	71.61	-64.18	91.05
	10^{-3}	72.53	69.94	-74.07	92.38
	5×10^{-3}	73.15	70.55	-72.22	92.43

Table 4: Thermodynamic parameters for the adsorption of five inhibitors on C-steel tested in a 1 M HClO₄ solution at different temperatures.

	<i>T</i> (K)	<i>R</i> ²	ΔH_{ads} (kJ mol ⁻¹)	ΔS_{ads} (J mol ⁻¹ K ⁻¹)	ΔG_{ads} (kJ mol ⁻¹)
Monomer	293	0.999		28.76	-28.64
	303	0.999		28	-28.7
	313	0.999	-20.21	30.68	-29.82
	323	0.999		29.93	-29.88
	333	0.999		27.7	-29.44
8,000	293	0.999		-9.42	-34.39
	303	0.999		-7.72	-34.81
	313	0.999	-37.15	-8.79	-34.4
	323	0.999		-8.42	-34.43
	333	0.998		-9.13	-34.11
29,000	293	0.999		-4.44	-35.12
	303	0.999		-3.99	-35.21
	313	0.999	-36.42	-2.68	-35.58
	323	0.999		-4.18	-35.07
	333	0.998		-4.44	-34.95
40,000	293	0.999		1.09	-35.59
	303	0.999		0.13	-35.31
	313	0.999	-35.27	2.81	-36.15
	323	0.999		0.15	-35.32
	333	0.999		1.05	-35.62
58,000	293	0.999		-7.06	-36.2
	303	0.999		-6.91	-36.18
	313	0.999	-38.29	-6.17	-36.34
	323	0.999		-7.74	-35.77
	333	0.999		-6.67	-36.05

where *R* denotes the gas constant (8.314 J mol⁻¹ K⁻¹) and *T* stands for the absolute temperature (K). The constant value of 55.5 mol L⁻¹ is the concentration of water in dilute aqueous solutions.

The calculated changes in the enthalpy, entropy and free energy of adsorption are presented in Table 4. In this study, the negative values of the enthalpy of adsorption, which vary between -20.21 and -38.29 kJ mol⁻¹, indicate that the adsorption of the inhibitors on the C-steel is an exothermic process. High values of ΔG_{ads} show that the inhibitor is strongly adsorbed on the metal surface in the corrosive media. The negative values of the free energy of adsorption indicate that the adsorption of the inhibitors on the steel surface is spontaneous. The variation in ΔG_{ads} between -29.06 and -36.34 kJ mol⁻¹ indicates that the adsorption of inhibitors on the carbon steel surface in a solution of 1 M perchloric acid at between 293 and 333 K is a mixture of chemical and physical adsorption. The determination of the free energy of adsorption provides information about the strength of adsorption of the molecules. Generally speaking, values of ΔG_{ads} between -40 and -20 kJ mol⁻¹ are consistent with physical adsorption, while those below -40 kJ mol⁻¹ are indicative of chemical adsorption [49].

3.6 Synergistic effect

Synergistic inhibition is brought about by the combination of PVP58000 and iodide ions for the corrosion of C-steel in 1M HClO₄ as halide ions have a greater tendency to be adsorbed on the surface as a result of their attraction to organic cations. The relationship between the efficiency and concentration of each inhibitor added by potassium iodide at different temperatures is shown in Table 5. The obtained results in the present study clearly show that the inhibition efficiency was substantially enhanced following the addition of KI and could occur because of the existence of synergism between different concentrations of the tested inhibitor and iodide ions.

The values of *S*_θ are higher than those for all concentrations indicating that the interaction between PVP and KI is a synergistic effect. It is well known that the maximum efficiency reaches 97.18 % as a result of the synergistic effect, while for PVP in the absence of KI it is 85.34 %. The inhibition efficiency increased following the addition of potassium iodide ions due to the synergistic effect but decreased as the temperature rose. It has been concluded that more effective barrier films of inhibitor molecules are produced on the surface of the sample due to synergy, thus blocking the active sites on the steel surface to protect carbon steel from corrosion [50].

Table 5: Synergism parameter (S_θ) for different concentrations of PVP58000 and in the presence of a solution of 5×10^{-6} M KI from weight loss measurements at 293, 313, and 333 K.

C (mol/L)	293 K			313 K			333 K		
	IE(PVP)	IE(PVP+KI)	S_θ	IE(PVP)	IE(PVP+KI)	S_θ	IE(PVP)	IE(PVP+KI)	S_θ
5×10^{-5}	55.19	91.29	1.25	38.91	55.53	1.12	19.07	32.89	1.05
10^{-4}	75.23	94.57	1.11	58.53	73.32	1.27	48.71	62.62	1.2
5×10^{-3}	85.34	97.18	1.26	77.29	83.68	1.14	69.41	74.92	1.07

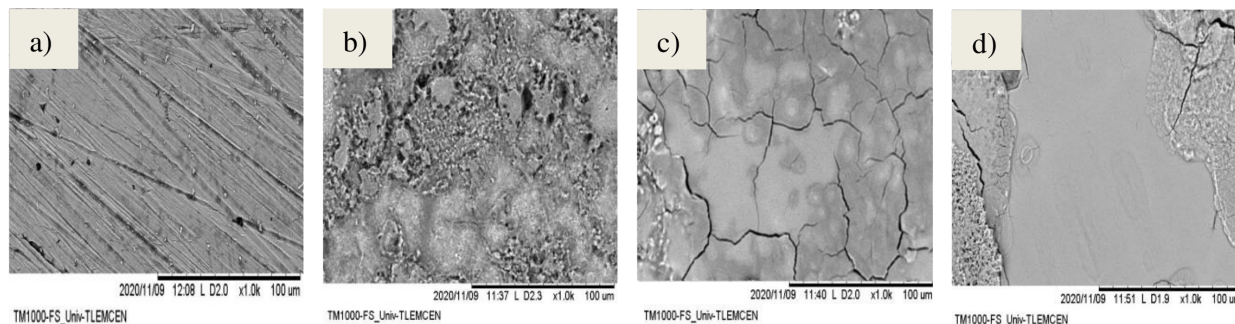


Figure 4: SEM images of carbon steel (a) before immersion, (b) after immersion in the acidic solution (1 M HClO_4) in the absence of inhibitors, (c) after immersion in the acidic solution containing 5×10^{-3} M PVP58000, and (d): (c) + KI.

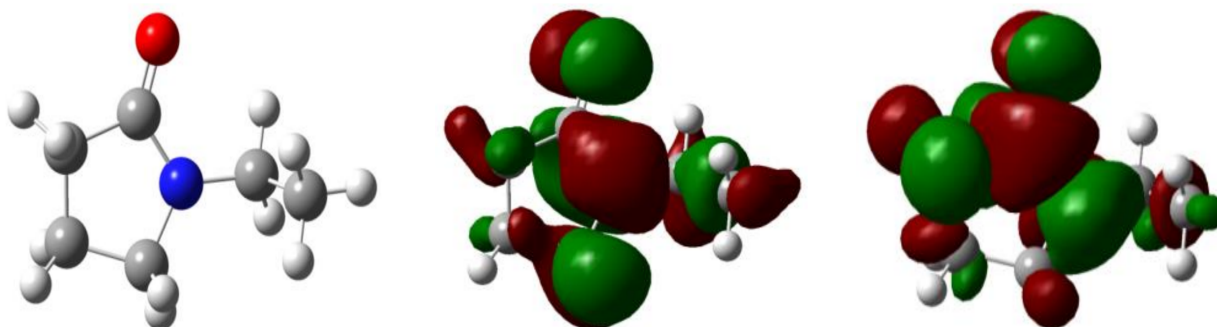


Figure 5: (a) Optimized molecular structure, (b) HOMO and (c) LUMO of the protonated Polyvinylpyrrolidone molecule.

3.7 Scanning electron microscopy

To confirm adsorption of the polyvinylpyrrolidone on the carbon-steel surface in the presence and absence of the inhibitor in 1 M HClO_4 , scanning electron microscopy experiments were carried out. Fig. 4a shows the surface morphology before corrosion testing. It is obvious that specimens immersed in the solution in the absence of PVP58000 and KI additives show significant degradation of the surface and pitting corrosion is evident from the surface morphology as is shown in Fig. 4b. However, in the presence of PVP, an obvious reduction in the degradation of the surface is shown. This amelioration can be attributed to the adsorption of PVP on the metal surface and the formation of a protective film, thereby isolating the carbon-steel surface (Fig. 4c). The addition of KI improves the degree of inhibition and the stability of the corrosion product on the steel surface as is shown in Fig. 4d. This indicates that the adsorption of iodide ions on carbon steel leads to the formation of more stable films. The scanning electron microscopy (SEM) study confirmed that the corrosion inhibition of carbon steel and synergistic effect occur following the adsorption of

inhibitor molecules on the metal surface.

3.8 Quantum chemical calculations

The experimental study was completed by a theoretical study at the B3LYP/6-31G* level in order to correlate the results obtained experimentally with the molecular structure and electrical properties of Polyvinylpyrrolidone as is presented in Fig. 5.

The energies of the HOMO and LUMO, total energy (E), number of transferred electrons (ΔN), softness (σ), electrophilicity index (ω) and global hardness (η) were calculated and are listed in Table 6:

The energy gap between the HOMO and LUMO is another important descriptor that must be considered. In Table 6, it is shown that the PVP inhibitor has a higher E_{HOMO} (-6.29 eV) energy and lower E_{LUMO} (1.01 eV) energy as well as a small energy gap $G_{\text{gap}} \sim -7.3$ eV between E_{HOMO} and E_{LUMO} . This strengthens its inhibitory action on the C-steel surface. The electrophilicity index is another important parameter which shows the tendency of the molecule to accept electron(s). The charge transfer of 0.6 eV indicates that the PVP inhibitor

Table 6: HOMO and LUMO energies as well as the global reactivity indices μ , σ , ω , ΔN , and G_{ap} for Polyvinylpyrrolidone compound at the B3LYP/6-31G* level of theory.

E_{HOMO} (eV)	E_{LUMO} (eV)	μ (eV)	η (eV)	σ (eV ⁻¹)	ω (eV)	ΔN (eV)	G_{ap} (eV)
-6.29	1.01	-2.65	3.65	0.27	0.96	0.6	7.3

is a strong electron donor [3]. Generally, if the fractions of electrons transferred are less than 3.6 eV, the inhibition efficiency increases by increasing the electron donating capacity on the metal surface [51]. Softness (σ) and chemical hardness (η) are important chemical properties to measure molecular reactivity and stability. Therefore, the chemical reactivity increases as the inhibition efficiency of adsorption rises. Actually, the molecule with the smallest chemical hardness should exhibit the greatest inhibition efficiency [52]. The PVP inhibitor exhibits a good degree of chemical reactivity on the metal surface due to the decrease in the chemical hardness ($\eta = 3.65$ eV) and increase in the softness ($\sigma = 0.27$ eV⁻¹).

3.9 Inhibition mechanism

Different techniques (Weight loss, SEM, and DFT) were used to determine the inhibitory effect of different molecular weights of Polyvinylpyrrolidone on the corrosion of C-steel in a solution of perchloric acid. PVP58000 yielded the highest corrosion inhibition, while the monomer exhibited the lowest. The results showed that inhibition efficiencies on carbon steel increase as the concentration of the inhibitors (PVPs) rises and were enhanced following the addition of potassium iodide (KI) due to synergism. It is well known that iron exhibits coordinate affinity towards nitrogen-, sulfur- and oxygen-bearing ligands [53]. In this study, the electron pairs of oxygen and nitrogen atoms are responsible for chemical bonding to the C-steel surface.

4. Conclusion

The obtained results showed that Polyvinylpyrrolidone is effective in the presence of perchloric acid. The studied compounds exhibited good corrosion inhibition performances of PVP (58,000 g mol⁻¹) on C-steel in perchloric acid and its activity increased as the concentration of the inhibitor rose, while the efficacy decreased as the temperature increased. The thermodynamic adsorption parameters show that the studied inhibitors are adsorbed on the C-steel surface following an exothermic, spontaneous process. Inhibition is achieved by the adsorption of the molecules on the C-steel surface and follows the Langmuir isotherm. The inhibition efficiency increased following the addition of iodide ions due to the synergistic effect and decreased by increasing the temperature. The SEM images illustrated the formation of a protective layer on the carbon-steel surface as well as supported the corrosion inhibition activity and synergistic effect. The inhibition efficiencies of the inhibitors obtained from the weight loss method and density functional theory are in good agreement.

Acknowledgements

The authors would like to express their gratitude to the University Abou Beker Belkaid Tlemcen and Higher School of Applied Sciences Tlemcen for their fruitful support.

REFERENCES

- [1] Rasheeda, K.; Vijaya, D.P.A.; Krishnaprasad, P.A.; Samshuddin, S.: Pyrimidine derivatives as potential corrosion inhibitors for steel in acid medium—An overview, *Int. J. Corros. Scale Inhib.*, 2018, **7**(1), 48–61 DOI: 10.17675/2305-6894-2018-7-1-5
- [2] Dwivedi, D.; Lepkova, K.; Becker, T.: Emerging surface characterization techniques for carbon steel corrosion: a critical brief review, *Proc. R. Soc. A*, 2017, **473**(2199), 1–19 DOI: 10.1098/rspa.2016.0852
- [3] Attar, T.; Benchadli, A.; Messaoudi, B.; Benhadria, N.; Choukchou-Braham, E.: Experimental and Theoretical Studies of Eosin Y Dye as Corrosion Inhibitors for Carbon Steel in Perchloric Acid Solution, *Chem. React. Eng. Catal.*, 2020, **15**(2), 454–464 DOI: 10.9767/bcrec.15.2.7753.454-464
- [4] Bouraoui, M.M.; Chettouh, S.; Chouchane, T.; Khellaf, N.: Inhibition Efficiency of cinnamon oil as a green corrosion inhibitor, *Journal of Bio and Tribo-Corrosion*, 2019, **5**(28), 1–9 DOI: 10.1007/s40735-019-0221-0
- [5] Attar, T.; Larabi, L.; Harek, Y.: The Inhibition effect of potassium iodide on the corrosion of pure iron in sulfuric acid, *Adv. Chem.*, 2014, **2014**, 1–5 DOI: 10.1155/2014/827514
- [6] Xhanari, K.; Finšgar, M.; Knez, Z.; Hrnčič, M.K.: Green corrosion inhibitors for aluminium and its alloys: a review, *RSC Adv.*, 2017, **7**(44), 27299–27330 DOI: 10.1039/C7RA03944A
- [7] Marzorati, S.; Verotta, L.; Trasatti, S.P.: Green Corrosion Inhibitors from Natural Sources and Biomass Wastes, *Molecules*, 2018, **24**(1), 1–24 DOI: 10.3390/molecules24010048
- [8] Attar, T.; Benchadli, A.; Choukchou-Braham, E.: Corrosion inhibition of carbon steel in perchloric acid by potassium iodide, *Int. J. Adv. Chem.*, 2019, **7**(1), 35–41 DOI: 10.14419/ijac.v7i1.19651
- [9] Azzam, E.M.S.; Abd El-Salam, H.M.; Reham, A.M.; Shaban, S.M.; Shokry, A.: Control the corrosion of mild steel using synthesized polymers based on polyacrylamide, *Egypt. J. Pet.*, 2018, **27**(4), 897–910 DOI: 10.1016/j.ejpe.2018.01.006

- [10] Nawaz, M.; Yusuf, N.; Habib, S.: Development and Properties of Polymeric Nanocomposite Coatings, *Polymers*, 2019, **11**(5), 1–14 DOI: [10.3390/polym11050852](https://doi.org/10.3390/polym11050852)
- [11] Teodorescu, M.; Bercea, M.: Poly(vinylpyrrolidone)–A Versatile Polymer for Biomedical and Beyond Medical Applications, *Polym. Plast. Technol.*, 2015, **54**(9), 923–943 DOI: [10.1080/03602559.2014.979506](https://doi.org/10.1080/03602559.2014.979506)
- [12] Zhi, X.; Fang, H.; Bao, C.; Shen, G.; Zhang, J.: The immunotoxicity of graphene oxides and the effect of PVP-coating, *Biomaterials*, 2013, **34**(21), 5254–5261 DOI: [10.1016/j.biomaterials.2013.03.024](https://doi.org/10.1016/j.biomaterials.2013.03.024)
- [13] Jones, D.S.; Djokic, J.; Gorman, S.P.: The resistance of polyvinylpyrrolidone-iodine-poly(ϵ -caprolactone) blends to adherence of *Escherichia coli*, *Biomaterials*, 2005, **26**(14), 2013–2020 DOI: [10.1016/j.biomaterials.2004.06.001](https://doi.org/10.1016/j.biomaterials.2004.06.001)
- [14] Lgaz, H.; Salghi, R.; Ali, I.H.: Corrosion inhibition behavior of 9-hydroxyrisperidone as a green corrosion inhibitor for mild steel in hydrochloric acid: electrochemical, DFT and MD simulations studies, *Int. J. Electrochem. Sci.*, 2018, **13**(1), 250–264 DOI: [10.20964/2018.01.26](https://doi.org/10.20964/2018.01.26)
- [15] Liu, S.B.: Conceptual density functional theory and some recent developments, *Acta Phys. -Chim. Sin.*, 2009, **25**(3), 590–600 DOI: [10.3866/pku.whxb20090332](https://doi.org/10.3866/pku.whxb20090332)
- [16] Aiad, I.; Shaban, S.; El-Sukkary, M.; El-Awady, M.; Soliman, E.: Electrical and Gravimetric Estimation of the Corrosion Inhibition of Three Synthesized Cationic Surfactants N-(3-(Butylidene Amino) Propyl)-N, N-Dimethyl Alkan-1-Ammonium Bromide Derivatives in 1 M HCl, *J. Mater. Eng.*, 2017, **6**(1), 429–450 DOI: [10.1520/MPC20170001](https://doi.org/10.1520/MPC20170001)
- [17] Attar, T.; Larabi, L.; Harek, Y.: Inhibition effect of potassium iodide on the corrosion of carbon steel (XC 38) in acidic medium, *Int. J. Adv. Chem.*, 2014, **2**(2), 139–142 DOI: [10.14419/ijac.v2i2.3272](https://doi.org/10.14419/ijac.v2i2.3272)
- [18] Javadian, S.; Yousefi, A.; Neshati, J.: Synergistic effect of mixed cationic and anionic surfactants on the corrosion inhibitor behavior of mild steel in 3.5% NaCl, *Appl. Surf. Sci.*, 2013, **285**, 674–681 DOI: [10.1016/j.apsusc.2013.08.109](https://doi.org/10.1016/j.apsusc.2013.08.109)
- [19] Aslam, R.; Mobin, M.; Aslam, J.: Sugar based N,N-didodecyl-N,N-digluconamide ethylenediamine gemini surfactant as corrosion inhibitor for mild steel in 3.5% NaCl solution-effect of synergistic KI additive, *Sci. Rep.*, 2018, **8**, 3690 DOI: [10.1038/s41598-018-21175-6](https://doi.org/10.1038/s41598-018-21175-6)
- [20] Eduok, U.M.; Umoren, S.A.; Udoh, A.P.: Synergistic inhibition effects between leaves and stem extracts of *Sida acuta* and iodide ion for mild steel corrosion in 1 M H₂SO₄ solutions, *Arab. J. Chem.*, 2012, **5**, 325–337 DOI: [10.1016/j.arabjc.2010.09.006](https://doi.org/10.1016/j.arabjc.2010.09.006)
- [21] Pramudita, M.; Sukirno, S.; Nasikin, M.: Synergistic Corrosion Inhibition Effect of Rice Husk Extract and KI for Mild Steel in H₂SO₄ Solution, *Bull. Chem. React. Eng. Catal.*, 2019, **14**(3), 697–704 DOI: [10.9767/bcrec.14.3.4249.697-704](https://doi.org/10.9767/bcrec.14.3.4249.697-704)
- [22] Shaju, K.S.; Thomas, K.J.; Raphael, V.P.; Paul, A.: Synergistic Effect of KI on Corrosion Inhibition of Mild Steel by Polynuclear Schiff Base in Sulphuric Acid, *ISRN Corrosion*, 2012, **2012**, 1–8 DOI: [10.5402/2012/425878](https://doi.org/10.5402/2012/425878)
- [23] Roy, P.; Pal, A.; Sukul, D.: Origin of the synergistic effect between polysaccharide and thiourea towards adsorption and corrosion inhibition for mild steel in sulphuric acid, *RSC Adv.*, 2014, **4**(21), 10607–10613 DOI: [10.1039/c3ra46549g](https://doi.org/10.1039/c3ra46549g)
- [24] Hazazi, O.A.; Fawzy, A.; Awad, M.: Synergistic Effect of Halides on the Corrosion Inhibition of Mild Steel in H₂SO₄ by a Triazole Derivative: Kinetics and Thermodynamic Studies, *Int. J. Electrochem. Sci.*, 2014, **9**, 4086–4103 <http://electrochemsci.org>
- [25] Borghi, G.; Ferretti, A.; Nguyen, N.L.; Dabo, I.; Marzari, N.: Koopmans-compliant Functionals and Their Performance Against Reference Molecular Data, *Phys. Rev. B*, 2014, **90**(7), 075135 DOI: [10.1103/physrevb.90.075135](https://doi.org/10.1103/physrevb.90.075135)
- [26] Pearson, R.: Absolute electronegativity and hardness: application to inorganic chemistry. *Inorg. Chem.*, 1988, **27**(4), 734–740 DOI: [10.1021/ic00277a030](https://doi.org/10.1021/ic00277a030)
- [27] Benhadria, N.; Messaoudi, B.; Attar, T.: The Study of the Correlation between the Detection Limit and the Energy Stability of Two Antimony Complexes by Means of Conceptual DFT, *Malaysian Journal of Chemistry*, 2020, **22**(2), 111–120 <https://ikm.org.my/ojs/index.php/MJChem/article/view/609>
- [28] Yuan, S.; Liang, B.; Zhao, Y.; Pehkonen, S.: Surface chemistry and corrosion behaviour of 304 stainless steel in simulated seawater containing inorganic sulphide and sulphate-reducing bacteria, *Corros. Sci.*, 2013, **74**, 353–366 DOI: [10.1016/j.corsci.2013.04.058](https://doi.org/10.1016/j.corsci.2013.04.058)
- [29] Chygyrynets, E.; Vorobyova, V.A.: Study of rapeseed extract as eco-friendly vapor phase corrosion inhibitor, *Chem. Chem. Technol.*, 2014, **8**(2), 235–242 DOI: [10.23939/chcht08.02.235](https://doi.org/10.23939/chcht08.02.235)
- [30] Eddy, N.O.; Ita, B.I.: QSAR, DFT and quantum chemical studies on the inhibition potentials of some carbozones for the corrosion of mild steel in HCl, *J. Mol. Model.*, 2011, **17**(2), 359–376 DOI: [10.1007/s00894-010-0731-7](https://doi.org/10.1007/s00894-010-0731-7)
- [31] Attar, T.; Messaoudi, B.; Benhadria, N.: DFT Theoretical Study of Some Thiosemicarbazide Derivatives with Copper, *Chem. Chem. Technol.*, 2020, **14**(1), 20–25 DOI: [10.23939/chcht14.01.020](https://doi.org/10.23939/chcht14.01.020)
- [32] Benhadria, N.; Attar, T.; Messaoudi, B.: Understanding the Link Between the Detection Limit and the Energy Stability of Two Quercetin–Antimony Complexes by Means of Conceptual DFT, *S. Afr. J. Chem.*, 2020, **73**(1), 120–124 DOI: [10.17159/0379-4350/2020/v73a17](https://doi.org/10.17159/0379-4350/2020/v73a17)
- [33] Musa, A.Y.; Kadhum, A.A.H.; Mohamed, A.B.; Takriff, M.S.: Molecular dynamics and quantum

- chemical calculation studies on 4,4-dimethyl-3-thiosemicarbazide as corrosion inhibitor in 2.5M H₂SO₄, *Mater. Chem. Phys.*, 2011, **129**(1-2), 660–665 DOI: [10.1016/j.matchemphys.2011.05.010](https://doi.org/10.1016/j.matchemphys.2011.05.010)
- [34] Alaoui, K.; El Kacimi, Y.; Galai, M.: New triazepine carboxylate derivatives: correlation between corrosion inhibition property and chemical structure, *Int. J. Ind. Chem.*, 2020, **11**(1), 23–42 DOI: [10.1007/s40090-019-00199-5](https://doi.org/10.1007/s40090-019-00199-5)
- [35] Popoola, L.T.: Organic green corrosion inhibitors (OGCIs): a critical review, *Corros. Rev.*, 2019, **37**(2), 71–102 DOI: [10.1515/corrrev-2018-0058](https://doi.org/10.1515/corrrev-2018-0058)
- [36] Abd-El-Naby, B.A.; Abdullatef, O.A.; El-Kshlan, H.M.; Khamisd, E.; Abd-El-Fatah, M.A.: Anionic Effect on the Acidic Corrosion of Aluminum and its Inhibition by Lupine Extract, *Port. Electrochim. Acta*, 2015, **33**(5), 265–274 DOI: [10.4152/pea.201505265](https://doi.org/10.4152/pea.201505265)
- [37] Singh, A.; Singh, A.K.; Quraishi, M.A.: A novel corrosion inhibitor for mild steel in acid media, *Open. Electrochem. J.*, 2010, **2**, 43–51 DOI: [10.2174/1876505X01002010043](https://doi.org/10.2174/1876505X01002010043)
- [38] Chakravarthy, M.P.; Mohana, K.N.: Adsorption and Corrosion Inhibition Characteristics of Some Nicotinamide Derivatives on Mild Steel in Hydrochloric Acid Solution, *Int. Sch. Res.*, 2014, **2014**, 1–13 DOI: [10.1155/2014/687276](https://doi.org/10.1155/2014/687276)
- [39] Oguzie, E.E.: Studies on the inhibitive effect of *Ocimumviridis* extract on the acid corrosion of mild steel, *Mater. Chem. Phys.*, 2006, **99**(2-3), 441–446 DOI: [10.1016/j.matchemphys.2005.11.018](https://doi.org/10.1016/j.matchemphys.2005.11.018)
- [40] Eddy, N.O.; Odoemelam, S.A.; Odiongenyi, A.O.: Inhibitive, adsorption and synergistic studies on ethanol extract of *Gnetum africana* as green corrosion inhibitor for mild steel in H₂SO₄, *Green. Chem. Lett. Rev.*, 2009, **2**(2), 111–119 DOI: [10.1080/17518250903170868](https://doi.org/10.1080/17518250903170868)
- [41] Chakravarthy, M.P.; Mohana, K.N.; Pradeep Kumar, C.B.: Corrosion inhibition effect and adsorption behaviour of nicotinamide derivatives on mild steel in hydrochloric acid solution, *Int. J. Ind. Chem.*, 2014, **5**(2), 1–21 DOI: [10.1007/s40090-014-0019-3](https://doi.org/10.1007/s40090-014-0019-3)
- [42] Benchadli, A.; Attar, T.; Choukchou-Braham, E.: Inhibition of Carbon Steel Corrosion in Perchloric Acid Solution by Povidone Iodine, *Phys. Chem. Res.*, 2019, **7**(4), 837–848 DOI: [10.22036/PCR.2019.198787.1665](https://doi.org/10.22036/PCR.2019.198787.1665)
- [43] Umoren, S.A.; Obot, I.B.; Ebenso, E.E.: Corrosion Inhibition of Aluminium Using Exudate Gum from *Pachylobus edulis* in the Presence of Halide Ions in HCl, *Eur. J. Chem.*, 2008, **5**, 355–364 DOI: [10.1155/2008/138407](https://doi.org/10.1155/2008/138407)
- [44] Faustin, M.; Maciuk, A.; Salvin, P.; Roos, C.; Lebrini, M.: Corrosion inhibition of C38 steel by alkaloids extract of *Geissospermum laeve* in 1M hydrochloric acid: Electrochemical and phytochemical studies, *Corros. Sci.*, 2015, **92**, 287–300 DOI: [10.1016/j.corsci.2014.12.005](https://doi.org/10.1016/j.corsci.2014.12.005)
- [45] Fawzy, A.; Abdallah, M.; Zaaferany, I.A.; Ahmed, S.A.; Althagafi, I.I.: Thermodynamic, kinetic and mechanistic approach to the corrosion inhibition of carbon steel by new synthesized amino acids-based surfactants as green inhibitors in neutral and alkaline aqueous media, *J. Mol. Liq.*, 2018, **265**(1), 276–291 DOI: [10.1016/j.molliq.2018.05.140](https://doi.org/10.1016/j.molliq.2018.05.140)
- [46] Umoren, S.A.; Obot, I.B.; Ebenso, E.E.; Obi-Egbed, N.O.: Synergistic Inhibition between Naturally Occurring Exudate Gum and Halide Ions on the Corrosion of Mild Steel in Acidic Medium, *Int. J. Electrochem. Sci.*, 2008, **3**(9), 1029–1043 <http://citeseerx.ist.psu.edu>
- [47] Attar, T.; Larabi, L.; Harek, Y.: Corrosion inhibition of cold rolled steel in 0.5 M H₂SO₄ by potassium iodide, *Der Pharma Chemica*, 2014, **6**(4), 181–186 <https://www.derpharmachemica.com>
- [48] Benchadli, A.; Attar, T.; Choukchou-Braham, E.: Corrosion inhibition of carbon steel (XC 38) in hydrochloric acid by potassium iodide, *Journal of Advanced Research in Science and Technology*, 2018, **5**(2), 834–844 <https://www.asjp.cerist.dz>
- [49] Doner, A.; Solmaz, R.; Ozcan, M.; Kardas, G.: Experimental and Theoretical Studies of Thiazoles as Corrosion Inhibitors for Mild Steel in Sulphuric Acid Solution, *Corros. Sci.*, 2011, **53**(9), 2902–2913 DOI: [10.1016/j.corsci.2011.05.027](https://doi.org/10.1016/j.corsci.2011.05.027)
- [50] Solmaz, R.: Investigation of corrosion inhibition mechanism and stability of Vitamin B1 on mild steel in 0.5M HCl solution, *Corros. Sci.*, 2014, **81**, 75–84 DOI: [10.1016/j.corsci.2013.12.006](https://doi.org/10.1016/j.corsci.2013.12.006)
- [51] Lukovits, I.; Kalman, E.; Zucchi, F.: Corrosion Inhibitors–Correlation between Electronic Structure and Efficiency, *Corrosion*, 2001, **57**(1), 3–9 DOI: [10.5006/1.3290328](https://doi.org/10.5006/1.3290328)
- [52] Ramya, K.; Mohan, R.; Joseph, A.: Adsorption and electrochemical studies on the synergistic interaction of alkyl benzimidazoles and ethylene thiourea pair on mild steel in hydrochloric acid, *J. Taiwan. Inst. Chem. Eng.*, 2014, **45**(6), 3021–3032 DOI: [10.1016/j.jtice.2014.08.033](https://doi.org/10.1016/j.jtice.2014.08.033)
- [53] Bentiss, F.; Jama, C.; Mernari, B.: Corrosion control of mild steel using 3,5-bis(4-methoxyphenyl)-4-amino-1,2,4-triazole in normal hydrochloric acid medium, *Corros. Sci.*, 2009, **51**(8), 1628–1635 DOI: [10.1016/j.corsci.2009.04.009](https://doi.org/10.1016/j.corsci.2009.04.009)

MODELLING OF THE PYROLYSIS ZONE OF A DOWNDRAFT GASIFICATION REACTOR

MÁRTA KÁKONYI*¹, ÁGNES BÁRKÁNYI¹, TIBOR CHOVÁN¹, AND SÁNDOR NÉMETH¹

¹Research Centre for Biochemical, Environmental and Chemical Engineering, University of Pannonia, Egyetem u. 10, Veszprém, 8200, HUNGARY

The increasing amount of municipal solid waste (MSW) is a growing challenge that current waste-treatment practices are having to face. Therefore, technologies that can prevent waste from ending up in landfill sites have come to the fore. One of the technologies that produces a valuable product from waste, namely synthesis gas, is gasification. The raw material of this technology is the so-called Refuse-Derived Fuel, which is made from MSW. Three separate zones are located in downdraft gasification reactors: the pyrolysis, oxidation and reduction zones. This work is concerned with the determination of kinetic parameters in the pyrolysis zone. It also discusses the estimation of the product composition of this zone, which defines the raw material of the following zone.

Keywords: gasification, modelling, waste, Refuse-Derived Fuel

1. Introduction

Management of the increasing quantity of municipal solid waste (MSW) is an ongoing issue. The majority of the waste ends up in landfill sites or is incinerated, leading to the emission of significant amounts of greenhouse gases. According to data from the European Union's Eurostat database [1], the EU27 countries produce in excess of 200 million tons of waste. The amount disposed of is continuously being reduced by separating recyclable and biodegradable materials. Although less and less waste is being dumped as landfill, landfill sites cannot accommodate waste being generated. Therefore, the quantity of waste ending up in landfill sites is not reducing significantly. In 2019 the EU member states deposited 24 mass % of waste in landfill sites; that quantity was 53 million tons. In Hungary, this value was 51 mass %, namely 1.9 million tons (Fig. 1).

As the waste deposited in landfill sites decomposes, methane is formed and released into the atmosphere as a result of a reduction in its volume through cracks in the soil layer used to cover the landfill. The global warming potential of methane (CH₄) is 25 times greater than that of carbon dioxide (CO₂) [2]. Therefore, the development of technologies that can prevent waste from ending up in landfill sites and further reduce greenhouse gas emissions through Carbon Capture, Utilization and Storage is justified. One such technology is gasification.

Different types of gasification reactors are available, namely moving bed, fluidized-bed, entrained-flow, rotary

*Correspondence: kakonyi.marta@mk.uni-pannon.hu

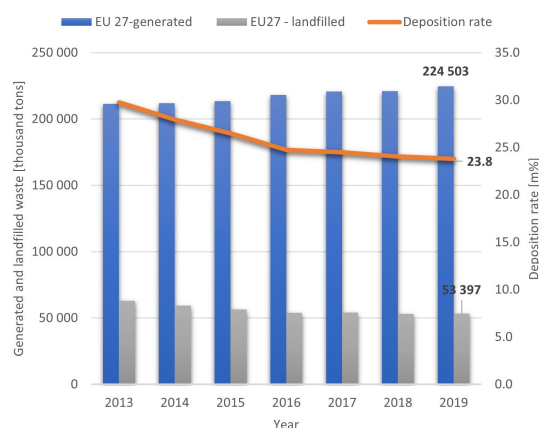


Figure 1: Generation of municipal solid waste and the amount deposited as landfill [1].

kiln and plasma gasifiers, which have been reviewed in Ref.[3,4]. Updraft and downdraft reactors are moving bed gasifiers. In the case of the former, the product gas travels in the opposite direction to the feedstock and leaves through the top of the reactor. Since the amount of tar contained in the product gas is higher than in the case of downdraft reactors, where the gas and feedstock flow in the same direction, the temperature of the effluent gas is higher. In fluidized-bed gasifiers, a bed material is used for the purpose of heat transfer and the raw material, which is fed into the reactor from the bottom, as well as the bed material are fluidized by air. The product gas contains a higher proportion of particles. The raw material of entrained-flow reactors is powdered, it along with

air is fed into the reactor from the top. Rotary kiln gasifiers rotate around their axes to ensure the solid and gas phases mixture. Plasma reactors use copper or carbon electrodes and the raw material is decomposed down to the atomic level. Downdraft reactors are the most suitable for low tar content with high carbon conversion, as well as high hydrogen (H₂) and carbon monoxide (CO) content of the product. Its operating temperature and residence time meet the requirements of waste, namely its investment and operating costs are low.

The feedstock of downdraft reactors is fed from above while the air feed enters through the side of the reactor at a height slightly higher than halfway up the gasifier and is evenly distributed inside. Therefore, three separate zones can be formed. At the top, in an oxygen-deficient environment, is the pyrolysis zone, before air is introduced and the raw material partially burned in the oxidation zone to meet the energy demand of the endothermic reactions that take place in the other two zones. By proceeding along the length of the reactor, the reduction processes occur in the reduction zone after passing through the oxidation zone. Once the gas has passed through the reduction zone, it is extracted and the slag falls to the bottom of the reactor.

The aim of this work is to create a simple model that estimates the amount of gaseous components in the pyrolysis zone as a function of temperature based on the composition of the raw material and the amounts of the gases. Furthermore, such a model can be integrated into a model of a more complex gasification reactor. To calculate the amounts of the gases, the kinetic parameters of the pyrolysis zone are required, which were identified. The output of this zone is the raw material for the following oxidation zone.

2. Identification of pyrolysis kinetic parameters

Various models using mainly biomass and cellulose feedstocks have been developed over the years to describe the pyrolysis zone. Some of them are suitable for molecular level studies, others are designed for particle-level studies and some are also applied to study equipment. Hameed et al. have compiled a detailed overview of them [5]. Since the pyrolysis zone is only one component of the reactor model, the less complex model referred to as the one-step kinetic model was chosen, which is written for the mass conversion as [6]

$$\frac{dm}{dt} = -k m (1 - y). \quad (1)$$

Here, y is the conversion factor calculated by using the mass of raw material (m_{in}), current mass (m_{actual}), and the mass of the solid residue (m_{final}) as [7]

$$y = \frac{m_{\text{in}} - m_{\text{actual}}}{m_{\text{in}} - m_{\text{final}}}. \quad (2)$$

The rate constant of the reaction, k , is defined by the Arrhenius equation

$$k = A e^{\frac{-E_a}{RT}}, \quad (3)$$

from which the unknown parameters A and E_a/R can be determined. The amount of gas can be calculated from Eq. 1.

The parameters for cellulose and lignin (a mixture of paper, cardboard and wood)—hereinafter referred to as cellulose, plastic (a mixture of PE, PP and PET) as well as a 50 – 50 m% blend of cellulose and plastic were identified separately. The kinetic parameters (A and E_a/R) of both kinds of raw materials were unknown. Since the search space was smaller when identifying the parameters of pure raw materials, faster and more accurate results were achieved. The parameters were determined using the MATLAB R2019b program based on experimental data from the literature [8]. The effect of a catalyst on the decomposition of waste was investigated by thermogravimetry and mass spectrometry in a mass spectrometer. The inert atmosphere was composed of argon, while the masses of the samples were between 0.5 and 4 mg. Results in the absence of a catalyst are studied in this work. The heating rate of measurements was 20 °C/min. The degradation of cellulose started at approximately 250 °C, while that of plastic commenced at around 400 °C (Fig. 2).

In order to focus on the portion of the curves where the changes in mass were larger as well as the measured and calculated values deviated more, the temperature range was narrowed from 60 – 700 °C to 142 – 552 °C for cellulose and to 369 – 531 °C for plastic. The $m\%$ of the residue was read from the graph. A global extrema searcher, NOMAD, was used in MATLAB to identify the parameters. The differential equation (Eq. 1) was solved using ode23s. The objective function to be minimized was the sum of the squares of the difference between the measured and calculated data for each temperature value:

$$\min(f) = \sum_T (m\%_{\text{measured}} - m\%_{\text{calculated}})^2. \quad (4)$$

The identified parameters are shown in Table 1.

Once the kinetic parameters of the pure fractions had been identified, the mixture was calculated using these values. The change in total weight is the sum of the change in weight of the cellulose (m_c) and plastic (m_p) (Eq. 5). Furthermore, the y -factor (Eq. 2), the kinetic rate of the reaction (Eq. 3) and the mass conversion (Eq. 1)

Table 1: Identified parameters

	$\ln(A)$	E_a/R [K]	Correlation coefficient
Cellulose	16.83	13 540	0.915
Plastic	55.3	43 502	0.765

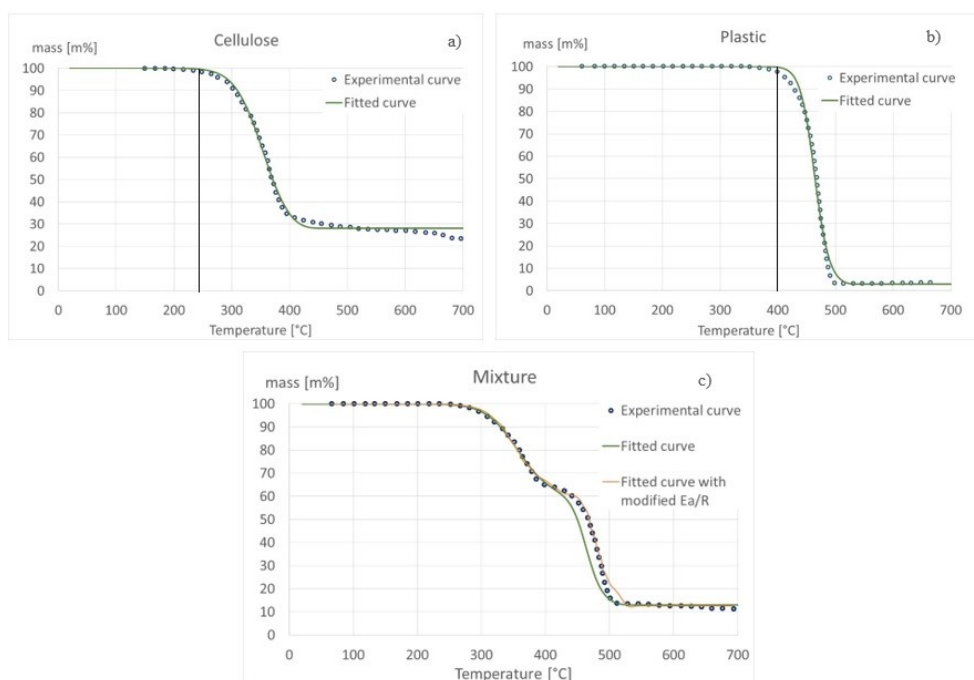


Figure 2: Measured [8] and simulated results using the identified parameters: a) cellulose, b) plastic, c) cellulose and plastic 50 – 50% mixture; \circ Experimental curve, — Fitted curve, — Fitted curve with modified E_a/R , — degradation start

were calculated separately for both components:

$$\frac{dm}{dt} = \frac{dm_c}{dt} + \frac{dm_p}{dt} \quad (5)$$

The results of the calculation using the applied model are shown in Fig. 2. The simulated decomposition curves of plastic (Fig. 2a) and cellulose (Fig. 2b) follow the experimental results well; the end of the curve deviates to a small extent caused by the decomposition of the lignin [9]. In the case of the mixture (Fig. 2c), a higher deviation in excess of 400 °C was observed. The decomposition of the cellulose commenced earlier at 250 °C, while that of the plastic started at 400 °C. The degradation of the plastic component started later. Although lignin begins to degrade at 400 °C, which may affect the decomposition of plastic [8,9], the difference was not significant, so the degradation of the lignin was not treated separately from that of the cellulose.

Since the component of the Arrhenius equation corresponding to the activation energy depends on the temperature, the E_a/R value had to be modified. From the Arrhenius equation (Eq. 3), the value of k was calculated along with the parameters before the kinetic parameters were recalculated by retaining the k value. The parameter E_a/R of plastic changed, its new value was 44 500 K, the values of the other parameters remained unchanged as is presented in Table 1. Using this new E_a/R number, the recalculated curve (depicted in orange) fitted better. Based on the one-step kinetic model, the mass of gas formed in the pyrolysis zone can be calculated. The disadvantage of this model is that it cannot determine the composition of the gas nor the quantities of its components. In the oxidation zone, since the products from the

pyrolysis zone are partially oxidized, it is also necessary to quantify each gaseous component.

3. Composition of the gas

Pyrolysis gas consists of different components; the main components are carbon monoxide (CO), hydrogen (H₂), carbon dioxide (CO₂), methane (CH₄), water (H₂O), and tar. The exact molecular formula of tar is unknown, its formula is represented as C_aH_bO_c. An extrema search was used to determine its composition.

3.1 Composition of Refuse-Derived Fuel

Some waste-treatment plants include mechanical biological treatment plants that produce Refuse-Derived Fuel (RDF) by filtering out and grinding MSW. In such plants, glass, metal as well as inert and biodegradable materials are removed, MSW is dried whilst being grinded and finally 3 % of its original weight will be equal to the mass of the RDF. As the raw material of the reactor is RDF, the results of studies into the composition of RDF were collected and averaged Table 2. [10, 11]

3.2 Objective function and constraints

Based on the composition, the constraints required for the extrema search can be determined. The total masses (m_j) of each element, namely C, O, H, Cl, S, and N, were determined from Eq. 6. The mass of the impurities (m_{Cl} , m_S and m_N) was subtracted from the total gas mass (m_{gas}). The extrema finder searches for the minimum of the objective function, which is the absolute value of the

Table 2: Average RDF composition

Proximate analysis [m%]	
Moisture content	17.55
Ash	12.3
Volatile matter	63.18
Fixed carbon	6.97
Ultimate analysis of the dry basis [m%]	
C	40.83
H	5.36
O	37.08
N	1.18
S	0.29
Cl	0.34
Ash	14.92

difference between the total mass of the gas and the sum of the mass of each gaseous component according to Eq. 7, where n_i denotes the moles of gaseous compounds and M_i represents the molecular weight.

$$m_j = m_{\text{gas}} \frac{(m\%)_j}{100} \quad (6)$$

$$\min(f) = \text{abs} \left(m_{\text{gas}} - (m_{\text{Cl}} + m_{\text{S}} + m_{\text{N}}) - \sum_i M_i n_i \right) \quad (7)$$

The total weight of each element should be equal to the sum of the weight of the same element in each compound. Due to the strength of the constraints, only a minimal error is permissible. The nonlinear constraints are

$$0.01 \geq \frac{\text{abs} [m_{\text{C}} - M_{\text{C}}(n_{\text{CO}} + n_{\text{CH}_4} + n_{\text{CO}_2} + a n_{\text{tar}})]}{m_{\text{C}}} \quad (8)$$

$$0.01 \geq \frac{\text{abs} [m_{\text{O}} - M_{\text{O}}(n_{\text{CO}} + 2n_{\text{CO}_2} + n_{\text{H}_2\text{O}} + c n_{\text{tar}})]}{m_{\text{O}}} \quad (9)$$

$$0.01 \geq \frac{\text{abs} [m_{\text{H}} - M_{\text{H}}(4n_{\text{CH}_4} + 2n_{\text{H}_2\text{O}} + 2n_{\text{H}_2} + b n_{\text{tar}})]}{m_{\text{H}}} \quad (10)$$

The limits of the parameters a , b , and c are determined based on the measurement of the tar composition [12, 13]. The constraints of these parameters are

$$12 > a > 6; \quad 24 > b > 6; \quad 6 > c > 0 \quad (11)$$

Empirical relationships [14, 15] were applied to the mass ratios of CO to CO₂, and CH₄ to CO₂, which are temperature-dependent:

$$y_{\text{CO}/\text{CO}_2} = \exp \left(1.8447896 + \frac{7730313}{T} + \frac{5019898}{T} \right) \quad (12)$$

Table 3: Lower and upper limits

Limit	CO ₂	H ₂ O	H ₂	C _a H _b O _c	a	b	c
Lower [m%]	10	0	0.4	40	9	10	4
Upper [m%]	25	10	0.7	95	11	20	6

$$y_{\text{CH}_4/\text{CO}_2} = 5 \times 10^{-16} T^{5.06} \quad (13)$$

By measuring the composition of the pyrolysis gas [8, 16], the lower and upper limits were determined for the mass percent of components (Table 3). The $m\%$ limits were calculated from

$$0 \geq \frac{m\%_{\text{lower}}}{100} - \frac{n_i M_i}{m_{\text{gas}} - (m_{\text{Cl}} + m_{\text{S}} + m_{\text{N}})} \quad (14)$$

$$0 \geq \frac{n_i M_i}{m_{\text{gas}} - (m_{\text{Cl}} + m_{\text{S}} + m_{\text{N}})} - \frac{m\%_{\text{upper}}}{100} \quad (15)$$

Using the kinetic parameters identified in the previous section, the batch pyrolysis was simulated for 250 kg of raw material with a moisture content of 17.55 % as well as plastic and cellulose fractions of 50 – 50 %. During the process, the composition of the gas was calculated as a function of temperature based on the aforementioned equations. The heating rate which was used during identification was 20 °C/min. The dry raw material was taken into account in the calculation. To reduce the calculation time, the composition was estimated every 20 s so the total simulation time was 3600 s. In each step, the starting point of the extrema search was the result of the calculation during the previous step. The results of the simulation are shown in Fig. 3 and Table 4. Above 500 °C, the tar began to decompose and the amount of CO increased compared to that of CO₂.

4. Conclusions

The aim of this work was to develop a relatively simple model of the pyrolysis zone of a downdraft gasification reactor to estimate its kinetic parameters and based on these propose a methodology to determine the amount of gaseous components generated. The kinetic parameters of the pyrolysis zone were determined by an extrema finder and the calculated values fit well with the experimental results found in the literature. With the help of the proposed model, the kinetic parameters can be identified for any new raw material and heating rate. The method applied to determine the composition of gaseous components is suitable for estimating the quantity of components as a function of temperature based on the elemental composition of the raw material. The one-step kinetic model using a simple calculation of the gas composition can be easily applied to describe the pyrolysis zone of the RDF gasification reactor and even integrated into a more complex model of a gasification system because of the low computational capacity required.

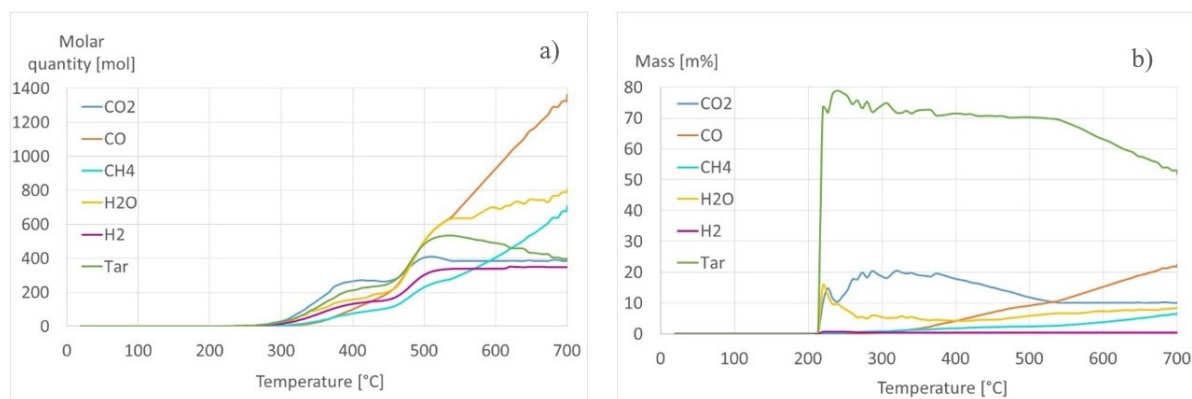


Figure 3: Evolution of molar quantity a) and weight percentage b) as a function of temperature

Table 4: Gas composition as a function of temperature

Temperature [°C]	200	300	400	500	600	700
Molar quantity [mol]						
CO ₂	0	29.2	266.1	406.5	386.5	390.2
CO	0	1.2	98.9	499.7	927.7	1361.5
CH ₄	0	3.6	74.7	229.9	404.6	707.1
H ₂ O	0	21.2	157	499.8	696.8	804.4
H ₂	0	14	132	304.2	340.3	349.6
Tar	0	23.6	211	483.1	489.8	387.1
<i>a</i>	0	9.1	9.2	9	9	9.5
<i>b</i>	0	17.3	18.2	17.3	17.3	18.2
<i>c</i>	0	5.6	5.9	6	5.9	6
Mass [m%]						
CO ₂	0	18.6	17.8	11.8	10	10.1
CO	0	0.5	4.2	9.2	15.3	22.4
CH ₄	0	0.8	1.8	2.4	3.8	6.7
H ₂ O	0	5.5	4.3	5.9	7.4	8.5
H ₂	0	0.4	0.4	0.4	0.4	0.4
Tar	0	74.2	71.5	70.3	63.1	51.9

5. Acknowledgements

This work was supported by the TKP2020-NKA-10 project financed under the 2020-4.1.1-TKP2020 Thematic Excellence Programme by the National Research, Development and Innovation Fund of Hungary.

REFERENCES

- [1] Eustat-Municipal Waste by Waste Management, Date of save: 2021. 04. 07. <https://ec.europa.eu/eurostat>
- [2] IPCC: Fourth Assessment Report, 2006
- [3] Molino, A.; Chianese, S.; Musmarra, D.: Biomass gasification technology: The state of the art overview, *J. Energy Chem.*, 2016, **25**(1), 10–25 DOI: [10.1016/j.jechem.2015.11.005](https://doi.org/10.1016/j.jechem.2015.11.005)
- [4] Kumar, A.; Jones, D.D.; Hanna, M.A.: Thermochemical biomass gasification: a review of the current status of the technology, *Energies*, 2009, **2**(3), 556–581 DOI: [10.3390/en20300556](https://doi.org/10.3390/en20300556)
- [5] Hameed, S.; Sharma, A.; Pareek, V.; Wu, H.; Yu, Y.: A review on biomass pyrolysis models: Kinetic, network and mechanistic models, *Biomass Bioenerg.*, 2019, **123**, 104–122 DOI: [10.1016/j.biombioe.2019.02.008](https://doi.org/10.1016/j.biombioe.2019.02.008)
- [6] Varhegyi, G.; Jakab, E.; Antal Jr, M.J.: Is the Broido-Shafizadeh model for cellulose pyrolysis true?, *Energy Fuels*, 1994, **8**(6), 1345–1352 DOI: [10.1021/ef00048a025](https://doi.org/10.1021/ef00048a025)
- [7] Faravelli, T.; Frassoldati, A.; Hemings, E.B.; Ranzi, E.: Multistep Kinetic Model of Biomass Pyrolysis, in *Cleaner Combustion*, 2013, 111–139, <http://link.springer.com>
- [8] Sebestyén, Z.; Barta-Rajnai, E.; Bozi, J.; Blazsó, M.; Jakab, E.; Miskolczi, N.; Sója, J.; Czégény, Z.: Thermo-catalytic pyrolysis of biomass and plastic mixtures using HZSM-5, *Appl. Energy*, 2017, **207**, 114–122 DOI: [10.1016/j.apenergy.2017.06.032](https://doi.org/10.1016/j.apenergy.2017.06.032)
- [9] Grammelis, P.; Basinas, P.; Malliopoulou, A.; Sakellariopoulos, G.: Pyrolysis kinetics and combustion characteristics of waste recovered fuels, *Fuel*, 2009, **88**(1), 195–205 DOI: [10.1016/j.fuel.2008.02.002](https://doi.org/10.1016/j.fuel.2008.02.002)
- [10] Vounatsos, P.; Atsonios, K.; Itskos, G.; Agraniotis, M.; Grammelis, P.; Kakaras, E.: Classification

- of refuse derived fuel (RDF) and model development of a novel thermal utilization concept through air-gasification, *Waste Biomass Valori.*, 2016, **7**(5), 1297–1308 DOI: [10.1007/s12649-016-9520-6](https://doi.org/10.1007/s12649-016-9520-6)
- [11] Phyllis2: The results of RDF composition studies were collected and averaged, Date of save 2020.12.11. <https://phyllis.nl>
- [12] Blanco, P.H.; Wu, C.; Onwudili, J.A.; Williams, P.T.: Characterization of tar from the pyrolysis/gasification of refuse derived fuel: influence of process parameters and catalysis, *Energy Fuels*, 2012, **26**(4), 2107–2115 DOI: [10.1021/ef300031j](https://doi.org/10.1021/ef300031j)
- [13] Ponzio, A.; Kalisz, S.; Blasiak, W.: Effect of operating conditions on tar and gas composition in high temperature air/steam gasification (HTAG) of plastic containing waste, *Fuel Process. Technol.*, 2006, **87**(3), 223–233 DOI: [10.1016/j.fuproc.2005.08.002](https://doi.org/10.1016/j.fuproc.2005.08.002)
- [14] Salem, A.M.; Paul, M.C.: An integrated kinetic model for downdraft gasifier based on a novel approach that optimises the reduction zone of gasifier, *Biomass Bioenerg.*, 2018, **109**, 172–181 DOI: [10.1016/j.biombioe.2017.12.030](https://doi.org/10.1016/j.biombioe.2017.12.030)
- [15] Sharma, A.K.: Modeling and simulation of a downdraft biomass gasifier 1. Model development and validation, *Energy Convers. Manag.*, 2011, **52**(2), 1386–1396 DOI: [10.1016/j.enconman.2010.10.001](https://doi.org/10.1016/j.enconman.2010.10.001)
- [16] Efika, E.C.; Onwudili, J.A.; Williams, P.T.: Products from the high temperature pyrolysis of RDF at slow and rapid heating rates, *J. Anal. Appl. Pyrolysis*, 2015, **112**, 14–22 DOI: [10.1016/j.jaap.2015.01.004](https://doi.org/10.1016/j.jaap.2015.01.004)

DAPHNIA MAGNA ACUTE IMMOBILIZATION TEST: AN OPPORTUNITY TO TEST THE ECOTOXICITY OF ALTERNATIVE FUELS

KATALIN ESZTER HUBAI*¹

¹Center for Natural Sciences, University of Pannonia, Egyetem u. 10, 8200 Veszprém, HUNGARY

The increasing need for environmental protection has led to the development of alternative biofuels. While the use of alternative fuels has significantly increased recently, only a few studies have addressed the problem of their ecotoxicity. The main aim of this work was to provide a short review of the *Daphnia magna* acute immobilization test, which has been the most commonly discussed in the literature.

Keywords: *Daphnia magna*, immobilization, ecotoxicology, alternative fuels

1. Introduction

Over recent decades, rapid population growth has been accompanied by a growth in the consumption of energy and use of transport fuels, which has caused irreversible environmental degradation and climate change [1]. Desires for a green environment have increased the demand for alternative fuels which in turn has necessitated researchers and industries to develop renewable alternative and cleaner energy sources worldwide [2].

Biofuels are energy-enriched substances manufactured from vegetable oils, recycled cooking grease and oil as well as animal fats through a chemical process known as transesterification, which is described below, to produce chemical compounds known as fatty acid methyl esters (FAME) [3, 4]. Biodiesel is the name given to these esters when they meet biodiesel standards such as the American ASTM D6751 or the European EN14214 for use as transport fuels [4]. Biodiesel is an eco-friendly form of fuel and may provide a solution to some problems associated with petroleum diesel [5].

Alternative fuels are key to improving the EU's security of energy supply, reducing the impact of transportation on the environment and boosting the EU's competitiveness. They are also an important building block for the EU's transition towards a low-carbon economy. In 2007, the production of biofuels in the EU reached 8,500 ktoe (kilotonnes of oil equivalent), while in 1996, this figure was less than 500 ktoe [6]. In 2010, 15.5% of power generation and 1.3% of energy consumption worldwide was attributed to renewable energy, while today, it is estimated that 86,000 kt per year of biofuels are produced, with the USA and Brazil being the primary producers [7].

More studies have shown that the use of biodiesel would reduce emissions of hydrocarbons, carbon monoxide and volatile organic compounds [8, 9]. However, the results of analyzing the biological effects related to the presence of biodiesel in the environment are ambiguous [10].

Although the use of alternative fuels has significantly increased recently, relatively few studies have addressed the problem of their ecotoxicity. Therefore, the main objective of this study is to provide a short overview of the *Daphnia magna* acute immobilization test which has been the most frequently discussed in the literature.

2. Methodology

2.1 Test organism

In addition to the chemical characterization of a substance, ecotoxicological tests provide an important tool for ecological risk assessments [11], giving a quantitative estimation of the overall toxic effect of the test organisms selected [12]. In general, the *Daphnia magna* acute immobilization test is amongst the most widely used ecotoxicological methods [13]. International standards apply such as OECD 202:2004 [14] or ISO 6341:1996.

The test organisms are the freshwater crustaceans *D. magna* and *D. pulex*. For the tests, neonates (newborn, freshly hatched juveniles) are used. (The main purpose of any standard protocol is to increase quality assurance which in turn might increase the credibility of the data produced [15]. In order to minimize any possible errors caused by improper maintenance of stock cultures, so-called Toxkits have been developed and marketed by MicroBioTests Inc. (Mariakerke-Gent, Belgium) [16]. The main benefits of using a Toxkit are that they are maintenance-free and user-friendly [17] test organisms

*Correspondence: hubai.katalin@mk.uni-pannon.hu



Figure 1: Freshly hatched *D. magna* neonate

whose genetic material is practically uniform and, prior to testing, juveniles of approximately the same age are reproduced (Fig. 1).

2.2 Implementation of experiments

There are several options for conducting alternative fuel toxicology studies. In one part of the research, the fuel was stirred in water before the test organisms were introduced into the test chamber [18–20]. In this method, the layer of oil on the top of the wells can cause some problems.

In other experiments, aqueous extracts were used, for example, a stock solution was made by adding seawater (depending on the test organism) to the sample and stirring the mixture for 10 – 24 h [21–23].

Three different biodiesels, that is, two based on the vegetable oils produced by canola and soybean as well as waste frying oil that originated from animals, were used by Hollebene et al. [24]. Oil-in-water dispersions (OWD) and water-accommodated fractions (WAF) were used for the *Daphnia magna* assay. Different results were observed during the tests; higher LC50 values were measured in WAFs compared to in OWDs. This suggests that the soluble fraction is of lower toxicity compared to the physical danger of the organisms being smothered by the oily fuel (See Table 1).

Müller et al. [23] assessed the toxicity of the water-soluble fraction (WSF) of biodiesel on *D. magna* in comparison to the WSF of diesel [24]. The tested sample of biodiesel was a fatty acid methyl ester (FAME) mainly produced by soybean oil (95%). This biodiesel did not elucidate a measurable degree of toxicity either following acute or chronic exposure. On the other hand, in a study by Eck-Varanka et al. [21], the ecotoxicity of a rapeseed biodiesel was profiled using a battery of test organisms and *D. magna* exhibited an extremely high degree of toxicity, being the most sensitive assay in the battery.

Khan et al. [18] carried out an extensive study to compare the ecotoxicity of diesel, neat biodiesel (B100) and blends of both (B50, B20 and B5). B100 was produced from recycled cooking oils and fats. The lowest and highest levels of ecotoxicity were exhibited by B100 and diesel, respectively, while the ecotoxicity of the blends, expressed both in terms of mortality rates and EC50 values, were in the intermediate range. However, the differences between the measured responses were quite small: the LC50 values of *Daphnia magna* in neat biodiesel and diesel were 4.65 and 1.78 ppm, respectively. Tjartinto et al. (2014) conducted a similar study on biodiesel produced from waste vegetable oil and reported an EC50 value of 3.157 ppm for *Daphnia magna* [25].

Heger et al. [26] compared the ecotoxicity of two biofuel candidates (1-octanol and 2-butanone) and found that 1-octanol exhibited a significant level of ecotoxicity on *D. magna* while 2-butanone did not. However, assays conducted on other test organisms revealed that the metabolites of the tested products could pose a higher risk of toxicity. Heger et al. [27] applied the *D. magna* acute immobilization test to compare the aquatic toxicity of the two biofuel candidates, namely 2-methyltetrahydrofuran (2-MTHF) and 2-methylfuran (2-MF), and found that the latter induced a significantly higher mortality rate than 2-MTHF (See Table 1).

Ecotoxicity, more precisely the ecotoxicity impact, is also included in the life cycle assessments (LCA) of alternative fuels [28]. Since LCAs follow the whole production line of a product, Bunzel et al. [29] used a *D. magna* assay to evaluate pesticide runoff from agricultural fields used for the cultivation of energy crops.

Khan et al. [18] stressed that one possible major purpose of ecotoxicity testing is assessing the potential risk of fuel spills in aquatic ecosystems. As such, it should be emphasized that *Daphnia magna*, being a freshwater taxon, cannot represent marine ecosystems, instead marine surrogates are used such as the brine shrimp *Artemia salina* [30].

Gateau et al. [31] investigated water-soluble fractions (WSFs) of four different vegetable oil methyl esters. Lower EC50 values (> 1000 mg/L) were calculated for vegetable oil methyl esters than for regular diesel ($EC50 < 100$ mg/L) (See Table 1).

The toxicity of biodiesel blends and crude oils have been investigated in other studies and biodiesel has been found to be less toxic to *D. magna* than both the biodiesel blends and crude oil (See Table 1).

3. Conclusion

In conclusion, it should be emphasized that the number of available studies is surprisingly low. Furthermore, these studies are extremely difficult to compare due to the following reasons: since the studies have been conducted on alternative fuels of very different origins, more extensive research on their chemical compositions to determine potential toxic effects is required. By taking into consid-

Table 1: Results of the *Daphnia magna* acute immobilization test (WAF: water-accommodated fraction; OWD: oil-in-water dispersion)

Fuel type	Method	LC50	Reference
1- octanol	WAF; Methods of acute toxicity testing using fish, macroinvertebrates and amphibians (US EPA)	520 mg/L	LeBlanc, 1980 [32]
1- octanol	OWD; Section 5, para. 1 "No. 3 of the Regulation on Application Documents and Evidence under the Chemicals Act" (Federal Environmental Agency)	26 mg/L	Kühn et al., 1989 [33]
Rapeseed oil Methyl Esters (RME)	WAF; OECD 202	> 1000 WAF mg/ml	Gateau et al., 2005 [31]
Erucic Rapeseed oil Methyl Esters (ERME)		> 1000 WAF mg/ml	
Sunflower oil Methyl Esters (SME)		> 1000 WAF mg/ml	
High Oleic Sunflower oil Methyl Esters (HOSME)		> 1000 WAF mg/ml	
Diesel fuel		< 100 WAF mg/ml	
based on vegetable oil produced from canola	OWD; Environment Canada test method "Biological Test Method: Acute Lethality Test Using <i>Daphnia</i> spp"	280 (200-410) mg/L	Hollebone et al., 2008 [24]
based on vegetable oil produced from soil crops		37.8 (23.0-63.1) mg/L	
based on waste frying oil produced from animals		582 (316-1080) mg/L	
Ultra-Low sulphur diesel		15.2 (8.2-29.3) mg/L	
Low sulphur diesel		17.9 (12.7-25.3) mg/L	
based on vegetable oil produced from canola	WAF (25 g/L fuel (1:40, fuel:water); Environment Canada test method "Biological Test Method: Acute Lethality Test Using <i>Daphnia</i> spp"	24650 (2500-140000) mg/L	
based on vegetable oil produced from soil crops		7500 (5100-11000) mg/L	
based on waste frying oil produced from animals		7500 (5100-11000) mg/L	
Ultra-low sulphur diesel		3300 (1800-5800) mg/L	
Low sulphur diesel		>25000 mg/L	
biodiesel (fatty acid methyl ester)	WAF; OECD 202	0.0226% (100% was 1:1 water:biodiesel)	Eck-Varanka et al., 2018 [21]
2-butanone (methyl ethyl ketone)	OWD; OECD 202	2152.1±44.6 mg/L	Heger et al., 2018 [26]
2-methyltetrahydrofuran (2-MTHF)	OWD; OECD 202	1.116±0.102 mg/L	Heger et al., 2018 [27]
2-methylfuran (2-MF)		0.032±0.004 mg/L	

eration the practical aspects of the tests, different periods of exposure have been employed (chronic exposures of 24, 48 and even 96 h). Sample preparation protocols also differ: oil-in-water dispersions (OWD) and water-accommodated fractions (WAF) have also been used as alternatives [34].

Generally, the *Daphnia magna* acute immobilization tests show an appropriate degree of sensitivity to a wide variety of compounds or complex mixtures [35–37]. However, as different components of an ecosystem will exhibit taxon-specific sensitivity to a chemical, a carefully composed battery of biotests should be used to gain a more comprehensive understanding [38]. It is possible that these tests will represent different functional and/or taxonomic groups as the ecotoxicity of pollutants influences the function and structure of aquatic or terrestrial ecosystems [39], moreover, possible endpoints will differ [40]. The minimum battery should involve the luminescent bacteria test, algae and zooplanktonic crustaceans [41].

Acknowledgments

This study was funded by the NTP-NFTÖ-19-B-0148 project.

REFERENCES

- [1] Darda, S.; Papalas, T.; Zabaniotou, A.: Biofuels journey in Europe: Currently the way to low carbon economy sustainability is still a challenge, *J. Clean. Prod.*, 2019, **208**, 575–588 DOI: [10.1016/j.jclepro.2018.10.147](https://doi.org/10.1016/j.jclepro.2018.10.147)
- [2] Shote, A.S.: Biofuel: An environmental friendly fuel, in *Anaerobic Digestion*, Eds.: Banu, J.R. (Intech Open, London, England), 2019. DOI: [10.5772/intechopen.82856](https://doi.org/10.5772/intechopen.82856)
- [3] Alleman, T.L.; McCormick, R.L.: Biodiesel handling and use guide, Fifth Edition (U.S. Department of Energy), 2016, DOE/GO-102016-4875
- [4] Milbrandt, A.; Kinchin, C.; McCormick, R.: The feasibility of producing and using biomass-based diesel and jet fuel in the United States, Technical Report NREL/TP-6A20-58015, 2013. DOI: [10.2172/1260324](https://doi.org/10.2172/1260324)
- [5] Aransiola, E.F.; Ehinmitola, E.O.; Adebimpe, A.I.; Shittu, T.D.; Solomon, B.O.: Prospects of biodiesel feedstock as an effective ecofuel source and their challenges, in *Woodhead Publishing Series in Energy, Advances in Eco-Fuels for a Sustainable Environment*, Eds.: Azad, K. (Woodhead Publishing, Sawston, England), 2019. ISBN: 978-0-081-02728-8
- [6] European Commission (2014): Report on the Assessment of the Member States National Policy Frameworks for the development of the market as regards alternative fuels in the transport sector and the deployment of the relevant infrastructure pursuant to Article 10 (2) of Directive 2014/94/EU, <https://ec.europa.eu>
- [7] Rastogi, M.; Shrivastava, S.: Recent advances in second generation bioethanol production: An insight to pretreatment, saccharification and fermentation processes, *Renew. Sust. Energ. Rev.*, 2017, **80**, 330–340 DOI: [10.1016/j.rser.2017.05.225](https://doi.org/10.1016/j.rser.2017.05.225)
- [8] Makareviciene, V.; Janulis, P.: Environmental effect of rapeseed oil ethyl ester, *Renew. Energy*, 2003, **28**(15), 2395–2403 DOI: [10.1016/S0960-1481\(03\)00142-3](https://doi.org/10.1016/S0960-1481(03)00142-3)
- [9] Bamgbose, I. A.; Anderson, T.A.: Phytotoxicity of three plant-based biodiesels, unmodified castor oil, and Diesel fuel to alfalfa (*Medicago sativa L.*), lettuce (*Lactuca sativa L.*), radish (*Raphanus sativus*), and wheatgrass (*Triticum aestivum*), *Ecotoxicol. Environ. Saf.*, 2015, **122**, 268–274 DOI: [10.1016/j.ecoenv.2015.08.003](https://doi.org/10.1016/j.ecoenv.2015.08.003)
- [10] Hawrot-Paw, M.; Izwikow, M.: Ecotoxicological effects of biodiesel in the soil, *J. Ecol. Eng.*, 2015, **16**(5), 34–39 DOI: [10.12911/22998993/60451](https://doi.org/10.12911/22998993/60451)
- [11] Klimkowicz-Pawlas, A.; Maliszewska-Kordybach, B.; Smreczak, B.: Triad-based screening risk assessment of the agricultural area exposed to the long-term PAHs contamination, *Environ. Geochem. Health*, 2019, **41**(3), 1369–1385 DOI: [10.1007/s10653-018-0220-y](https://doi.org/10.1007/s10653-018-0220-y)
- [12] Kessler, N.; Schauer, J.J.; Yagur-Kroll, S.; Melamed, S.; Tirosh, O.; Belkin, S.; Erel, Y.: A bacterial bioreporter panel to assay the cytotoxicity of atmospheric particulate matter, *Atmos. Environ.*, 2012, **63**, 94–101 DOI: [10.1016/j.atmosenv.2012.09.048](https://doi.org/10.1016/j.atmosenv.2012.09.048)
- [13] Allan, I.J.; Vrana, B.; Greenwood, R.; Mills, G.A.; Roig, B.; Gonzalez, C.A.: A “toolbox” for biological and chemical monitoring requirements for the European Union’s Water Framework Directive, *Talanta*, 2006, **69**(2), 302–322 DOI: [10.1016/j.talanta.2005.09.043](https://doi.org/10.1016/j.talanta.2005.09.043)
- [14] OECD/OCDE, 2004. OECD Guideline for Testing of Chemicals No. 202: *Daphnia sp.* Acute Immobilisation Test. ISSN: 20745761 OECD (2004), Test No. 202: *Daphnia sp.* Acute Immobilisation Test, in *OECD Guidelines for the Testing of Chemicals, Section 2*, (OECD Publishing, Paris) DOI: [10.1787/9789264069947-en](https://doi.org/10.1787/9789264069947-en)
- [15] Koeter, H.B.W.M.: Mutual acceptance of data: harmonised test methods and quality assurance of data - the process explained. *Toxicol. Lett.*, 2003, **140–141**, 11–20 DOI: [10.1016/S0378-4274\(02\)00491-5](https://doi.org/10.1016/S0378-4274(02)00491-5)
- [16] Persoone, G.; Baudo, R.; Cotman, M.; Blaise, C.; Thompson, K.Cl.; Moreira-Santos, M.; Vollat, B.; Törökne, A.; Han, T.: Review on the acute *Daphnia magna* toxicity test – Evaluation of the sensitivity and the precision of assays performed with organisms from laboratory cultures or hatched from dormant eggs, *Knowl. Managt. Aquatic Ecosyst.*, 2009, **393**, 01 DOI: [10.1051/kmae/2009012](https://doi.org/10.1051/kmae/2009012)
- [17] Kokkali, V.; van Delft, W.: Overview of commercially available bioassays for assessing chemical toxicity in aqueous samples. *Trends in Anal. Chem.*, 2014, **61**, 133–155 DOI: [10.1016/j.trac.2014.08.001](https://doi.org/10.1016/j.trac.2014.08.001)

- [18] Khan, N.; Warith, M.A.; Luk, G.: A comparison of acute toxicity of biodiesel, biodiesel blends, and diesel on aquatic organisms. *J. Air Waste Manag. Assoc.*, 2007, **57**(3), 286–296 DOI: [10.1080/10473289.2007.10465333](https://doi.org/10.1080/10473289.2007.10465333)
- [19] Bamgbose, I.A.; Anderson, T.A.: Assessment of three plant-based biodiesels using a *Daphnia magna* bioassay. *Environ. Sci. Pollut. Res.*, 2018, **25**(5), 4506–4515 DOI: [10.1007/s11356-017-0678-7](https://doi.org/10.1007/s11356-017-0678-7)
- [20] Pikula, K.S.; Zakharenko, A.M.; Chaika, V.V.; Stratidakis, A.K.; Kokkinakis, M.; Waissi, G.; Rakitskii, V.N.; Sarigiannis, D.A.; Hayes, A.W.; Coleman, M.D.; Tsatsakis, A.; Golokhvast, K.S.: Toxicity bioassay of waste cooking oil-based biodiesel on marine microalgae. *Toxicol. Rep.*, 2019, **6**, 111–117 DOI: [10.1016/j.toxrep.2018.12.007](https://doi.org/10.1016/j.toxrep.2018.12.007)
- [21] Eck-Varanka, B.; Kováts, N.; Horváth, E.; Ferincz, Á.; Kakasi, B.; Nagy, S.T.; Imre, K.; Paulovits, G.: Eco- and genotoxicity profiling of a rapeseed biodiesel using a battery of bioassays. *Ecotoxicol. Environ. Safety*, 2018, **151**, 170–177 DOI: [10.1016/j.ecoenv.2018.01.015](https://doi.org/10.1016/j.ecoenv.2018.01.015)
- [22] Leite, M.B.N.L.; de Araújo, M.M.S.; Nascimento, I.A.; da Cruz, A.C.S.; Pereira, S.A.; do Nascimento, N.C.: Toxicity of water-soluble fractions of biodiesel fuels derived from castor oil, palm oil, and waste cooking oil. *Environ. Toxicol. Chem.*, 2011, **30**(4), 893–897 DOI: [10.1002/etc.444](https://doi.org/10.1002/etc.444)
- [23] Müller, J.B.; Melegari, S.P.; Perreault, F.; Matias, W.G.: Comparative assessment of acute and chronic ecotoxicity of water soluble fractions of diesel and biodiesel on *Daphnia magna* and *Aliivibrio fischeri*. *Chemosphere*, 2019, **221**, 640–646 DOI: [10.1016/j.chemosphere.2019.01.069](https://doi.org/10.1016/j.chemosphere.2019.01.069)
- [24] Hollebhone, B.P.; Fieldhouse, B.; Landriault, M.; Doe, K.; Jackman, P.: Aqueous solubility, dispersibility and toxicity of biodiesels, in *International oil spill conference proceedings*, Savannah, USA, 2008. DOI: [10.7901/2169-3358-2008-1-929](https://doi.org/10.7901/2169-3358-2008-1-929)
- [25] Tjarinto, R.; Rachmatiah, I.; Salami, S.: Toxicity test of water-soluble fractions of waste vegetable oil-based biodiesel and biodiesel/diesel blends on *Daphnia magna* and *Allium cepa*. in: *Proceedings of the 3rd Applied Science for Technology Innovation*, ASTECHNOVA International Energy Conference, Yogyakarta, Indonesia, 2014, 294–301
- [26] Heger, S.; Du, M.; Bauer, K.; Schäffer, A.; Hollert, H.: Comparative ecotoxicity of potential biofuels to water flea (*Daphnia magna*), zebrafish (*Danio rerio*) and Chinese hamster (*Cricetulus griseus*) V79 cells. *Sci. Total Environ.*, 2018a, 631–632, 216–222 DOI: [10.1016/j.scitotenv.2018.03.028](https://doi.org/10.1016/j.scitotenv.2018.03.028)
- [27] Heger, S.; Bluhm, K.; Du, M.; Lehmann, G.; Anders, N.; Dechambrec, D.; Bardowc, A.; Schäffer, A.; Hollert, H.: Aquatic toxicity of biofuel candidates on *Daphnia magna*. *Ecotoxicol. Environ. Safety*, 2018b, **164**, 125–130 DOI: [10.1016/j.ecoenv.2018.08.008](https://doi.org/10.1016/j.ecoenv.2018.08.008)
- [28] Yang, Y.: Life cycle freshwater ecotoxicity, human health cancer, and noncancer impacts of corn ethanol and gasoline in the U.S., *J. Clean. Prod.*, 2013, **53**, 149–157 DOI: [10.1016/j.jclepro.2013.04.009](https://doi.org/10.1016/j.jclepro.2013.04.009)
- [29] Bunzel, K.; Schäfer, R.B.; Thrän, D.; Kattwinkel, M.: Pesticide runoff from energy crops: A threat to aquatic invertebrates? *Sci. Total Environ.*, 2015, **537**, 187–196 DOI: [10.1016/j.scitotenv.2015.08.011](https://doi.org/10.1016/j.scitotenv.2015.08.011)
- [30] Camargo, R.P.L.; Carrim, A.J.I.; Filho, N.R.A.: Study ecotoxicity of biodiesel from residual oils and fats and the effects of salinity aquatic ecosystems. *Ecotoxicol. Environ. Contam.*, 2017, **12**(1), 63–67 DOI: [10.5132/eec.2017.01.08](https://doi.org/10.5132/eec.2017.01.08)
- [31] Gateau, P.; van Dievoet, F.; Bouillon, V.; Vermeersch, G.; Claude, S.; Staat, F.: Environmentally friendly properties of vegetable oil methyl esters. *J. Am. Oil Chem. Soc.*, 2005, **12**(4), 308–313 DOI: [10.1051/oc1.2005.0308](https://doi.org/10.1051/oc1.2005.0308)
- [32] LeBlanc, G.A.: Acute toxicity of priority pollutants to water flea (*Daphnia magna*). *Bull. Environ. Contam. Toxicol.*, 1980, **24**(1), 684–691 DOI: [10.1007/bf01608174](https://doi.org/10.1007/bf01608174)
- [33] Kühn, R.; Pattard, M.; Pernak, K.D.; Winter, A.: Results of the harmful effects of selected water pollutants (anilines, phenols, aliphatic compounds) to *Daphnia magna*. *Water Res.*, 1989, **23**(4), 495–499 DOI: [10.1016/0043-1354\(89\)90141-3](https://doi.org/10.1016/0043-1354(89)90141-3)
- [34] Bluhm, K.; Heger, S.; Seiler, T.B.; Hallare, A.V.; Schaeffer, A.; Hollert, H.: Toxicological and ecotoxicological potencies of biofuels used for the transport sector -a literature review. *Energy Environ. Sci.*, 2012, **5**, 7381–7392 DOI: [10.1039/c2ee03033k](https://doi.org/10.1039/c2ee03033k)
- [35] Pedersen, F.; Petersen, G.I.: Variability of species sensitivity to complex mixtures. *Water Sci. Technol.*, 1996, **33**(6), 109–119 DOI: [10.1016/0273-1223\(96\)00318-6](https://doi.org/10.1016/0273-1223(96)00318-6)
- [36] Pintar, A.; Besson, M.; Gallezot, P.; Gibert, J.; Martin, D.: Toxicity to *Daphnia magna* and *Vibrio fischeri* of Kraft bleach plant effluents treated by catalytic wet-air oxidation. *Water Res.*, 2004, **38**(2), 289–300 DOI: [10.1016/j.watres.2003.09.027](https://doi.org/10.1016/j.watres.2003.09.027)
- [37] Czech, B.; Joško, I.; Oleszczuk, P.: Ecotoxicological evaluation of selected pharmaceuticals to *Vibrio fischeri* and *Daphnia magna* before and after photooxidation process. *Ecotoxicol. Environ. Safety*, 2014, **104**, 247–253 DOI: [10.1016/j.ecoenv.2014.03.024](https://doi.org/10.1016/j.ecoenv.2014.03.024)
- [38] Brack, W.; Aissa, S.A.; Backhaus, T.; Dulio, V.; Escher, B.I.; Faust, M.; Hilscherova, K.; Hollender, J.; Hollert, H.; Müller, C.; Munthe, J.; Posthuma, L.; Seiler, T.B.; Slobodnik, J.; Teodorovic, I.; Tindall, A.J.; de Aragão Umbuzeiro, G.; Zhang, X.; Altenburger, R.: Effect-based methods are key. The European Collaborative Project SOLUTIONS recommends integrating effect-based methods for diagnosis and monitoring of water quality. *Environ. Sci. Eur.*, 2019, **31**, 10 DOI: [10.1186/s12302-019-0192-2](https://doi.org/10.1186/s12302-019-0192-2)
- [39] Marzullo, R.C.M.; Matai, P.H.L.S.; Morita, D.M.: New method to calculate water ecotoxicity footprint

- of products: A contribution to the decision-making process toward sustainability. *J. Clean. Prod.*, 2018, **188**, 888–899 DOI: [10.1016/j.jclepro.2018.03.307](https://doi.org/10.1016/j.jclepro.2018.03.307)
- [40] Jos, A.; Repetto, G.; Rios, J.C.; Hazen, M.J.; Molero, M.L.; Peso, A.; Salguero, M.; Fernández-Freire, P.; Pérez-Martín, J.M.; Cameán, A.: Ecotoxicological evaluation of carbamazepine using six different model systems with eighteen endpoints. *Toxicol. In Vitro*, 2003, **17**, 525–532 DOI: [10.1016/S0887-2333\(03\)00119-X](https://doi.org/10.1016/S0887-2333(03)00119-X)
- [41] Manusadžianas, L.; Sadauskas, K.; Vitkus, R.: Comparative study of indices used in toxicity evaluation of effluents. *Desalination*, 2010, **250**, 383–389 DOI: [10.1016/J.DESAL.2009.09.061](https://doi.org/10.1016/J.DESAL.2009.09.061)

INFLUENCE OF MINERAL COMPOSITION IN NATURAL GRANITE ROCKS ON MICROHARDNESS

ESZTER KELEMEN-CSERTA*¹ AND ISTVÁN GÁBOR GYURIKA¹

¹Research Centre for Engineering Sciences, University of Pannonia, Egyetem u. 10, 8200 Veszprém, HUNGARY

Granites are becoming increasingly popular and, as a result, their areas of use are expanding. In addition to their colour and particle size, the surface roughness of the machined material is becoming an important aspect of their application. In order to create a suitable surface roughness, the type of rocks located on the surface, elemental composition and microhardness of the minerals are important, because knowledge of these characteristics can be used to determine the machining parameters. Microhardness is affected by the atomic percentage values of Si, Al and Na. In addition, for some minerals, a correlation can also be established between the Si, Al and Na components.

Keywords: *natural rocks, granite, microhardness, surface roughness*

1. Introduction

Granites are one of the most commonly used natural rocks due to their beautiful appearance and the fact that many variations in their colour can be found. Their appearance is special since the grains of the constituent minerals found in granite are nicely outlined and clearly visible with the naked eye, therefore, are also preferred architecturally. Zhao et al. [1] studied the effect of weathering on samples of granite. For this purpose, the samples were soaked in different concentrations of Na₂SO₄ and MgSO₄ before the wetting–drying cycles. It was found that the increase in wetting–drying cycles greatly influences the physical parameters, namely weight, colour, surface roughness and hardness. In addition, the effect of Na₂SO₄ on the specimens was greater than that of MgSO₄ and the higher salt concentration accelerated weathering of the rock.

Although the spectacular grain structure of granite is advantageous in terms of appearance, it is disadvantageous in terms of machinability. The particles are composed of different minerals that result in a heterogeneous structure. This heterogeneous property makes machining difficult.

Ramnath et al. [2] have developed epoxy granite composites (EGCs) as a novel alternative material, which exhibit several positive properties, e.g., are stable and lighter, but due to their heterogeneous structure, machining was critical. According to experiments, it was shown that 600 rpm is the optimal spindle speed and 0.09 m/min is the optimal feed rate for machining this material. This

value can even be used for natural granite rocks.

In collaboration with us, many researchers have studied the formation, change and effect of surface roughness. Sanmartín et al. [3] studied the effect of surface treatment on roughness, surface gloss and colour. It was found that the colour of granite affects the gloss of the surface differently for smooth and rough surfaces. The change in luminosity also depends on the mineral composition of the rock.

Shen et al. [4] studied concrete and granite by investigating the relationship between surface roughness and hydrophilicity. In their experiments, it was observed that the bonding strength always increases with the joint roughness coefficient (JRC). Furthermore, the relationship between surface roughness and hydrophilicity was determined as well as the importance of knowing the effect of surface adhesion and surface characteristics evaluated.

Aydin et al. [5] machined the surface of granite rocks with diamond saw blades and examined their surface roughness. They concluded that instead of mechanical properties, mineral properties affect surface roughness. Among the mineralogical properties, the particle size was chosen as the primary aspect of surface roughness.

Others have studied the hardness of granite from different perspectives. Prikryl [6] cut thin sections of the rock samples in which the size, distribution, shape, orientation and mineral composition of the grains were analysed. It was found that as the particle size of minerals decreases, their strength increases.

Rajpurohit et al. [7] investigated a statistical relationship between the Cerchar Hardness Index and this dia-

*Correspondence: kelemen.cserta.eszter@mk.uni-pannon.hu

mond tool. It was concluded that the hardness of the rock greatly influences the wear of the tool. A similar result was obtained by Delgado et al. [8] who studied the sawability of granite as well as determined that its hardness strongly influences the sawability and wear of diamond tools. The Vickers hardness of minerals was measured experimentally and it was determined that a small increase in hardness leads to a large decrease in the sawing speed. A similar result was obtained by Dong et al. [9] who developed an innovative method for sawing hard rocks and demonstrated that the sawing force correlates with the properties of the rock.

A similar experiment was performed by Yilmaz [10], who examined the wear of diamond tools as a function of the hardness of the minerals that granite is composed of. The rock hardness index of the specimens was used to determine the hardness according to the percentage occurrence of the constituent minerals. The results showed that the rock hardness index correlated with the sawblade wear rate (SWR) of the tool. Even though previous studies have attributed the percentage occurrence of quartz to the main reason for sawblade wear, Yilmaz's results showed that other minerals also influence tool wear. In another study, where Yilmaz et al. [11] conducted experiments on natural granite, they found that the maximum particle size of quartz, orthoclase and microcline had the greatest effect on SWR.

Li et al. [12] studied how the mineral content of rock affects its properties. For this purpose, the mineral content, particle size, abrasion resistance and hardness of 96 samples from 10 provinces in China were measured. The test results showed that the wear and hardness of the rock can be accurately determined based on the type of rock, mineral content and particle size.

Diamond is extremely hard, tough and thermally conductive, making it an excellent material for the purpose of cutting rocks. The abrasion resistance of rocks varies, so it is important to provide the right metal matrix in which the diamond grains can be placed. During the experiment, 2 materials were investigated, that is, the Co- and Fe-based metal matrices. The results showed that the Co-based metal matrix is suitable for cutting granites, while the Fe-based one is suitable for cutting marbles [13]. This theory is also supported according to a study by Gupta and Pratap [14]. They also studied the metal matrix of the tool and found that the metal matrix composite (MMC) influences the efficiency and service life of the tool.

Yan et al. [15] also searched for a way of modifying the machining tool to ensure granite surfaces are properly machined. An ultrahard polycrystalline diamond (UHPCD) tool was compared to a polycrystalline diamond (PCD) one. The hardness of UHPCD was 105-115 GPa, while that of PCD was 53-57 GPa. The results showed that the lifetime of UHPCD bits was 132.33 m and that of PCD ones was 83.76 m.

Using a hammer, Adebayo and Okewale [16] determined the rebound values of the specimens as a function of hardness as well as the mineral compositions of the

samples. It was concluded that the sample with the highest quartz content resulted in the highest Vickers hardness number.

A document published by the University of Kiel [17] contains a table presenting the Vickers hardness number of several materials, in which the Vickers hardness number of granite is $H_{V\text{granite}} = 850$ and that of quartz is $H_{V\text{quartz}} = 1200$.

Yusupov and co-researchers [18] studied the hardness of minerals in terms of grindability. It was concluded that the presence of quartz increases the grinding time by 1.5-2 times. To optimize the process and reduce the amount of energy required, they proposed a method in which the minerals are machined separately.

Xie and Tamaki [19] investigated the effect of the micro-hardness distribution in granite on the efficiency of abrasive machining. In their research, it was determined that the efficiency of abrasive machining increases as the microhardness of granite decreases.

From the literature, it is also clear that researchers have considered the types of minerals when studying natural rocks. In contrast, in the present paper, the mineral constituents are examined to observe how these affect the hardness of specimens and thus their machinability.

Our goal is to draw up a prediction system based on complex analysis to facilitate the specification of the parameters required for surface machining. Alternatively, the parameters can be modified according to the types of minerals present on the surface or the quality of the surface to be created.

2. Materials and methods

The granites used in the experiments differ in terms of colour (pink, yellowish, orange, greyish, black and white), grain size (fine, medium and coarse) and composition. 4 of the 5 samples come from Brazil and 1 from the Hungarian mine in Süttő.

During the experiment, an experimental process was developed to investigate the composition, formation and hardness of the rock. It was determined that although all granite samples contained the minerals quartz, feldspar and biotite, the difference was in the type of feldspar minerals.

2.1 Rock working

The surface of the slabs composed of natural rock was machined by a CNC machine manufactured in Italy (Fig. 1). The used equipment was an Italian Prussiani Golden Plus-type CNC machine with a maximum power consumption of 15 kW. The machining cutting depth was 1 mm, the cutting width was 40 mm and the feed speed was 0.1 mm/tooth. The cutting speed used during machining was 37.7 m/min. The machining tool in the CNC machine consisted of 22 segments and the face mill was 100 mm in diameter. Although the elemental composition of the face-mill matrix is not specified by the manufacturers,



Figure 1: The CNC equipment and various tools



Figure 2: One of the granite samples (orange)

scanning electron microscopy (SEM) of the tool showed that Co, Cu, Sn and Ag were also present.

2.2 Hardness measurements

Samples with approximate dimensions of 5 mm × 5 mm (Fig. 2) were cut from the machined rock slabs to ensure that they could be easily placed on the tables of various measuring devices.

The minerals were separated based on their appearance. Biotite, which could be identified by its characteristic dark/black colour, was the first to be examined, followed by feldspar and quartz. In the case of the latter two, even though it was more difficult to distinguish them from each other, in the following examination of mineral composition, it was possible to make an accurate distinction between them.

The hardness of minerals is usually given according to the Mohs scale. This does not provide an exact value, rather only reflects the relative hardness of the different minerals.

Secondly, it is worth mentioning the methods used to measure the hardness of metals, which despite yielding accurate values, are greatly influenced by different compositions of minerals.

Table 1: Parameters of the Wolpert Group hardness tester

Eyepiece magnification	10×
Resolution	0.1 μm
Objective magnification factor	10×, 20×, 40×, 50×, 60×
Total magnification	400× (for measurements) 100× (for observations)
Measuring range	200 μm
Hardness value	5-digit
Maximum specimen height	85 mm
XY stage dimensions	100 × 100 mm
Operating temperature	Range: 10 to 38 °C (50 to 100 °F)

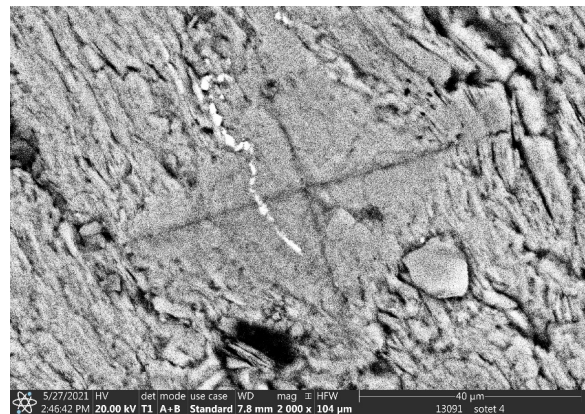


Figure 3: Imprint of the 136° square-based diamond pyramid

Measurements were performed on a WOLPERT W Group Micro Vickers digital auto turret 402MVD-type hardness tester, the parameters of which are shown in Table 1.

When measurements were taken, a specimen was placed on the measuring table and then the 136° square-based diamond pyramid for measuring the Vickers hardness was placed over the relevant mineral. After starting to take the measurements, the pyramid was pressed into the surface of the mineral where it left an imprint (Fig. 3). The peaks of the imprint were marked using a microscope, before the machine evaluated the results.

2.3 SEM

The chemical composition can be determined by scanning electron microscopy (SEM). A Thermo Fischer Scientific Aprea SEM, FEI/Philips XL-30 ESEM were used to examine the elemental composition of the sample's surface in a low vacuum at a resolution of 20 Å. During the evaluation, the equipment took a photo of the surface before evaluating the compositions of the selected areas. Given that the results were given in percentage composition, the types of constituent minerals present could be deduced (Fig. 4).

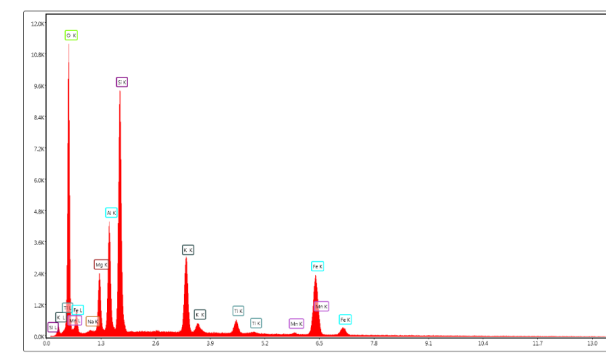


Figure 4: Elemental composition of biotite

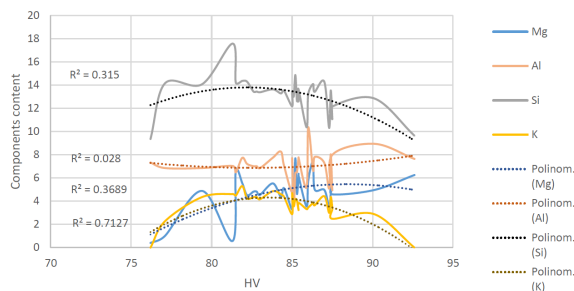


Figure 5: Effect of Mg, Al, Si and K constituents on Vickers hardness

3. Results

During this study, the minerals biotite, feldspar and quartz were examined on the surfaces of 5 different specimens.

Firstly, biotite was placed under the diamond pyramid of the hardness tester. It is known that the content of SiO_2 and grain size greatly influence the hardness as well as machinability of the specimens. However, it has not yet been studied whether and how the atomic percentage composition of the particles affects the hardness. Given that the hardness of granites is related to their quartz content, it was examined whether the hardness varies as a function of the Si content. Our measurements showed no correlation between the values. For biotite, no correlation was found between Si content and Vickers hardness.

Additional measurements also showed that the atomic percentage composition of biotite did not correlate with the Vickers hardness (HV). During the evaluation, the constituent elements (Mg, Al, K) were examined separately, but no correlation ($R_{\text{Mg}}^2 = 0.315$, $R_{\text{Al}}^2 = 0.028$, $R_{\text{Si}}^2 = 0.3689$, $R_{\text{K}}^2 = 0.6127$ where R^2 denotes the coefficient of determination) was found between changes in any of these constituents and hardness. It is also clear from the diagram (Fig. 5) that the individual constituents do not affect the Vickers hardness.

The next group of minerals studied were feldspars. After evaluating the measurements, several correlations were observed. Given that as the Si content increases, the total content of Na and Al decreases (Fig. 6), it can be stated that a decrease in the Si content leads to an increase

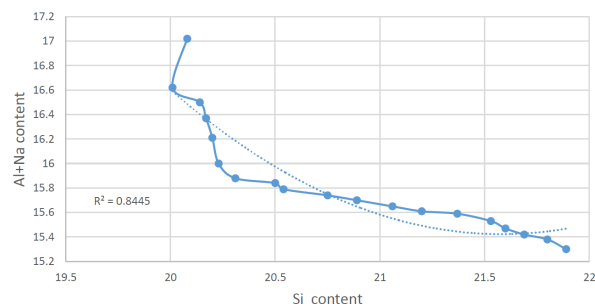


Figure 6: The correlation between Na+Al and Si contents

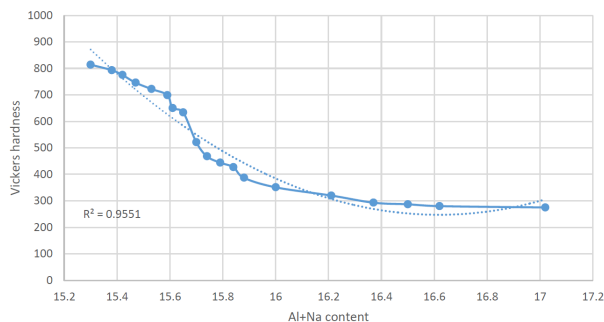


Figure 7: The correlation between HV and Na+Al content

in the Na+Al content in the case of feldspars ($R_{\text{Al+Na}}^2 = 0.8445$).

It also greatly affects the Vickers hardness. The change in Vickers hardness is inversely proportional to an increase in Na+Al content (Fig. 7). As the Na+Al content in the mineral increases, the Vickers hardness decreases ($R_{\text{HV}}^2 = 0.9551$).

The results of our measurements are illustrated in the diagram Fig. 7.

In the case of the mineral quartz, the results do not exhibit such a correlation ($R_{\text{HV}}^2 = 0.2646$). In uncontaminated quartz, where no impurities (C, K, Ca, Fe) were detected, large variations in hardness were observed (Fig. 8), presumably due to the crystallization of quartz.

For minerals where other constituents are present in addition to quartz, neither were clear correlations between the changes in Vickers hardness and elemental composition observed. Given the results, changes in the constituents of quartz do not affect the Vickers hardness.

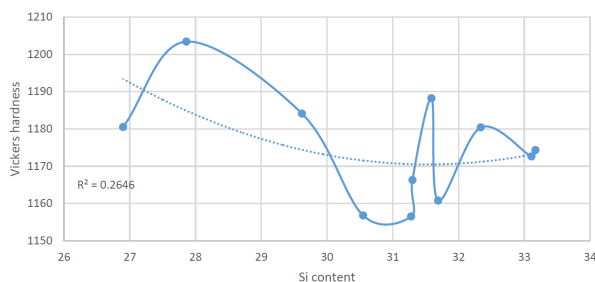


Figure 8: The correlation between HV and Si content

4. Conclusions

An important aspect when machining natural rocks is the hardness of the minerals they are composed of, because the hardness of the rock surface greatly influences machinability. Based on preliminary measurements, the surface composition of feldspars was examined in order to predict their hardness.

With the knowledge obtained during the present study, the parameters of the processing equipment can be adjusted according to the mineral composition on the given surface.

In the case of the minerals biotite and quartz, clear values for machining could not be provided, since increasing the Si content of either mineral has no effect on the Vickers hardness.

Our results suggest that Na+Al constituents do not affect either the change in hardness or the Si content.

In the case of feldspars, on the other hand, it was observed that both the hardness and Si content are inversely proportional to the Na+Al content. As granites constitute several types of feldspars, these research results are a major step forward in the development of a forecasting system.

Acknowledgements

The authors are deeply indebted to their supervisor Dr. Margit Eniszné Bódogh (PhD; University of Pannonia), Ferencné Bakos (laboratory technician, University of Pannonia) and Miklós Jakab (PhD student, University of Pannonia) for their help in the measurement and evaluation processes applied in the scope of the present study.

REFERENCES

- [1] Zhao, F.; Sun, Q.; Zhang, W.: Combined effects of salts and wetting–drying cycles on granite weathering, *Bull. Eng. Geol. Environ.*, 2020, **79**(7) 3707–3720 DOI: [10.1007/s10064-020-01773-3](https://doi.org/10.1007/s10064-020-01773-3)
- [2] Arun Ramnath, R.; Thyla, P. R.; Harishsharan, A. K. R.: Machining parameter selection in milling epoxy granite composites based on AHP, *Mater. Today Proc.*, 2021, **42**(2), 319–324 DOI: [10.1016/j.matpr.2020.09.340](https://doi.org/10.1016/j.matpr.2020.09.340)
- [3] Sanmartín, P.; Silva, B.; Prieto, B.: Effect of surface finish on roughness, color, and gloss of ornamental granites, *J. Mater. Civ. Eng.*, 2011, **23**(8), 1239–1248 DOI: [10.1061/\(ASCE\)MT.1943-5533.0000285](https://doi.org/10.1061/(ASCE)MT.1943-5533.0000285)
- [4] Shen, Y.; Wang, Y.; Yang, Y.; Sun, Q.; Luo, T.; Zhang, H.: Influence of surface roughness and hydrophilicity on bonding strength of concrete-rock interface, *Constr. Build. Mater.*, 2019, **213**, 156–166 DOI: [10.1016/j.conbuildmat.2019.04.078](https://doi.org/10.1016/j.conbuildmat.2019.04.078)
- [5] Aydin, G.; Karakurt, I.; Aydiner, K.: Investigation of the surface roughness of rocks sawn by diamond sawblades, *Int. J. Rock Mech. Min. Sci.*, 2013, **61**, 171–182 DOI: [10.1016/j.ijrmms.2013.03.002](https://doi.org/10.1016/j.ijrmms.2013.03.002)
- [6] Prikryl, R.: Some microstructural aspects of strength variation in rocks, *Int. J. Rock Mech. Min. Sci.*, 2001, **38**(5), 671–682 DOI: [10.1016/S1365-1609\(01\)00031-4](https://doi.org/10.1016/S1365-1609(01)00031-4)
- [7] Rajpurohit, S. S.; Sinha, R. K.; Sen, P.: Influence of Cerchar hardness index of hard rock granite on wear of diamond tools, *Mater. Today Proc.*, 2020, **33**, 5471–5475 DOI: [10.1016/j.matpr.2020.03.273](https://doi.org/10.1016/j.matpr.2020.03.273)
- [8] Delgado, N. S.; Rodriguez-Rey, A.; del Ríó, L. M. S.; Sarriá, I. D.; Calleja, L.; de Argandoña, V. G. R.: The influence of rock microhardness on the sawability of Pink Porrino granite (Spain), *Int. J. Rock Mech. Min. Sci.*, 2005, **42**(1), 161–166 DOI: [10.1016/j.ijrmms.2004.08.010](https://doi.org/10.1016/j.ijrmms.2004.08.010)
- [9] Dong, P.; Zhang, J.; Ouyang, C., Sun, D.; Wu, J.: Investigation on sawing performance of diamond frame saw based on reciprocating swing in processing hard stone, *J. Mater. Process. Technol.*, 2021, **295**, 117171 DOI: [10.1016/j.jmatprotec.2021.117171](https://doi.org/10.1016/j.jmatprotec.2021.117171)
- [10] Yılmaz, N. G.: Abrasivity assessment of granitic building stones in relation to diamond tool wear rate using mineralogy-based rock hardness indexes, *Rock Mech. Rock Eng.*, 2011, **44**(6), 725–733 DOI: [10.1007/s00603-011-0166-1](https://doi.org/10.1007/s00603-011-0166-1)
- [11] Yılmaz, N. G.; Goktan, R. M.; Kibici, Y.: An investigation of the petrographic and physico-mechanical properties of true granites influencing diamond tool wear performance, and development of a new wear index, *Wear*, 2011, **271**(5-6), 960–969 DOI: [10.1016/j.wear.2011.04.007](https://doi.org/10.1016/j.wear.2011.04.007)
- [12] Li, Q.; Li, J.; Duan, L.; Tan, S.: Prediction of rock abrasivity and hardness from mineral composition, *Int. J. Rock Mech. Min. Sci.*, 2021, **140**, 104658 DOI: [10.1016/j.ijrmms.2021.104658](https://doi.org/10.1016/j.ijrmms.2021.104658)
- [13] Bulut, B.; Gunduz, O.; Baydogan, M.; Kayali, E. S.: Determination of matrix composition for diamond cutting tools according to the hardness and abrasivity properties of rocks to be cut, *Int. J. Refract. Met. Hard Mater.*, 2021, **95**, 105466 DOI: [10.1016/j.ijrmhm.2020.105466](https://doi.org/10.1016/j.ijrmhm.2020.105466)
- [14] Gupta, R. K.; Pratap, B.: Diamond tools processing for marble and granite: Cutting & wear, *Mater. Today Proc.*, 2021, **46**(6), 2135-2140 DOI: [10.1016/j.matpr.2021.02.346](https://doi.org/10.1016/j.matpr.2021.02.346)
- [15] Yan, G.; Yue, W.; Meng, D.; Lin, F.; Wu, Z.; Wang, C.: Wear performances and mechanisms of ultrahard polycrystalline diamond composite material grinded against granite, *Int. J. Refract. Met. Hard Mater.*, 2016, **54**, 46–53 DOI: [10.1016/j.ijrmhm.2015.07.014](https://doi.org/10.1016/j.ijrmhm.2015.07.014)
- [16] Adebayo, B.; Okewale, I. A.: Analysis of the potential of some Nigerian rocks to wear drill bit, *AU J. Technol.*, 2007, **11**(2) <https://www.thaiscience.info/journals/Article/AUJT/10290645.pdf>
- [17] Hardness, [Online]. Available: https://www.tf.uni-kiel.de/matwis/amat/mw1_ge/kap_8/advanced/t8_4_2.html
- [18] Yusupov, T. S.; Kirillova, E. A.; Shumskaya, L. G.: Mineral hardness effect on the combined mineral

- grinding. *J. Min. Sci.*, 2007, **43**(4), 450–454 DOI: [10.1007/s10913-007-0046-y](https://doi.org/10.1007/s10913-007-0046-y)
- [19] Xie, J.; Tamaki, J.: Parameterization of micro-hardness distribution in granite related to abrasive machining performance, *J. Mater. Process. Tech.*, 2007, **186**(1-3), 253–258 DOI: [10.1016/j.jmatprotec.2006.12.041](https://doi.org/10.1016/j.jmatprotec.2006.12.041)